

AD-A143 507

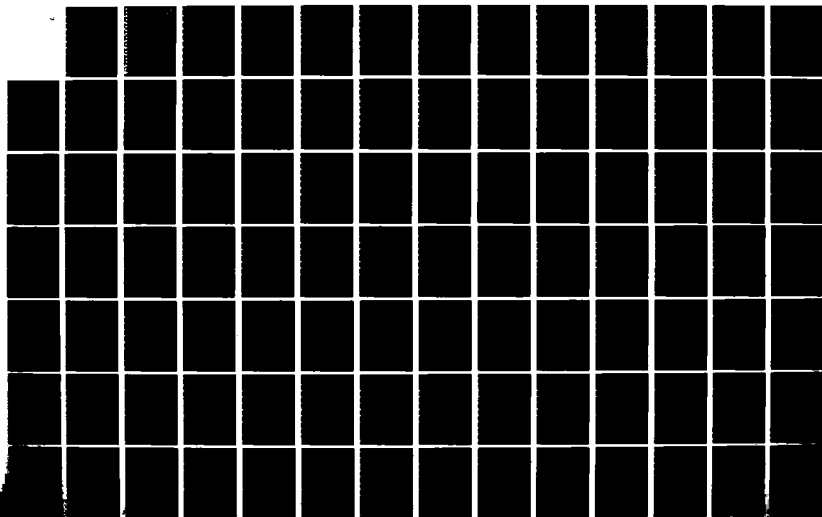
STUDIES OF THE ELECTRIC FIELD DISTRIBUTION IN BIOLOGICAL  
BODIES - EXPERIMENTAL (U) OTTAWA UNIV (ONTARIO) DEPT OF  
ELECTRICAL ENGINEERING S S STUCHLY ET AL. MAY 84  
N00044-82-G-0011

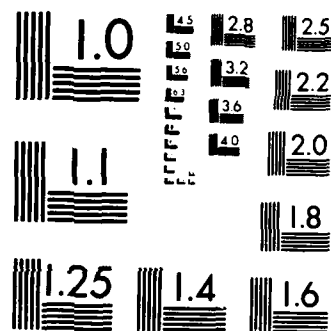
1/2

UNCLASSIFIED

F/G 6/18

NL





MICROCOPY RESOLUTION TEST CHART  
NATIONAL BUREAU OF STANDARDS-1963-A

AD-A143 507

ANNUAL SCIENTIFIC REPORT

2

Studies of the Electric Field Distribution in  
Biological Bodies - Experimental Dosimetry at  
Radio Frequencies

Research Grant No. N00014-82-G-0011

Submitted to

Office of Naval Research  
Division of Biological Sciences  
Department of the Navy  
Arlington, VA 22217

by

Dr. Stanislaw S. Stuchly  
and  
Dr. Maria A. Stuchly

Department of Electrical Engineering  
University of Ottawa  
Ottawa, Ontario  
Canada K1N 6N5

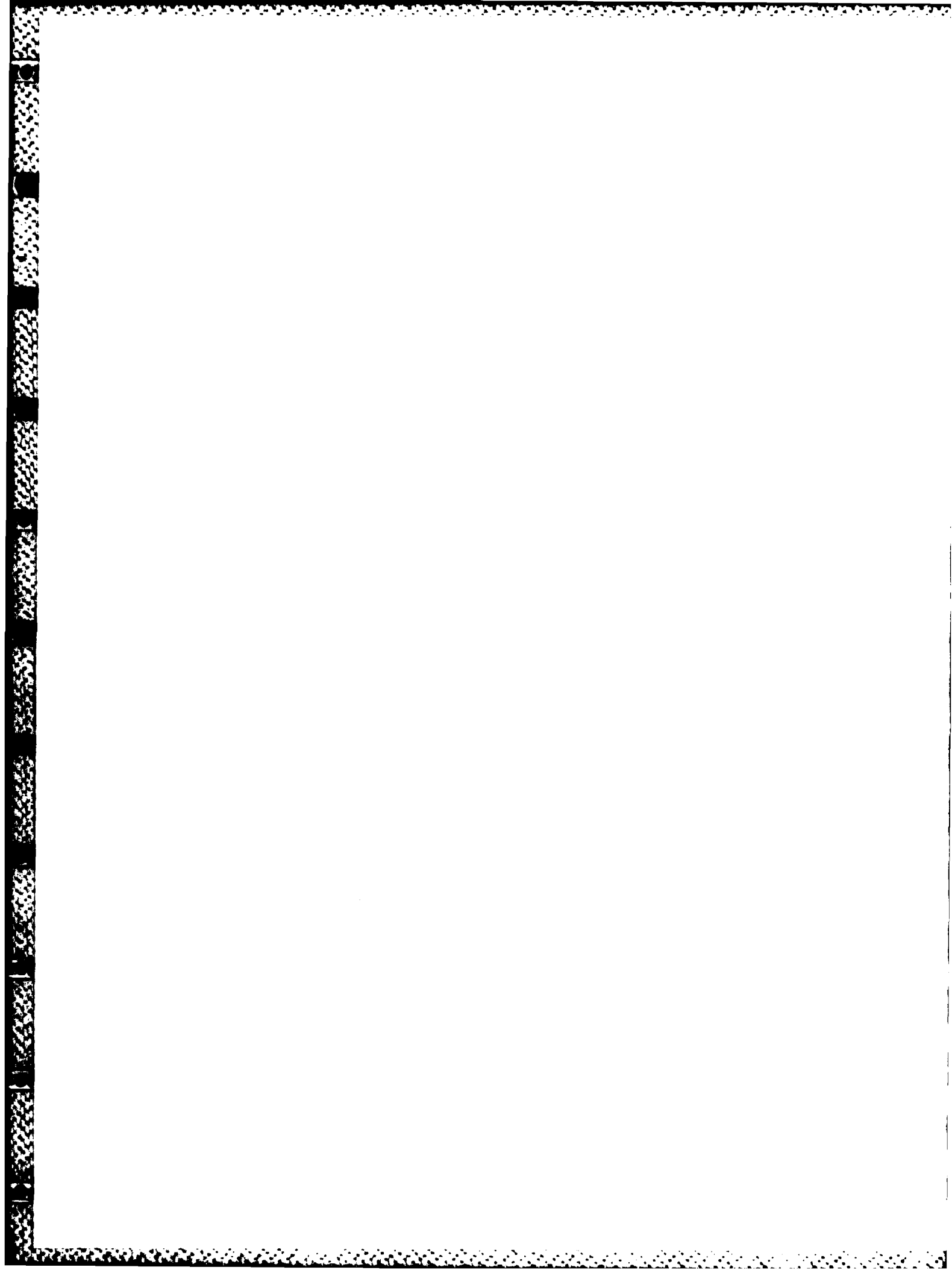
Reported period  
June 1, 1983 - May 31, 1984

FILE COPY

DTIC  
ELECTE  
JUL 27 1984  
S D

DISTRIBUTION STATEMENT  
Approved for public  
Distribution Unlimited

- 84 07 25 0511



UNCLASSIFIED

SECURITY CLASSIFICATION OF THIS PAGE (When Data Entered)

REPORT DOCUMENTATION PAGE		READ INSTRUCTIONS BEFORE COMPLETING FORM
1. REPORT NUMBER	2. GOVT ACCESSION NO.	3. RECIPIENT'S CATALOG NUMBER
4. TITLE (and Subtitle) Studies of the Electric Field Distribution in Biological Bodies - Experimental Dosimetry at Radio Frequencies		5. TYPE OF REPORT & PERIOD COVERED Annual Scientific 1983-1984
7. AUTHOR(s) Dr. S. S. Stuchly & Dr. M. A. Stuchly		6. PERFORMING ORG. REPORT NUMBER
9. PERFORMING ORGANIZATION NAME AND ADDRESS Dept. of Electrical Engineering, Univ. of Ottawa Ottawa, Ontario Canada, K1N 6N5		8. CONTRACT OR GRANT NUMBER(s) N00014-82-G-0011
11. CONTROLLING OFFICE NAME AND ADDRESS Office of Naval Research, 800 North Quincy St., Arlington, VA 22217		10. PROGRAM ELEMENT, PROJECT, TASK AREA & WORK UNIT NUMBERS 665-003
14. MONITORING AGENCY NAME & ADDRESS (if different from Controlling Office)		12. REPORT DATE May 84
		13. NUMBER OF PAGES
		15. SECURITY CLASS. (of this report) Unclassified
		15a. DECLASSIFICATION/DOWNGRADING SCHEDULE
16. DISTRIBUTION STATEMENT (of this Report) Unlimited		
<div style="border: 1px solid black; padding: 5px; display: inline-block;"> DISTRIBUTION STATEMENT Approved for public release; Distribution Unlimited </div>		
17. DISTRIBUTION STATEMENT (of the abstract entered in Block 20, if different from Report)		
18. SUPPLEMENTARY NOTES		
19. KEY WORDS (Continue on reverse side if necessary and identify by block number) 1. Radiofrequency Radiation; 2. Absorption; 3. Dosimetry; 4. Computer Control; 5. Spatial Distribution; 6. Human Model		
20. ABSTRACT (Continue on reverse side if necessary and identify by block number) This report summarizes research progress in the period from June 1, 1983 to May 31, 1984 in studies of the specific absorption rate (SAR) in a model of the human body exposed to radiofrequency radiation in the far and near field of antennas. The objective of the project was to develop and evaluate a computer-controlled system for measurements of the spatial distribution of the SAR in simulated and real biological bodies and to perform measurements on a model of the human body in the near field of typical antennas. ---CONT.		

DD FORM 1 JAN 73 1473

EDITION OF 1 NOV 65 IS OBSOLETE  
S/N 0102-LF-014-6601

UNCLASSIFIED

SECURITY CLASSIFICATION OF THIS PAGE (When Data Entered)

UNCLASSIFIED

SECURITY CLASSIFICATION OF THIS PAGE (When Data Entered)

Block 20. CONT.

In summary, our investigations of the SAR distribution in a full-scale mode of man showed that relevant dosimetric data in the far and the near field can be conveniently and accurately obtained by the measurements using implantable electric field probes and computer-controlled data acquisition system. Such information cannot be reliably obtained using presently available numerical methods.

Large gradients and non-uniformities in the SAR distribution exist for exposures in the far- and the near-field of antennas. Typically, the spatial peak SAR is over 100 times greater than the whole-body average SAR. It is well justified to assume that biological responses to exposure to RF fields are dependent on the SAR gradients and the locations of the extrema of the SAR, not only on the whole-body average. Therefore, information on the spatial distribution of the SAR is essential in developing rational exposure standards, particularly for exposures in the near-field.

Accession For	
NTIS GRA&I	<input checked="checked" type="checkbox"/>
DTIC TAB	<input type="checkbox"/>
Unannounced	<input type="checkbox"/>
Justification	
By	
Distribution/	
Availability Codes	
Dist	Avail and/or Special
A/1	



S/N 0102- LF-014-6601

SECURITY CLASSIFICATION OF THIS PAGE(When Data Entered)

TABLE OF CONTENTS

- (i) Executive Summary
- (ii) List of publications and presentations
- (iii) List of figures
- (iv) List of Tables
  
- 1. INTRODUCTION
  
- 2. EXPERIMENTAL SYSTEM
  
- 3. EXPERIMENTS IN THE FAR-FIELD
  - 3.1 Rationale
  - 3.2 Experimental results
  - 3.3 Comparison with theory
  - 3.4 Discussion and main findings
  - 3.5 Conclusions and future research plans
  
- 4. EXPERIMENTS IN THE NEAR-FIELD
  - 4.1 Experimental results
  - 4.2 Comparison with theory
  - 4.3 Discussion and main findings
  - 4.4 Conclusions and future research needs

### EXECUTIVE SUMMARY

This report summarizes research progress in the period from June 1, 1983 to May 31, 1984 in studies of the specific absorption rate (SAR) in a model of the human body exposed to radiofrequency radiation in the far and near field of antennas. The objective of the project was to develop and evaluate a computer-controlled system for measurements of the spatial distribution of the SAR in simulated and real biological bodies and to perform measurements on a model of the human body in the near field of typical antennas.

#### Experimental System

A computer-controlled scanning system is capable of positioning electric field probes within a volume of  $2 \times 0.5 \times 0.5$  m with an uncertainty of 0.05 mm. The system also provides for data acquisition, processing, display and recording. The specific absorption rate is calculated from the measured electric field intensity. The electric field intensity is measured with implantable triaxial electric-field probes. The probes have been fully characterized and calibrated at various frequencies. Their calibration accuracy is  $\pm 1$  dB, while the repeatability in the SAR measurements is better than  $\pm 0.5$  dB. The system can acquire, and record the data on the SAR in over 650 locations within a model of the human body in approx. 1.5 h.



To simulate the electrical properties of tissues new phantom materials have been developed. They are characterized by a long life time of over one year, in contrast to the previously developed materials which cannot be stored for longer than one month as their electrical and mechanical properties deteriorate rapidly.

### Energy Absorption in a Model of Man

#### \*Far-field Investigations

Investigations in the far field were performed to assess how reliable are numerical calculations using the block model of man. The measurements were done at 350 MHz because of previously reported resonance of the head, and nonuniform SAR distribution in the head. Maps of the SAR distribution were obtained for all three polarizations.

The spatial distribution of the SAR is highly non-uniform, with the SAR typically varying at least three orders of magnitude. Very large gradients of the SAR occur along the direction of wave propagation. At a frequency of 350 MHz, and anticipated at higher frequencies the SAR decreases exponentially in the body parts whose dimensions are comparable or greater than the wavelength in free space. The neck-head region constitutes a rather complex geometry and the resulting SAR is highly non-uniform and frequency dependent.

\*Far-field Comparison with Theory

A comparison of the SAR measured with the calculated data using the block model of man consisting of 340 cells showed a good agreement for the whole-body and the head average SARs but differences of up to two orders of magnitude (a factor of 100) in the spatial distribution of the SAR and the SARs averaged over small volumes. This finding underscores the importance of experimental methods in finding the SAR distributions, as well as the need for verification of theoretical predictions. Verification of some of the calculated results (e.g. whole-body or body-part average SARs) is not sufficient to prove the calculations correct for other data.

\*Near-field Investigations

Near-field investigations were performed at a frequency of 350 MHz for three antennas, a resonant dipole, a resonant dipole over the ground plane and a resonant slot. These antennas were selected to represent important exposure situations, namely portable transmitters and leakage fields.

For all configurations investigated (9), the spatial distribution of the SAR is highly nonuniform with the maximum to the whole body SAR ratio of about 170. The highest SARs at 350 MHz are at the antenna axis, except for antennas in the E polarization located close to the neck-head region. In the latter case the maximum SAR is in the neck. Larger SAR gradients exist for the E polarization than for the other two polarizations.

Analogously to exposure in the far-field, at 350 MHz and higher frequencies the SAR decreases exponentially in the direction of the wave propagation within approx. 10-12 cm, where its magnitude is about one hundred times below the SAR value at the surface, and about five times below the whole-body average. Therefore, the maximum SAR in the near field is always on the body surface, the increase in the center of the neck is small contrary to the situation in the far-field.

The relative spatial distribution of the SAR depends mainly on the antenna type, position and polarization. The whole-body average SAR is basically determined by the antenna gain and the distance from the body.

For antennas placed 8 cm from the body at 350 MHz, an input power to the antenna of 25 W is required to exceed the ANSI-1982 limit of 0.4 W/kg for the whole-body average SAR, but only 4 W is sufficient to exceed the spatial peak SAR of 8 W/kg (averaged over 1 g of tissue).

#### \*Near-field Comparison with Theory

A comparison with the theoretical predictions for the block model of man consisting of 90 cells was made for a dipole in the E polarization at 350 MHz. The average whole-body SARs were found within less than 2%. Large differences were found in the SAR distribution, similarly as in the far-field, the exponential decay of the SAR was not predicted by the theory. Relatively large differences, of an order of 5 to 10, were found between the

SAR averaged over various body volumes. This comparison again underscored the inherent limitations of the theoretical analysis.

In summary, our investigations of the SAR distribution in a full-scale mode of man showed that relevant dosimetric data in the far and the near field can be conveniently and accurately obtained by the measurements using implantable electric field probes and computer-controlled data acquisition system. Such information cannot be reliably obtained using presently available numerical methods.

Large gradients and non-uniformities in the SAR distribution exist for exposures in the far- and the near-field of antennas. Typically, the spatial peak SAR is over 100 times greater than the whole-body average SAR. It is well justified to assume that biological responses to exposure to RF fields are dependent on the SAR gradients and the locations of the extrema of the SAR, not only on the whole-body average. Therefore, information on the spatial distribution of the SAR is essential in developing rational exposure standards, particularly for exposures in the near-field.

Publications, Thesis and Presentations

1. S.S. Stuchly, M. Barski, B. Tam, G. Hartsgrove and S. Symons, "Computer based scanning system for electromagnetic dosimetry", Rev. Sci. Instrum., 54(11), pp. 1547-1550, Nov. 1983.
2. M.A. Stuchly, A. Kraszewski and S.S. Stuchly, "Implantable electric-field probes - some performance characteristics", IEEE Trans. Biomed. Engn. vol. BME, accepted 1984.
3. G.H. Wong, S.S. Stuchly, A. Kraszewski and M.A. Stuchly, "Probing electromagnetic fields in lossy spheres and cylinders", IEEE Trans. Microwave Theory and Techn., vol. MTT, (special issue), accepted 1984.
4. A. Kraszewski, M.A. Stuchly, S.S. Stuchly, G. Hartsgrove and D. Adamski, "Specific absorption rate distribution in a full-scale model of man at 350 MHz", IEEE Trans. Microwave Theory and Techn., vol. MTT (special issue), accepted 1984.
5. A. Kraszewski, M.A. Stuchly, S.S. Stuchly and G. Hartsgrove, "Specific absorption rate distribution in a model of man at various polarizations", 1984 International Microwave Symposium Digest, San Francisco, May 30-June 1, 1984.
6. G.H. Wong, "Specific absorption rate distribution in simple geometrical bodies at radio frequencies", M.A.Sc. Thesis, University of Ottawa, 1983.
7. A. Kraszewski, M.A. Stuchly, S.S. Stuchly and G. Hartsgrove, "Specific absorption rate distribution in a model of man at 350 MHz", 1984 BEMS Meeting, Atlanta, GA, July 15-19, 1984, (abstract).
8. G.W. Hartsgrove and A. Kraszewski, "Improved tissue-equivalent materials for electromagnetic absorption studies", 1984 BEMS Meeting, Atlanta, GA, July 15-19, 1984, (abstract).
9. M.A. Stuchly, A. Kraszewski, S.S. Stuchly and G. Hartsgrove, "Distribution of radiofrequency energy in a model of man-experimental results", 1984 URSI/BEMS Symposium, Florence, Italy, August 26-29, 1984.
10. A. Kraszewski, S.S. Stuchly, M.A. Stuchly, G. Hartsgrove and D. Adamski, "Energy absorption in the near field-experimental results for a model of man", 1984 URSI/BEMS Symposium, Florence, Italy, August 26-29, 1984.
11. A. Kraszewski, S.S. Stuchly, M.A. Stuchly, G. Hartsgrove and D. Adamski, "Specific absorption rate distribution in a model of man exposed in the near field", 1984 BEMS Meeting, Atlanta, GA, July 15-19, 1984, (abstract).

12. S.S. Stuchly, A. Kraszewski, M.A. Stuchly, G. Hartsgrove and G.H. Wong, "System for measuring the distribution of the internal electric field in models of animals and humans", 1984 IEEE-EMC-S Symposium, Tokyo, Japan, October 16-18, 1984.
13. M.A. Stuchly, A. Kraszewski, S.S. Stuchly, G. Hartsgrove and D. Adamski, "Dosimetry in a full scale model of the human body", 1984 IEEE-EMC-S Symposium, Tokyo, Japan, October 16-18, 1984.

LIST OF TABLES

1. Average specific absorption rate in a model of man exposed to a plane-wave of  $1 \text{ mW/cm}^2$  at 350 MHz.
2. Average specific absorption rate for the whole body and the head. Comparison between theory & experiment.
3. Average specific absorption rate for the whole-body and the body parts for various antennas in the near-field.
4. Exposure conditions for the experiment and the parameters for the block calculations in the near-field.
5. Maximum and mean specific absorption rate SAR along the direction of propagation, SAR, and the attenuation coefficient for antennas in the near-field.

## List of Figures

- Figure 1 - Schematic diagram of the modified experimental system for the acquisition, display and recording of the SAR distributions in full-scale models of the human body.
- Figure 2 - Flow chart of the modified experimental system from Fig. 1.
- Figure 3 - Output power of the transmitter vs. the attenuator setting. The linearity of the transmitter was found to be  $0.052 \text{ dB} \pm 0.03 \text{ dB}$  (SD), with max. difference 0.12 dB.
- Figure 4 - The transfer characteristic of the modified experimental system. The linearity of the system was found to be  $\pm 0.32 \text{ dB}$ .
- Figure 5 - Far-field experiments. The specific absorption rate (SAR) (normalized to  $1 \text{ mW/cm}^2$ ) in the torso at three locations vs. position across the torso; frequency 350 MHz, polarization E  $\parallel$  L.
- Figure 6 - Far-field experiments. The specific absorption rate (SAR) (normalized to  $1 \text{ mW/cm}^2$ ) in the torso at three locations vs. position across the torso; frequency 350 MHz, polarization H  $\parallel$  L.
- Figure 7 - Far-field experiments. The distribution of the specific absorption rate (SAR) (normalized to  $1 \text{ mW/cm}^2$ ) along the main axis of the body; frequency 350 MHz, polarization k  $\parallel$  L.
- Figure 8 - Far-field experiments. The specific absorption rate (SAR) (normalized to  $1 \text{ mW/cm}^2$ ) in the torso vs. the distance from the body surface at which the wave is incident for three position:  $x = 96 \text{ cm}$ ,  $+ x = 117 \text{ cm}$  and  $* x = 137 \text{ cm}$  from the base (feet). Frequency 350 MHz, polarization E  $\parallel$  L.
- Figure 9 - Far-field experiments. The specific absorption rate (SAR) (normalized to  $1 \text{ mW/cm}^2$ ) in the torso vs. the distance from the body surface at which the wave is incident for three position:  $x = 96 \text{ cm}$ ,  $+ x = 117 \text{ cm}$  and  $* x = 137 \text{ cm}$  from the base (feet). Frequency 350 MHz, polarization H  $\parallel$  L.
- Figure 10 - Far-field experiments. The specific absorption rate (SAR) (normalized to  $1 \text{ mW/cm}^2$ ) in the torso vs. the distance across the torso at  $x = 137 \text{ cm}$  from the base (feet), frequency 350 MHz, polarization k  $\parallel$  L.
- Figure 11 - Far-field experiments. The specific absorption rate (SAR) (normalized to  $1 \text{ mW/cm}^2$  - logarithmic scale) in the torso vs. the distance from the body surface at which the wave is incident. Position  $x = 127 \text{ cm}$  from the base (feet), frequency 350 MHz, E  $\parallel$  L.



Figure 12 - Far-field experiments. The specific absorption rate (SAR) (normalized to  $1 \text{ mW/cm}^2$ ) in three body cross sections, frequency 350 MHz polarization H  $\parallel$  L, propagation back to front.

Figure 13 - Far-field experiments. The distribution of the specific absorption rate (SAR) (normalized to  $1 \text{ mW/cm}^2$ ) along the body axis, frequency 350 MHz,  
a) polarization E  $\parallel$  L  
b) polarization H  $\parallel$  L.

Figure 14 - Far-field experiments. The distribution of the specific absorption rate (SAR) (normalized to  $1 \text{ mW/cm}^2$ ) in the head-solid line with experimental points, frequency 350 MHz, polarization k  $\parallel$  L. Dashed line represents the SAR distribution in a 16-cm dia. lossy sphere calculated numerically and presented here for comparison.

Figure 15 - Far-field experiments. The distribution of the specific absorption rate (SAR) (normalized to  $1 \text{ mW/cm}^2$ ) in the neck - at  $x = 150 \text{ cm}$  from the base (feet), \* on the main axis, 5 cm of the main axis, frequency 350 MHz, polarization E  $\parallel$  L.

Figure 16 - Far-field experiments. The distribution of the specific absorption rate (SAR) (normalized to  $1 \text{ mW/cm}^2$ ) averaged over the body horizontal cross-sections (slices) for E  $\parallel$  L and H  $\parallel$  L, frequency 350 MHz.

Figure 17 - Far-field experiments. Comparison of the specific absorption rate (SAR) (normalized to  $1 \text{ mW/cm}^2$ ) distribution averaged over the body horizontal cross-sections (slices): the data calculated for the block model (solid line) and the experimental data (this work) (dashed line), frequency 350 MHz, polarization E  $\parallel$  L.

Figure 18 - Far-field experiments. Comparison of the specific absorption rate (SAR) (normalized to  $1 \text{ mW/cm}^2$ ) distribution in the head: the data calculated for the block model (number in blocks) and the experimental data (this work) (numbers in brackets), frequency 350 MHz,  
a) inner layer; polarization E  $\parallel$  L  
b) outer layer; polarization E  $\parallel$  L  
c) inner layer; polarization k  $\parallel$  L.

Figure 19 - Far field experiments. Comparison of the specific absorption rate (SAR) (normalized to  $1 \text{ mW/cm}^2$ ) distribution in the body: the data calculated for the block model (shaded bars) and the experimental data (this work) (dashed lines), frequency 350 MHz  
a) E  $\parallel$  L middle layer  
b) E  $\parallel$  L back layer  
c) E  $\parallel$  L front layer  
d) k  $\parallel$  L middle layer.

- Figure 20 - Far-field experiments. Comparison of the specific absorption rate (SAR) (normalized to  $1 \text{ mW/cm}^2$ ) distribution in the torso along the direction of propagation: the data calculated for the block model (dashed-line blocks) and the experimental data (this work) (stars), frequency 350 MHz, polarization E  $\parallel$  L,  
a) at  $x = 127 \text{ cm}$   
b) at  $x = 117 \text{ cm}$   
c) at  $x = 96 \text{ cm}$   
from the base level (feet).
- Figure 21 - Near-field experiments, resonant dipole. The distribution of the specific absorption rate (SAR) in three cross-sections of the body, frequency 350 MHz, polarization E  $\parallel$  L, power to the antenna 1W.  
a) dipole at  $x = 156.5 \text{ cm}$   
b) dipole at  $x = 137 \text{ cm}$   
c) dipole at  $x = 103 \text{ cm}$   
from the base (feet).
- Figure 22 - Near-field experiments, resonant dipole. The distribution of the specific absorption rate (SAR) in three cross-sections of the body, frequency 350 MHz, polarization H  $\parallel$  L, power to the antenna 1 W, dipole at  $x = 137 \text{ cm}$  from the base (feet).
- Figure 23 - Near-field experiments, resonant dipole. The distribution of the specific absorption rate (SAR) in three cross-sections of the body, frequency 350 MHz, polarization k  $\parallel$  L, dipole 14 cm above the head.
- Figure 24 - Near-field experiments, resonant dipole above the ground plane. The distribution of the specific absorption rate (SAR) in three cross-sections of the body, frequency 350 MHz, polarization E  $\parallel$  L, power to the antenna 1 W, dipole at  $x = 137 \text{ cm}$  from the base (feet).
- Figure 25 - Near-field experiments, resonant dipole above the ground plane. The distribution of the specific absorption rate (SAR) in three cross-sections of the body, frequency 350 MHz, polarization H  $\parallel$  L, power to the antenna 1 W, dipole at  $x = 137 \text{ cm}$  from the base (feet).
- Figure 26 - Near-field experiments, resonant dipole above the ground plane. The distribution of the specific absorption rate (SAR) in three cross-sections of the body, frequency 350 MHz, polarization k  $\parallel$  L, power to the antenna 1 W, dipole at  $x = 14 \text{ cm}$  above the head.
- Figure 27 - Near-field experiments, resonant slot. The distribution of the specific absorption rate (SAR) in three cross-sections of the body, frequency 350 MHz, polarization E  $\parallel$  L, power to the antenna 1 W, slot at  $x = 85 \text{ cm}$  from the base (feet).

- Figure 28 - Near-field experiments, resonant dipole. The mean values of the specific absorption rate (SAR) in a number of locations along the selected axis, frequency 350 MHz, polarization E  $\parallel$  L, power to the antenna 1 W,  
a) dipole at x = 156.5 cm  
b) dipole at x = 137 cm  
c) dipole at x = 103 cm  
from the base (feet).
- Figure 29 - Near-field experiments, resonant dipole. The mean values of the specific absorption rate (SAR) in a number of locations along the selected axis, frequency 350 MHz, polarization H  $\parallel$  L, power to the antenna 1 W, dipole at x = 137 cm from the base (feet).
- Figure 30 - Near-field experiments, resonant dipole. The mean values of the specific absorption rate (SAR) in a number of locations along the selected axis, frequency 350 MHz, polarization H  $\parallel$  L, power to the antenna 1 W, slot at x = 87 cm from the base (feet).
- Figure 31 - Near-field experiments, resonant dipole. The mean values of the specific absorption rate (SAR) for horizontal tissue layers along the vertical body axis, frequency 350 MHz, polarization E  $\parallel$  L, power to the antenna 1 W  
a) dipole at x = 156.5 cm  
b) dipole at x = 137 cm  
c) dipole at x = 103 cm  
from the base (feet).
- Figure 32 - Near-field experiments, resonant dipole. The mean values of the specific absorption rate (SAR) for horizontal tissue layers along the vertical body axis, frequency 350 MHz, polarization H  $\parallel$  L, power to the antenna 1 W, dipole at x = 137 cm from the base (feet).
- Figure 33 - Near-field experiments, resonant dipole above the ground plane. The mean values of the specific absorption rate (SAR) for horizontal tissue layers along the vertical body axis, frequency 350 MHz, polarization E  $\parallel$  L, power to the antenna 1 W, dipole at x = 137 cm from the base (feet).
- Figure 34 - Near-field experiments, resonant dipole above the ground plane. The mean values of the specific absorption rate (SAR) for horizontal tissue layers along the vertical body axis, frequency 350 MHz, polarization H  $\parallel$  L, power to the antenna 1 W, dipole at x = 137 cm from the base (feet).
- Figure 35 - Near-field experiments, resonant slot. The mean value of the specific absorption rate (SAR) for horizontal tissue layers along the vertical body axis, frequency 350 MHz, polarization E  $\parallel$  L, power to the antenna 1 W, slot at x = 85 cm from the base (feet).

- Figure 36 - Near-field experiment, resonant dipole. The specific absorption rate (SAR) in the torso at the dipole axis vs. distance from the body surface at which the wave is incident frequency 350 MHz, polarization E  $\parallel$  L, power to the antenna  
a) dipole at x = 103 cm  
b) dipole at x = 137 cm  
from the base (feet).
- Figure 37 - Near-field experiment, resonant dipole. The specific absorption rate (SAR) in the torso at the dipole axis vs. distance from the body surface at which the wave is incident, frequency 350 MHz, polarization H  $\parallel$  L, power to the antenna 1 W, dipole at x = 137 cm from the base (feet).
- Figure 38 - Near-field experiment, resonant dipole above the ground plane. The specific absorption rate (SAR) in the torso at the dipole axis vs. distance from the body surface at which the wave is incident, frequency 350 MHz, polarization E  $\parallel$  L, power to the antenna 1 W, dipole at x = 137 cm from the base (feet).
- Figure 39 - Near-field experiment, resonant dipole above the ground plane. The specific absorption rate (SAR) in the torso at the dipole axis vs. distance from the body surface at which the wave is incident, frequency 350 MHz, polarization H  $\parallel$  L, power to the antenna 1 W, dipole at x = 137 cm from the base (feet).
- Figure 40 - Near-field experiments, resonant dipole. The local values of the specific absorption rate (SAR) along the selected body axis, frequency 350 MHz, polarization k  $\parallel$  L, power to the antenna 1 W, the dipole 14 cm above the head.
- Figure 41 - Near-field experiments, resonant dipole above the ground plane. The local values of the specific absorption rate (SAR) along the selected body axis, frequency 350 MHz, polarization k  $\parallel$  L, power to the antenna 1 W, the dipole 14 cm above the head.
- Figure 42 - Near-field experiment. Comparison of the specific absorption rate (SAR) averaged over the body horizontal cross-sections: the experimental data vs. the data calculated for the block model, resonant dipole, frequency 350 MHz, polarization E  $\parallel$  L, power to the antenna 1 W, dipole at x = 137 cm from the base (feet).
- Figure 43 - Near-field experiment. Comparison of the specific absorption (SAR) averaged in the direction of the wave propagation for various positions along two vertical body axis. Experimental data (this work) vs. the data calculated for the block-model of man, frequency 350 MHz, polarization E  $\parallel$  L, power to the antenna 1 W, dipole at x = 137 cm from the base (feet).

Figure 44 - Near-field experiment. Comparison of the local specific absorption rate (SAR) along the direction of the wave propagation in the torso, experimental data (this work) (stars) and values calculated for the block model (blocks), frequency 350 MHz, polarization E  $\parallel$  L, power to the antenna 1 W.

## 1. INTRODUCTION

This report covers the second year of investigations of a two-year project. The objective of the project was to develop, design and evaluate a computer-controlled system for measurement of the distribution of the electric field or the specific absorption rate (SAR) in simulated and real biological bodies (models and animal cadavers) and to perform measurements on a model of the human body irradiated in the near field of typical radiofrequency and microwave antennas.

The general objective was achieved through the following developments and investigations:

- Design, development, fabrication and testing of a computer-controlled scanning system for positioning electric field probes, data acquisition, processing, display and recording.
- Design and assembly of a small anechoic chamber to house the radiofrequency parts of the experimental system.
- Design, fabrication and testing of auxiliary materials and circuits necessary for the experiment, i.e. molds of the full-size human body, tissue-equivalent materials, representative antennas, electronic circuitry with an optical-fiber link and a high-gain amplifier.

- Comprehensive evaluation and calibration of three types of implantable electric field probes.
- Evaluation of the whole system by investigation of the SAR distributions in lossy dielectric spheres and cylinders (the SAR in these objects were calculated analytically for the comparison).
- Investigations of the distribution of the specific absorption rate in a full-scale model of the human body exposed to a plane wave and comparison with theoretical calculations.
- Investigations of the specific absorption rate in a full scale model of the human body exposed in the near field of selected antennas.

The first annual scientific report described in detail the development of the scanning system, anechoic chamber, the auxiliary materials and circuits. While at the end of the first year of the project, the basic system was in place and operating, additional modifications were introduced during the second year to improve its performance. Only those modifications are outlined here, with the main body of this report devoted to the discussion of the obtained experimental data.

During the course of this work, the results were or are going to be presented at six scientific meetings (for specifics see the list of publications and presentations p. 1). The work completed was also described in contributions in 4 refereed journals (already published or accepted for publications), 2 papers have been submitted for publication, and since a lot of research data has not been yet described in open literature (most of the illustrations included in this report) preparation of further publications is planned in the near future.



## 2. EXPERIMENTAL SYSTEM

The experimental system as described earlier (S.S. Stuchly et al, Rev. Sci. Instr., vol. 54, 1983) has been subsequently modified to improve its accuracy and reliability and to increase the dynamic range. A block diagram of the modified experimental system is shown in Fig. 1, and a flow chart of the system operation is depicted in Fig. 2. The main modifications included: an introduction of a digital attenuator and an improved high-gain AC amplifier, as well as extensive software amendments.

Figures 3 and 4 illustrate the system linearity at the transmitter and receiver end, respectively. The linear range boundaries are incorporated into the software and are used to control the digital attenuator so that the electric-field measurements are always performed in the linear range of both the transmitter and receiver.

One of the spin-offs of this project was the development of tissue equivalent materials which are stable in time and are characterized by a long shelf life. The previously available tissue-equivalent materials had the life-time of not more than one month even if stored at low temperatures. The tissue-equivalent materials developed in our laboratory (Hartsgrove et. al., 1984 BEMS Annual Meeting) maintain their electrical and mechanical properties within a narrow desired range for at least one year and possibly more.

The implantable electric field probes have been fully characterized (M.A. Stuchly et al., IEEE Trans. BME, 1984).

The overall performance of the system has been evaluated by measuring the SAR distributions in lossy spheres and cylinders at various frequencies of interest using three types of the electric field probes (Wong et al, IEEE Trans. MTT, 1984).

The system capabilities can be summarized as follows:

- (i) The SAR measurement repeatability is better than  $\pm 0.5$  dB ( $\sim 10\%$ ), (tested on 15 runs under various conditions),
- (ii) The SAR measurement uncertainty is  $\pm 1$  dB, the main factor is the uncertainty in the probe calibration,
- (iii) After the initial arrangement of the experiment, the system can acquire the data on the electric field intensity and the SAR in over 650 locations within a model of the human body in approximately 1.5 h.

The main difficulty experienced during the development of the system has been inadequate performance of the available implantable electric field probes. Their limited sensitivity has forced us to use more complex electronic circuitry than initially anticipated. Their limitations in the frequency response and geometrical size imposed limits on the frequencies investigated. Finally, their poor mechanical properties resulted in extreme susceptibility to breakage, which in turn led to delays, when the probes were accidentally broken and replacement probes had to be purchased.

### 3. EXPERIMENTS IN THE FAR-FIELD

#### 3.1 Rationale

While the main objective of the project has been the development of the system and investigations of the SAR spatial distribution in the near-field of typical antennas, the initial investigations were undertaken in the far-field. The main goal was to determine the accuracy of the data based on the analysis of so-called block model of man. Since the information on the SAR distribution is required in addition to the average SAR for extrapolating biological responses observed in animals into the human exposure, reliability of these data is essential. As the initial experiments showed considerable differences between the measured SAR and the theoretical values, it was decided that more comprehensive investigations were well justified. Furthermore, the comparisons of the SAR averaged over the whole body and over some of the parts were also undertaken.

The far-field measurements were performed at a frequency of 350 MHz, and are being presently done at 915 MHz. The frequency of 350 MHz was selected because of a head resonance and a highly nonuniform spatial distribution of the SAR (with a maximum in the center of the head) reported for the block model of man (Hagmann et. al., IEEE Trans. MTT., vol. MTT-27, pp. 804-813, 1979). The measurements are also being presently performed at 915 MHz to confirm anticipated distributions of the SAR in the torso (based on the measurements at 350 MHz) and an increased absorption in the center of the head (as predicted by an analysis of an equivalent sphere).

### 3.2 Experimental results

Maps of the SAR within a model of the human body having the electrical properties of the average tissue have been obtained for all three polarizations of the incident plane wave. The experimental results for two polarizations are presented in two papers, one accepted (Kraszewski, et. al., IEEE Trans. MTT, 1984) for publication, and in abstracts and summaries of conference papers to be presented in 1984 (Kraszewski et. al., 1984 IEEE/MTT and 1984 BEMS, M.A. Stuchly et. al., EMC'84 and 1984 URSI/BEMS). The data not included in the above publications are illustrated in Figs. 5 - 20. Expanded figure captions are provided to illustrate various points.

A curve-fitting method has been developed to facilitate calculations of the average SAR for the whole-body and its parts from the acquired maps of local SARs. The electric-field probe cannot be positioned very close to the bottom wall of the model (the probe is introduced to the model from the top and normally is scanned down to a distance of approximately 2 cm from the bottom wall of the model). Since the model is irradiated from the bottom and the SAR decreases with the distance along the direction of propagation, it is essential to include the SAR values in the volume adjacent to the bottom wall in the calculations of the average SAR. To accomplish this task, the experimental data are extrapolated into that volume by the least-square curvefitting. In the majority of cases, e.g. in the torso, as shown in Figs. 8 and 11, the SAR follows an exponential function along the direction of the wave propagation, and therefore an exponential function is fitted into the data points and the SARs in the volume close to the model wall are

calculated (Fig. 11). Where the SAR changes in a less regular fashion, e.g. in the head or legs, other functions such as polynomials were fitted into the data. The extrapolated values of the SAR were used together with the experimentally obtained values for calculations of the averages. Uniform spacing between the measurement points used for averaging was maintained.

To calculate the whole-body average SAR the commonly used "rule of nines" (B. Ricci, Physiological Basis of Human Performance", Lea & Febiges, Philadelphia, 1967) was applied, i.e. the contributions by weight of the various parts of the human body were as follows:

head and neck	0.09
upper torso	0.18
lower torso	0.18
arms 2x0.09	0.18
upper legs 2x0.09	0.18
lower legs 2x0.09	<u>0.18</u>
	0.99

The average SARs were calculated for each body parts and than multiplied by the weighing factors and added to obtain the whole-body average. The contributions of various parts of the body to the whole-body average for two polarizations are shown in Table 1.

### 3.3 Comparison with theory

Table 2 presents a comparison between the average SAR for the whole body and the head calculated from the measured data (this work) and those calculated using the block model of man, (Hagmann et. al., 1979). Not all polarizations can be compared because of a lack of the theoretical data. Furthermore, for the wave propagation from head to toes ( $k \parallel L$ ), calculation of the averages from the measured data is of questionable meaning and utility, as the power is dissipated predominantly in the upper part of the body close to the antenna. This means that in calculating the averages it would be necessary to use extensively the extrapolated data.

The theoretical average SAR values were calculated in two ways, firstly by a simple addition of the values calculated for individual body cells (this method was used by Hagmann et. al., 1979), and secondly using cell volume weighing factors to account for the differences in the size of the cells in the block model. The cell volume ranged from approximately 17  $\text{cm}^3$  to 690  $\text{cm}^3$ .

The agreement between the experiment and the theory for the whole-body and the head average SARs is quite good. It is, within 6-13%, depending on the method of calculation of the averages.

Another comparison between the theory and experiment is shown in Fig. 17. The solid line shows the SAR averaged over horizontal layers of the body along the vertical body axis, as calculated from the measured data. The dashed line shows the SAR values calculated for the block model of man. It should be pointed out that the geometries of the two models are slightly different, and the models have their chins, rather than feet, aligned for this comparison. The agreement between the theoretical and experimental results is very good in the head, reasonable in the torso, but rather bad in the legs.

Significant differences between the experiment and the theory can be observed in the spatial distribution of the SAR as illustrated in Figs. 18 and 19.

Figures 18a and 18b show the SAR values in the head at 350 MHz for  $E \parallel L$  in two layers of cubical cells as calculated (Hagmann et. al., 1979) and dots and numbers in brackets show the locations and values of the measured SAR, respectively. If the theoretical and experimental values are relatively close in few locations, it appears to be purely coincidental. As a rule, large differences, typically by a factor of 10 to 20, are observed between the calculated and the measured values. The differences are greater for the inner layer of cells, but for  $k \parallel L$ . Similarly, large differences can be seen, however in this case the comparison is confined by the difference in the orientation of the electric field in the experiment (shoulder-to-shoulder) and the calculations (front-to-back).

Figures 19a to 19c illustrate the comparison between the calculated and measured values of the SAR in the torso, at three different depths at 350 MHz, for  $E \parallel L$ . The columns indicate the calculated values for the cells in which the measurements were made. The measured values are shown by dashed line bars. The lines on the figurines shown in the figures designate the locations of the measurement points. There again, differences of an order of magnitude are quite typical (notice that the SAR scale is logarithmic). Figure 19d depicts the same comparison for  $k \parallel L$ . Similarly to the case of the head, the results are confined by the differences in the orientation of the electric field. Nevertheless, it is striking that while it was determined experimentally, that for waves propagating from head to toe at 350 MHz the energy deposition takes place mostly in the head and the upper torso, the theory predicts comparable SARs in the lower torso to those in the upper torso. It should also be noted, that we do not find  $SAR > 1$  mW/kg for an incident power density of  $1 \text{ mW/cm}^2$  in the torso below 50 cm from the top of the head. The calculations show the SAR values between approx 10 and 100 mW/kg in the lower torso and the legs. Such striking differences cannot possibly be attributed to the difference in the orientation of the electric field.

The differences in the actual (measured) and the predicted SAR distribution are probably best illustrated in Figs. 20a to 20c. In the torso, at 350 MHz for the E polarization the wave is attenuated exponentially, and the SAR decreases by a factor of over 10, from its value at the surface facing the source, within the first 5 cm or so. However, the theory predicts the



SAR greater or comparable in the center cell layer to those in the outer layer. The differences in the SARs averages over the layers for the measured and the calculated data are large, over an order of magnitude.

### 3.4 Discussion and main findings

Very good symmetry with respect to the main axis of the body in terms of the SAR values was confirmed in our measurements, as illustrated in Figs. 5 and 6 for two polarizations, namely  $E \parallel L$  and  $H \parallel L$  (where  $L$  is the main body axis). This allowed us to limit the scanning to one half of the model.

For all polarizations at 350 MHz the SAR decreases with distance from the body surface in the direction of the wave propagation for the body parts whose dimensions are comparable with the wavelength. This is particularly well illustrated for the  $E$  and  $H$  polarizations ( $E \parallel L$ , see Fig. 8, and  $H \parallel L$ , see Fig. 9). Furthermore, the decay is exponential (Fig. 12), with the attenuation coefficient equal to that of a planar model having the electrical properties of tissue-equivalent material. In case of the  $k$  polarization (propagation from head-to-toes) a rapid SAR decrease occurs in the head within the first 10 cm along the direction of propagation (Fig. 7).

The SAR distribution in the head, neck and the limbs is highly nonuniform. For all polarizations there is a maximum of the SAR in the neck region, although the magnitude of the maximum is different for various

polarizations (Figs. 7, 13a, 13b). The greatest SAR in the center of the neck is for the E polarization, with the SAR 100 mW/kg per 1 mW/cm<sup>2</sup> of the incident power density. While in most cases, the highest values of the SAR are on the body surface facing the antenna, this is not the case for the neck (Fig. 15).

Increased absorption above the knee can also be observed for the E and H polarizations.

In case of the k polarization and the propagation from head-to-toes at 350 MHz, the distribution of the SAR can best be described as "a man in the shower". Maximum values of the SAR in this case are on the body surfaces facing the antenna perpendicular to the direction of the wave propagation, with the head providing a "shadow" for parts of the upper torso.

The distribution of the SAR in the head closely resembles that in a sphere of the equivalent size and electrical properties for the E and k polarizations. However, a case of the head resonance at 350 MHz, as predicted by the theory, has to be viewed with circumspection. The SAR values inside the head are not greater than at the surface.

The SAR averaged over the horizontal body layers and the whole-body average are not significantly different for the E and H polarizations except in the neck, (Fig. 16, Table 1). The whole-body averages are in a relative-

ly good agreement with the values calculated for spheroidal models of the average man (the Radiofrequency Dosimetry Handbook, second edition). However, the differences up to about 30% exist, which is not surprising in view of differences in shape. More importantly, the whole-body average at 350 MHz is greater for the H polarization than for the E polarization. According to the spheroidal-model data such behaviour is characteristic at higher frequency (above 600 MHz for an average man).

Our data on the SAR distribution is in a very good agreement with the experimental data obtained by the thermographic technique (for details see Kraszewski et. al., IEEE Trans. MTT, 1984 accepted).

On the other hand, a good agreement with the theoretical data obtained for the block model occurs for the whole-body average SAR (Table 2), only reasonable agreement for the SAR averaged over the layers perpendicular to the body axis (Fig. 17), and a lack of agreement for the spatial distribution of the local values of the SAR (Figs. 18, 19, 20).

### 3.5 Conclusions and future research plans

The spatial distribution of the SAR in a full-size homogeneous model of man has been measured at 350 MHz for three orthogonal polarizations of the incident electromagnetic field. The whole-body average SAR has been calculated where such calculations were meaningful. From the comprehensive experimental data obtained the following conclusions can be drawn:

- (i) The spatial distribution of the SAR is highly non-uniform, with the SAR typically varying within at least three orders of magnitude. Very large gradients of the SAR occur along the direction of wave propagation. Even greater non-uniformities can be expected in the actual human body which is electrically inhomogeneous.
- (ii) At a frequency of 350 MHz, and anticipated at higher frequencies, the SAR in the torso exhibits exponential decay in the direction of the wave propagation, with the exponent equal to that of the planar model having the electrical properties of the tissue. This indicates that, with some restrictions, the principles of geometrical optics can be applied to determine the SAR distribution in the torso at frequencies lower than previously predicted.
- (iii) The neck-head region constitutes a rather complex geometry and the resulting SAR distributions are difficult to predict are highly non-uniform and frequency dependent.
- (iv) Theoretical analysis of the block model of man consisting of about 340 cells does not provide adequate data on the SAR distribution, even approximately, at frequencies equal and greater than 350 MHz.

Further experimental investigations should address the following questions:

- (i) Does the exponential behaviour of the SAR occur also at higher frequencies ( $f > 350$  MHz)?
- (ii) Can the approximation of the head by an equivalent lossy sphere be used to determine the frequencies at which the SAR in the head center is greater than on the surface?
- (iii) Does the block-model of man provide more reliable information on the spatial distribution of the SAR at frequencies below 350 MHz, particularly close to the whole body resonance at 80 MHz? (As the cell size as compared to the wavelength becomes smaller as the frequency decreases, the block model provides a better approximation of the human body).
- (iv) What is the effect of the non-homogeneous tissue properties of the SAR distribution?

#### 4. EXPERIMENTS IN THE NEAR-FIELD

##### 4.1 Experimental results

All near-field experiments were performed at a frequency of 350 MHz for three antennas, a resonant dipole in free space, a resonant dipole over the ground plane and a resonant slot. These antennas were selected to represent important exposure situations, namely portable transmitters and leakage fields.

All the antennas were designed to be well matched in the free space and with the human model in the vicinity ( $VSWR < 1.2$ ). The antennas were placed approx. 8 cm from the model surface at various locations along the vertical axis. All the SAR values are normalized to 1 W input power to the antenna.

Figures 21 to 27 provide the data on the spatial distribution of the SAR in three cross-sections of the model of the human body. The cross-sections are located in the center ( $z=10$  cm), and 5 cm off center, toward the front ( $z=5$  cm), and toward the back ( $z=15$  cm). The values shown are averages of three to five independent measurements. The following antennas and their positions were investigated:

- (i) dipole, E  $\parallel$  L placed 156.5 cm (Fig. 21a)  
137 cm (Fig. 21b), and 103 cm from the base (feet)  
of the model (Fig. 21c)
- (ii) dipole, H  $\parallel$  L, placed at 137 cm (Fig. 22)
- (iii) dipole, k  $\parallel$  L, 14 cm above the head (Fig. 23)

- (iv) resonant dipole ( $\lambda/2$  dipole above the ground plane)  
E  $\parallel$  L (Fig. 24), H  $\parallel$  L (Fig. 25), and k  $\parallel$  L (Fig. 26)
- (v) slot, E  $\parallel$  L, placed at 87 cm from the model base (feet)  
(Fig. 27).

The spatial distribution of the SAR in various locations along two body axis and averaged over the tissue volume perpendicular to the direction of propagation is shown in Figs. 28 to 30. Figure 28 illustrates the SAR distribution for three locations of the dipole along the vertical body axis ranging from the head to the waist for E  $\parallel$  L. Figures 29 and 30 provide the same data for a resonant dipole and slot, respectively.

The distribution of the SAR averaged over horizontal tissue layers along the body vertical axis is shown in Figs. 31 to 35, for the dipole (Figs. 31 and 32), resonant dipole (Figs. 33 and 34) and the slot (Fig. 35).

The changes in the local values of the SAR along the direction of wave propagation are illustrated in Figs. 36 to 41. Figures 36 to 39 show the local values of SAR as a function of the distance along the direction of the wave propagation, the mean SAR for a given location (averaged over the body dimension along the direction of propagation) and the whole-body averaged SAR for various antennas. The least-square fit curve and its parameters are also shown on each figure. The fitting line is described by the equation:

$$\text{SAR} = A \exp (-Bz)$$

Figures 40 and 41 show the local SAR values along the direction of propagation for the antenna above the head of the human body model, and the wave propagation from head to toe.

The whole-body average SAR and average SARs for various body parts were calculated following the same procedure as described in the earlier part of this report for the far-field. The results are summarized in Table 3.

#### 4.2 Comparison with theory

Our experimental data can be compared with calculations performed using the block model and the method of moments solution of the tensor integral equation. This solution was published for a resonant dipole radiating at a frequency of 200 MHz (R.J. Spiegel, IEEE Trans. MTT., vol. 30, pp. 177-185, 1982), and the calculations at 350 MHz were performed by Dr. Spiegel upon our request.

The calculations were done for a block model consisting of 180 cells (total for the whole body) and for the E polarization ( $E \parallel L$ ). The essential parameters were identical for the calculations and the measurements as summarized in Table 4. Some minor, nonessential differences can be noticed, e.g. the experimental dipole had to be shortened to ensure impedance matching to the source.

The whole-body average SARs calculated and measured are relatively close, 7.9 and 7.8 mW/cm<sup>2</sup>, respectively. The difference can be easily attributed to the difference in the distance of the dipole from the body surface (7.3 cm vs. 8 cm).



In view of the limited number of cells in the block model (90 cells for half of the body) and our experience in the far-field, we decided to compare SAR values averaged over limited volumes rather than the local values.

Figure 42 gives a comparison of the SAR values averaged over the horizontal tissue layers along the main axis. Both the theory and the experiment indicate maximum mean SAR in the neck region, not on the dipole axis, which is below, on the shoulder level. However, the SAR values at the maximum are different by a factor of about three. The differences in the SAR values in other locations are of about the same order of magnitude.

Figure 43 gives a comparison of the SAR values averaged along the direction of wave propagation. The differences here are similar to those in the previous comparison, generally within a factor of three to five.

Large differences, however can be noted in the SAR along the direction of propagation in the torso on the dipole axis, as shown in Fig. 44. Experimental data shows that the SAR decreases exponentially with the wave penetration distance from the surface of incidence ( $z=20$  cm). The SAR is below one hundredth of the value on the surface at distances from the surface greater than 10 cm. However, according to the calculations the SAR in the cells about 14 cm from the surface facing the dipole (the third layer of cells) is only about 2 times smaller than in the first layer of cells on the antenna side.

The comparison of the experimental data with the calculations for the block model of man underscores the limitations of this theoretical analysis for the near-field exposures. This conclusion is the same as the one reached after the comparison of the far-field data. The inaccuracies in the calculations are inherent in the method employed and the size of the cells, as clearly indicated by Dr. Spiegel. Differences in the shape of the human body models and antenna parameters appear to play only a secondary role.

#### 4.3 Discussion and main findings

The spatial distribution of the SAR in the body cross-sections is highly non-uniform for all antennas and their locations as illustrated in Figs. 21-27. The highest SARs are nearly, but not always on, the axis of the antenna. When the antenna is positioned close to the head-neck region and for the E polarization, the maximum SAR is shifted off the dipole axis towards the head (Figs. 21a, 21b, 24). This feature is characteristic for both dipoles, the resonant dipole and the resonant dipole above the ground plane. However, for the H and k-polarizations the maximum SAR is on the axis of the dipole. The same holds when a dipole radiating with the E-polarization is placed close to the lower torso.

A comparison of the SAR maps for the E and the H-polarization (Figs. 21b and 22) shows that larger SAR gradients exist for the E polarization, notwithstanding the fact that the whole-body average SAR is very close for the two polarizations, namely 7.8 mW/kg for the E and 6.6 mW/kg for the H-polarization (Table 3).

A resonant dipole above the ground in the E polarization (Fig. 24) gives a very similar SAR map to that of a resonant dipole in free space (Fig. 21b) with the SAR values greater by the factor of approximately two, as expected because of the increase in the gain. It can also be noted, that the increase in the whole-body average SAR is also about twice (Table 3). The same observation applies to the H polarization, as shown in Figs. 22 and 25. In case of the k-polarization, Figs. 23 and 26, the increase in the SAR values is somewhat less than two times when the dipole is placed above the ground. The gain for the dipole in free space and above the ground plane is 1.64 and 3.28, respectively.

A half-wavelength resonant slot radiating in the E polarization (Fig. 27) deposits the energy more uniformly than a dipole (Fig. 21c) in the horizontal plane of the body. For the slot in the plane of its axis and nearby, the SARs on the body vertical axis and 10 cm off the axis are very close (Fig. 27).

The non-uniform distribution of the SAR is further illustrated in Figs. 28-30. These figures show the SAR values in various body locations. The SAR was calculated as the mean value of the volume having the probe diameter (9 mm) and extending from the body front to the back. Several features, of the way the energy is deposited in the body, can be observed here. The maximum mean values of the SAR is about 100 mW/kg per 1 W of the input power for the dipole in both the E and H polarizations (Figs. 28, 29), but only about 20 mW/kg for the slot (Fig. 30). The maximum is on the antenna axis, except when the antenna is located close to the neck (Figs. 28a, 28b).

The slot (Fig. 30) creates a broader SAR maximum in both directions. It can also be observed that for the dipoles, and to a lesser degree for the slot, the changes of the mean SAR along the vertical body axis are quite rapid, more than an order of magnitude within 10 cm being typical.

The RF energy is highly non-uniformly absorbed along the vertical body axis, even when averaged over the horizontal tissue layers, as illustrated in Figs. 31-35. Figures 31a, 31b and 33 clearly show that also the maximum of the mean SAR is shifted toward the neck region, off the axis of the dipole, for both types of dipoles, for the E-polarization. Also for the slot in the E-polarization located in the lower torso region, a small increase in the SAR occurs in the neck. The SAR value is small-though (approx. 3 mW/kg) as compared with the maximum (20 mW/kg), as shown in Fig. 35. The maximum mean SAR for the dipole above the ground plane is higher for the E and H polarizations than for the dipole in free space, but not two times (Figs. 31b and 33, 32 and 34).

One of the most important findings is that the SAR decreases exponentially in the direction of the wave propagation at a frequency of 350 MHz and for the E- and the H-polarization. This behaviour is analogous as for the exposure in the far-field. When an exponential curve is fitted into the experimental data points, as shown in Figs. 36-39, only at distances greater than approx 12 cm from the surface upon which the wave is incident, departure of the experimental results from the fitting line can be observed. Furthermore, at those distances the SAR is more than one hundred times below the maximum value on the surface, ten or more times below the mean value for the locations, and three to five times below the whole-body average.

The maximum SAR consistently appears at the body surface, although its vertical location may vary depending on the antenna location, as underlined earlier when the antenna is in the neck region the location of the maximum along the vertical axis shifts toward the neck. The value of the maximum is over 1 W/kg per 1 W of the antenna input power for the dipole in free space, and over about 2 W/kg for the dipole above the ground plane, as summarized in Table 5. It should be noted that the maxima for the E polarization and  $x=137$  cm listed in Table 5 do not represent the maxima along the vertical axis, which explains their lower values.

The attenuation coefficient is very close for all the situations analysed (Table 5), and furthermore is very close to the theoretical value of -0.495, calculated from the electrical properties of the tissue phantom material. It should also be pointed out that the three standard deviations for the attenuation coefficient, as listed in Table 5, are very small, not more than 5%.

When the antenna is positioned above the head, as in Figs. 40 and 41, the distribution of the SAR along the direction of propagation is more complex. Nevertheless, a nearly exponential decrease within the first few centimeters, (about 10 cm), is evident. An increase absorption in the neck can again be observed, although the SAR values are about 10 times below those on the surface (the top of the head). Similarly, like in the far-field, the exposure situation can best be described by a term "a man under the shower" (see Figs. 23, 26, 40, 41).

The average SAR in various parts of the body, as expected, depends on the position of the antenna with respect to the body and to a certain extent on the polarization as illustrated by the data summarized in Table 3. Whenever an antenna irradiating the body in the E-polarization is placed close to the neck, the head-neck SAR is significantly increased, but the increase does not occur for the H-polarization. This is clearly visible in Table 3 for the dipole, and  $x=137$  cm ( $x$  is the distance of the dipole axis from the base (feet) of the model).

The whole-body average SAR is mainly determined by the antenna gain, and to a much lesser degree by the antenna location. The dependence on the antenna location basically reflects the dependence on the average distance to the body surface (it should be noticed that the antenna axis was always 8 cm from the body surface, but because of the body curvature the distance between the antenna aperture and the body surface varied for different antenna positions and polarizations).

#### 4.4 Conclusions and future research

The spatial distribution of the SAR in a full-scale homogeneous model of man at 350 MHz and three polarizations of the incident wave has been measured and analyzed for three antennas in the near field. The whole-body average, the body parts and selected volumes SARs have been calculated. The antennas selected represent typical practical situations, such as portable transmitters and leaky RF transmitter cabinets or similar hardware. Furthermore, the linear antennas (dipoles) are the only antennas suitable for theo-

retical analyses. The following conclusions can be drawn on the near-field exposure:

- (i) The spatial distribution of the SAR is highly non-uniform in at least two and frequently in all three directions. Typically differences between the maximum SAR and the whole-body average SAR are as 1000 to 7 (140 to 1).
- (ii) At 350 MHz, and anticipated at all higher frequencies, for all antennas investigated, the SAR decreases exponentially with the distance from the body surface upon which the wave is incident. The attenuation coefficient is very close to that of a plane-wave incident upon a half-space having the same electrical properties as the body tissue. This is a very important finding, as it shows that a simplified analysis can be employed to determine the relative SAR distribution in the direction of propagation (at least for the E and H-polarizations) for multilayered (skin, fat, bone, muscle) models of human body. Still more sophisticated analysis has to be used to find the absolute values of the SAR, as these depend on the antenna type, position, polarization and distance from the body.
- (iii) For the E-polarization there is a tendency for the maximum absorption to shift toward the neck region if the antenna is nearby that region, and a small increase in the SAR occurs for other antenna positions.

- (iv) The relative spatial distribution of the SAR depends mainly on the antenna position and polarization as well as type (e.g. dipole vs. slot), but the whole-body average SAR is basically determined by the antenna gain and the distance from the body.
- (v) The block model of man consisting of 180 cells does not provide adequate data on the SAR distribution at frequencies equal and greater than 350 MHz.

Further experimental investigations should address the following:

- (i) Confirmation of the conclusions drawn for frequencies above 350 MHz, at least one more frequency (915 MHz).
- (ii) Determination of the lower bound of frequency for which the SAR decreases exponentially in the direction of wave propagation.
- (iii) Investigations of such practical antennas as a short helix and a monopole (whip), which are used in portable transmitters.

Our final question related to the near-field exposure maybe worth addressing. According to the ANSI recommendations (ANSI C95.1-1982), the upper limits for near-field exposures are the average SAR (whole-body) of 0.4 W/kg and the spatial peak SAR 8 W/kg as averaged over 1 g of tissue. At a frequency of 350 MHz the output power of portable transmitters should not exceed 25 W for the average SAR to be above the limit for practical distances of 7 to 10 cm for the antenna separation from the body surface. However,



only about 4 W appear to be sufficient for exceeding the spatial peak SAR. Whether this condition should apply when the peak SAR is on the body surface is a separate question.

Table 1

Average specific absorption rates in various part of a full-scale  
model of man exposed to a plane-wave of  $1 \text{ mW/cm}^2$  at 350 MHz

Body part	SAR (mw/kg)	
	E    L	H    L
head & neck	93.8	41.2
upper torso	11.2	26.8
lower torso	17.0	31.1
arms	36.0	68.9
legs	55.5	56.9
whole body	40.0	47.0

Table 2

Comparison of the specific absorption rat. (SAR)  
(normalized to 1 mW/cm<sup>2</sup> in the head and the whole body):  
calculated for the block model and experimental results (this work)  
frequency 350 MHz, polarization E // L

SAR [mW/kg]	Calculated	Measured
Head (1)	108.0	102.2
Head (2)	98.2	93.8
Whole-body (1)	44.5	40.2
Whole-body (2)	46.2	40.0

- (1) Straight summation  
(2) Weighted by volume factor

Table 3

Near-field experiments. The whole-body average SAR (mW/kg) and average SARs (mW/kg) for body parts,  $f=350$  MHz, input power to the antenna 1 W

Body part	Antenna configuration						Dipole above ground plane x=137 cm		Slot E IL, x=87 cm
	Dipole								
	E IL, x=157.5cm	E IL, x=137cm	E IL, x=103cm	H IL, x=137cm	E IL	H IL			
Head & neck	78.7	45.0	0.2	4.5	86.7	7.7	1.6		
Upper torso	2.8	13.7	6.6	30.8	42.9	65.0	0.4		
Lower torso	1.5	1.9	32.4	0.5	3.3	0.7	14.5		
Arms	2.4	2.9	5.0	2.5	6.6	5.1	12.3		
Legs	0.6	0.7	0.4	0.2	1.5	0.2	4.5		
Whole body	8.5	7.8	8.1	6.6	17.8	13.5	6.7		

Table 4

Exposure conditions for the experiment and the parameters for  
the block model calculations in the near-field

PARAMETER	EXPERIMENT	CALCULATIONS
Frequency (MHz)	350	350
Nominal dipole length	$\lambda/2$	$\lambda/2$
Actual dipole length	$0.43\lambda$	$0.5\lambda$
Dipole length/radius	117	200
Input impedance ( $\Omega$ )	50	48.3
Distance from the body (cm)	8	7.3
Model height (cm)	175	170
Dielectric constant	37	37
Conductivity (S/m)	0.954	0.954

Table 5

Maximum and mean specific absorption rate SAR along the direction  
of propagation, SAR, and the attenuation coefficient for  
antennas in the near-field

Antenna	Polarization	$x^1$ (cm)	SAR(mW/kg)			$B^2$
			Max	Mean	WB Ave.	
Dipole	E	103	$1090 \pm 86^3$	100	8.1	$-0.567 \pm 0.011^3$
	E	137	$494 \pm 32.5$	50	7.8	$-0.464 \pm 0.009$
	H	137	$1053 \pm 193$	96	6.6	$-0.515 \pm 0.027$
Dipole above ground	E	137	$1291 \pm 330$	139	17.8	$-0.464 \pm 0.012$
	H	137	$2632 \pm 516$	247	13.5	$-0.503 \pm 0.024$

<sup>1</sup> x is the distance of the antenna axis from the model feet

<sup>2</sup> B is the attenuation coefficient, see also Figs. 36-39  
(the attenuation coefficient for the infinite half space irradiated  
by a plane wave is  $B = 0.49 \pm 0.02$ )

<sup>3</sup> shows three standard deviations

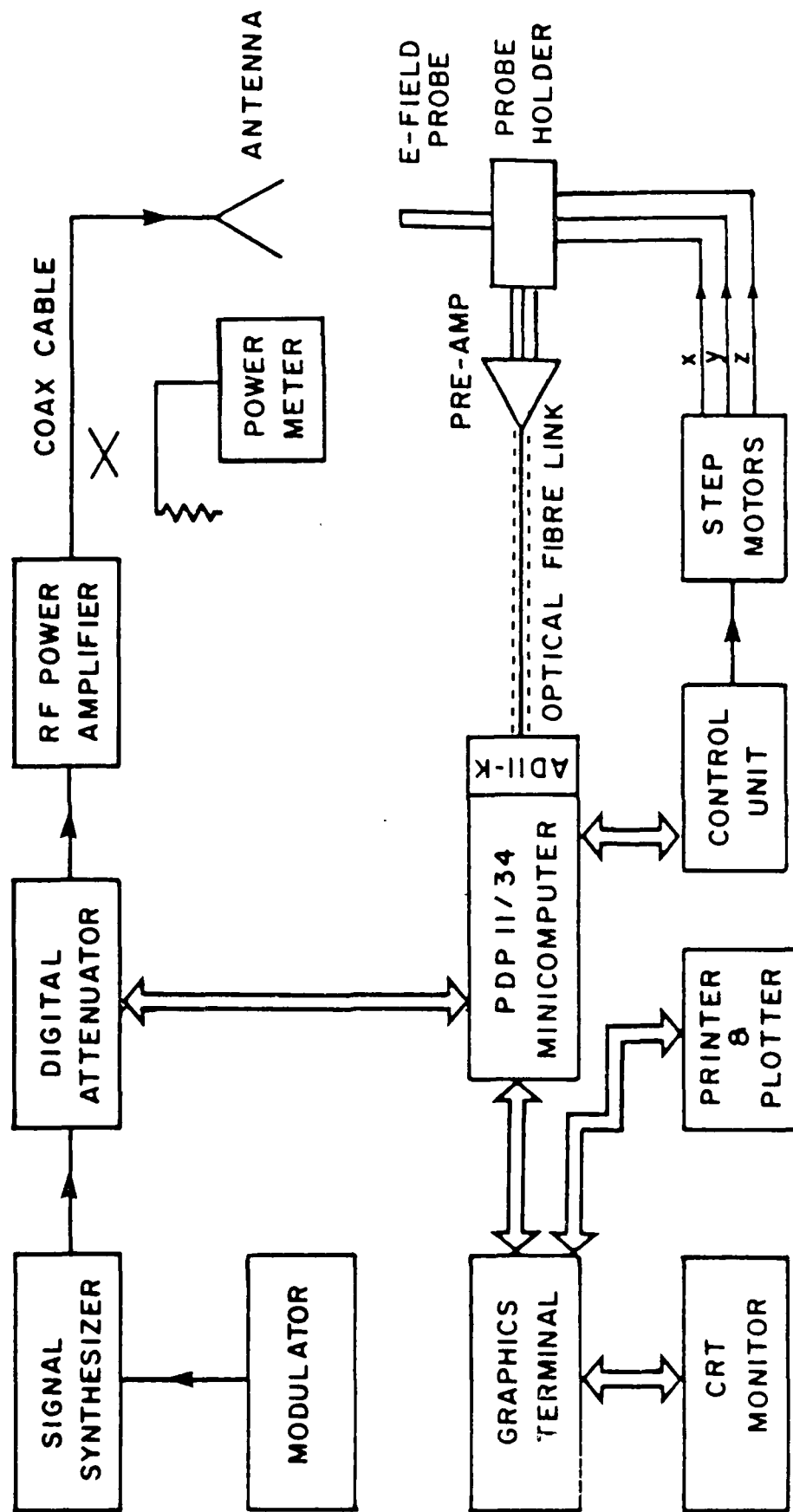


Figure 1 - Schematic diagram of the modified experimental system for the acquisition, display and recording of the SAR distributions in 1-scale models of the human body.

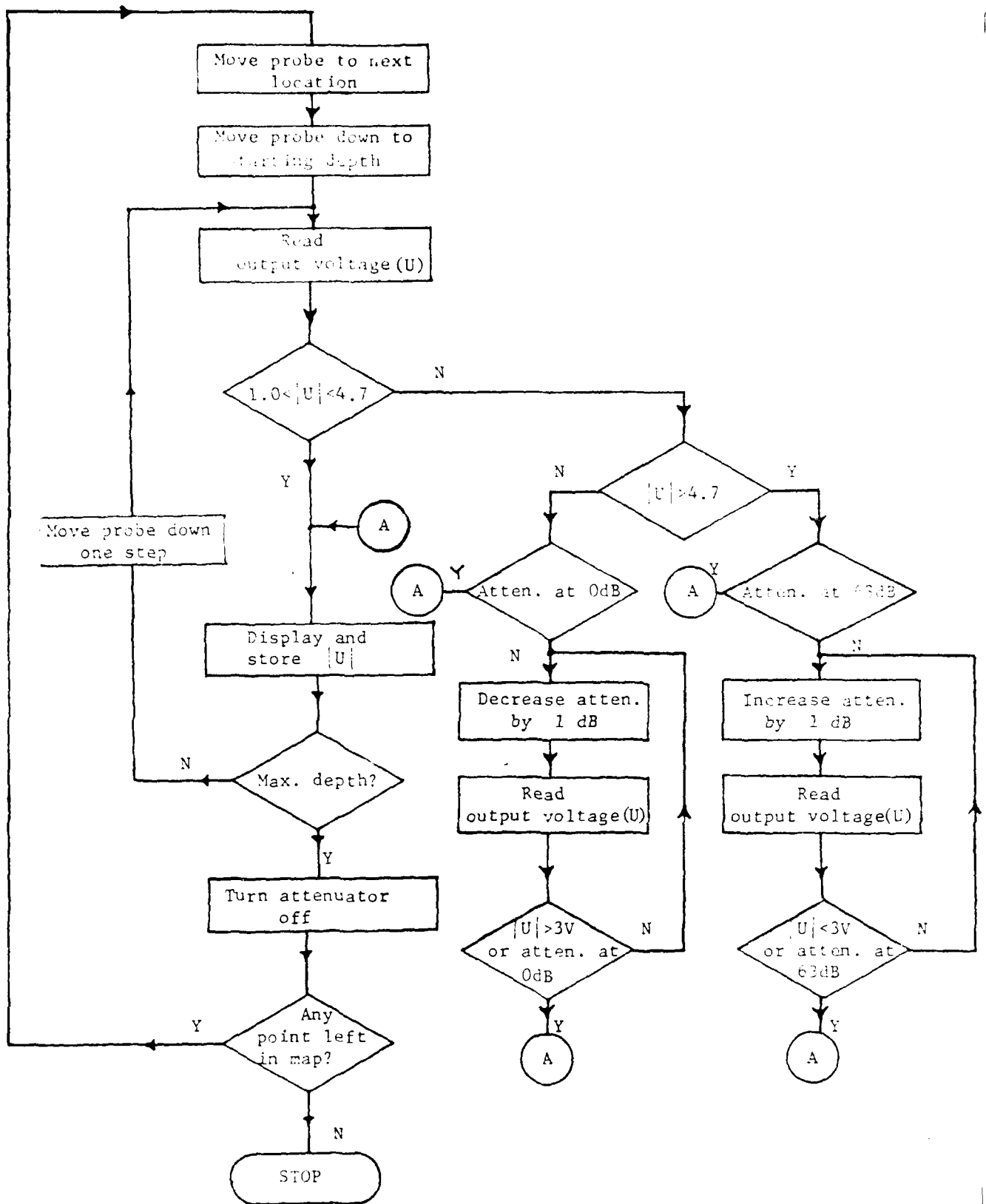
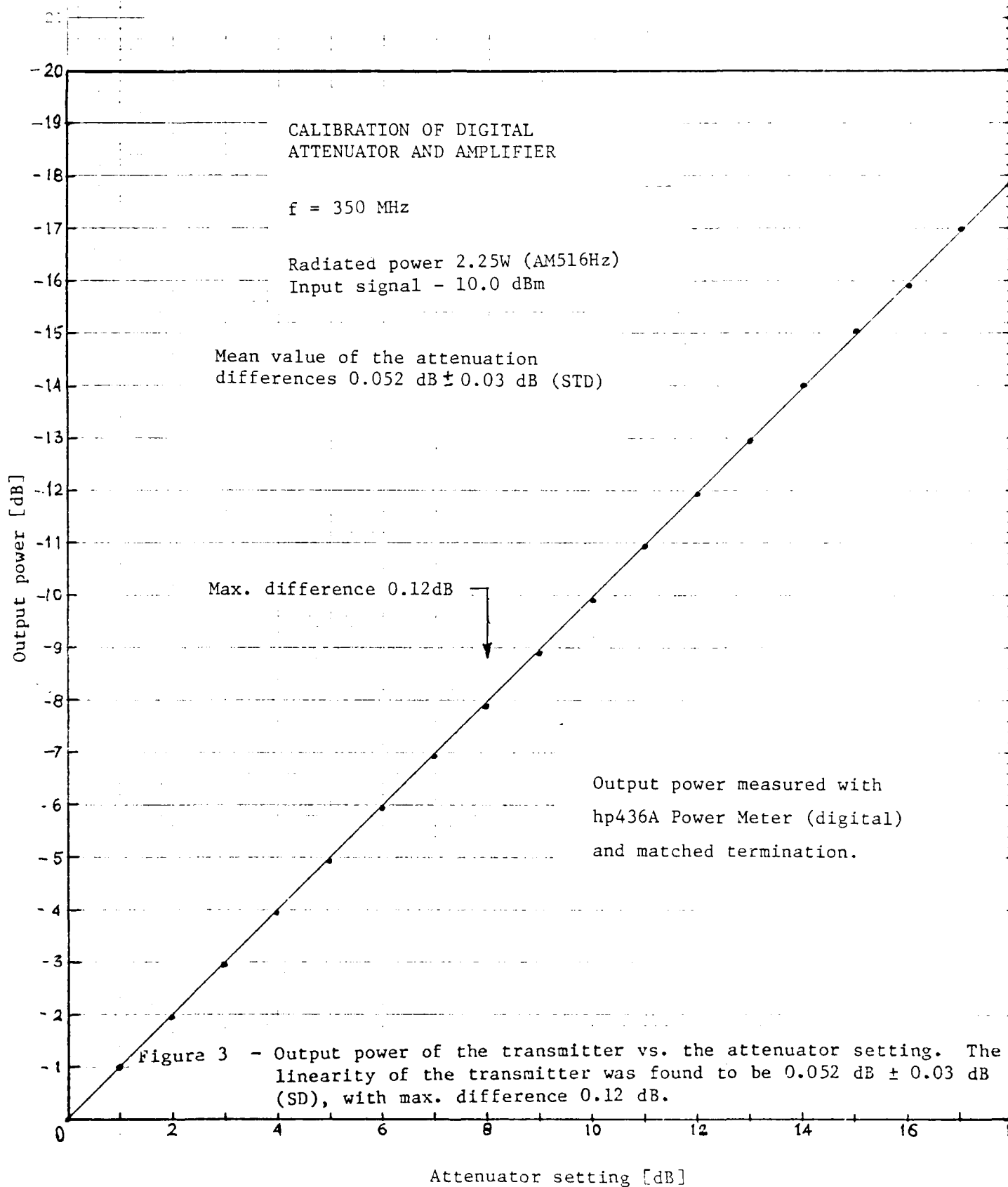


Figure 2 - Flow chart of the modified experimental system from Fig. 1.





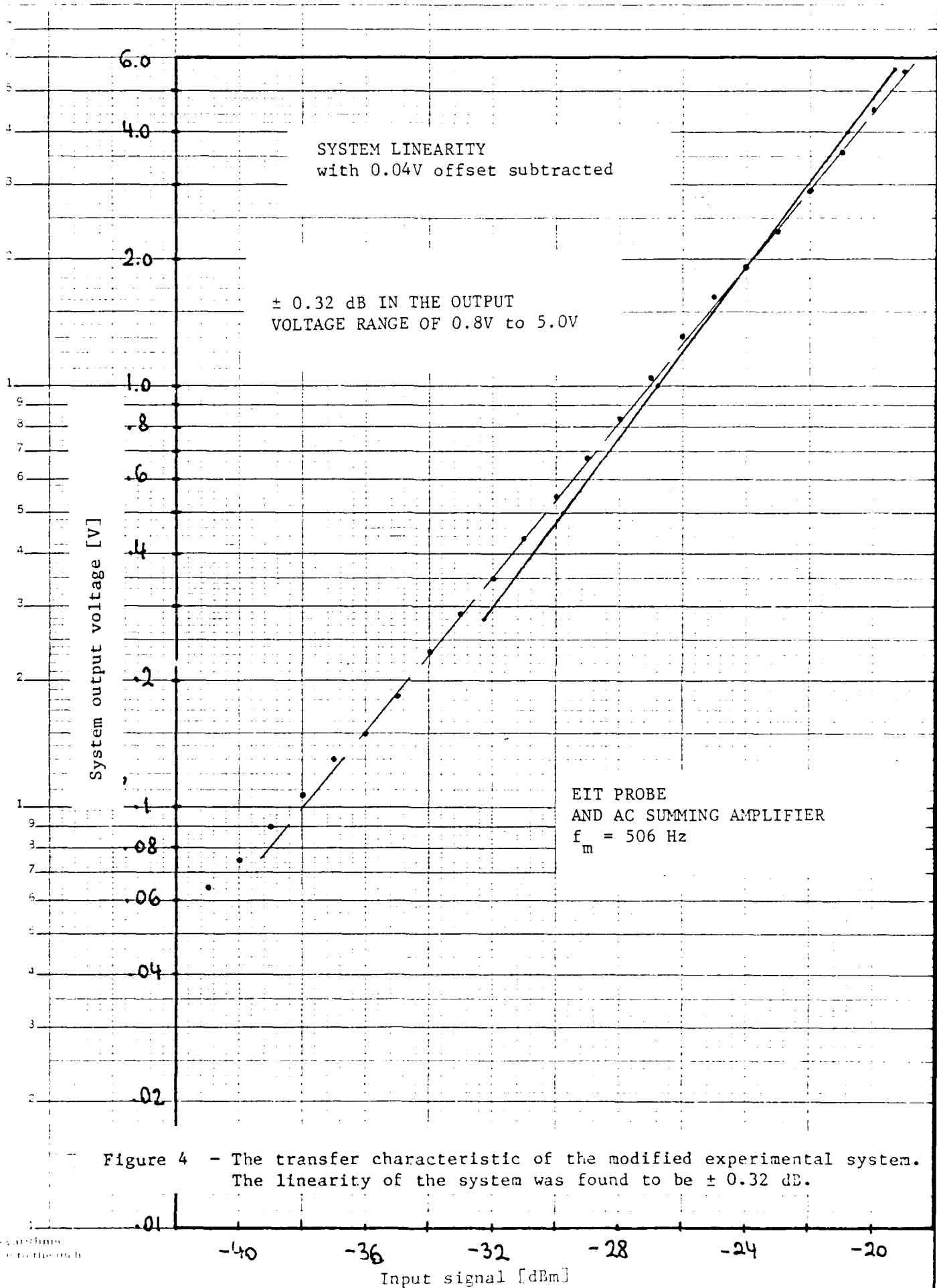


Figure 4 - The transfer characteristic of the modified experimental system. The linearity of the system was found to be  $\pm 0.32$  dB.

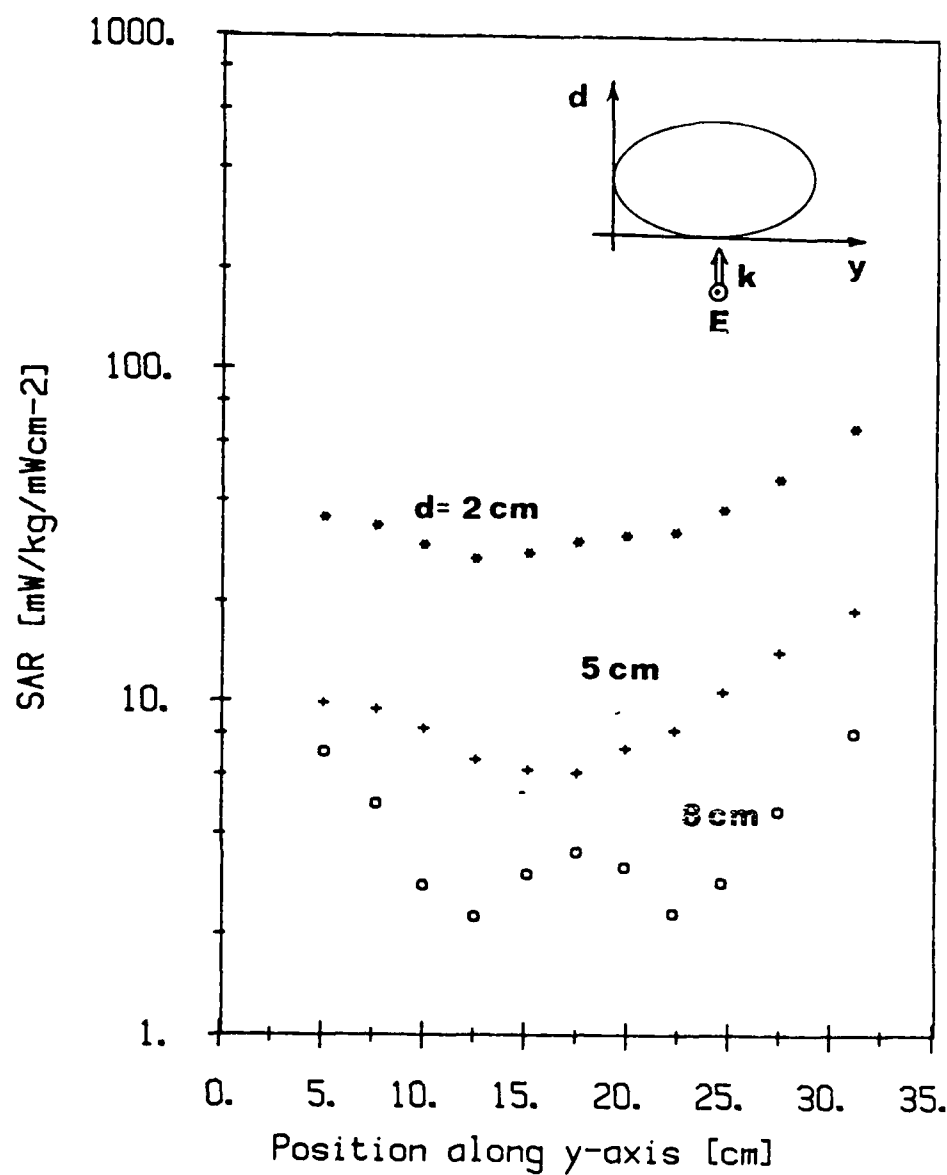


Figure 5 - Far-field experiments. The specific absorption rate (SAR) (normalized to  $1 \text{ mW/cm}^2$ ) in the torso at three locations vs. position across the torso; frequency 350 MHz, polarization  $E \parallel L$ .

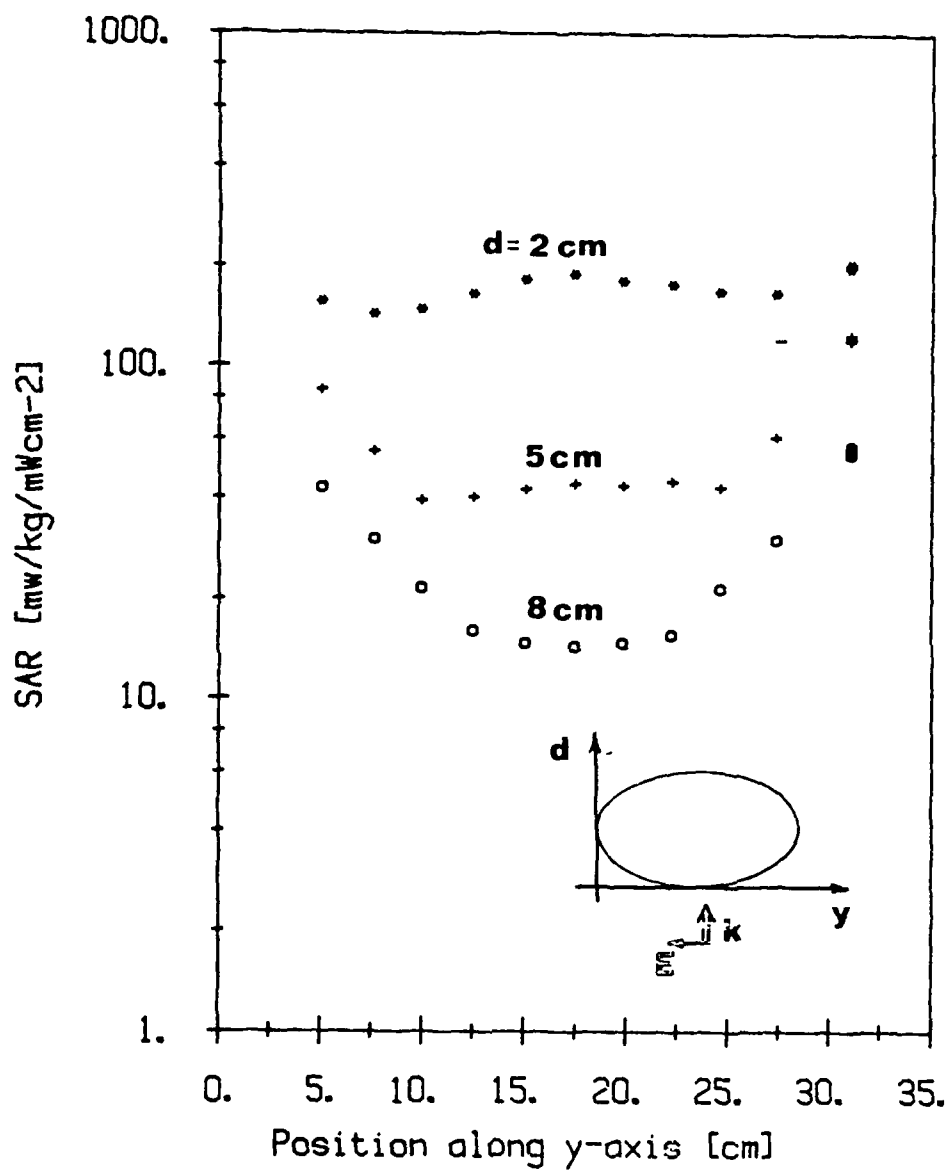


Figure 6 - Far-field experiments. The specific absorption rate (SAR) (normalized to  $1 \text{ mW/cm}^2$ ) in the torso at three locations vs. position across the torso; frequency 350 MHz, polarization H || L.

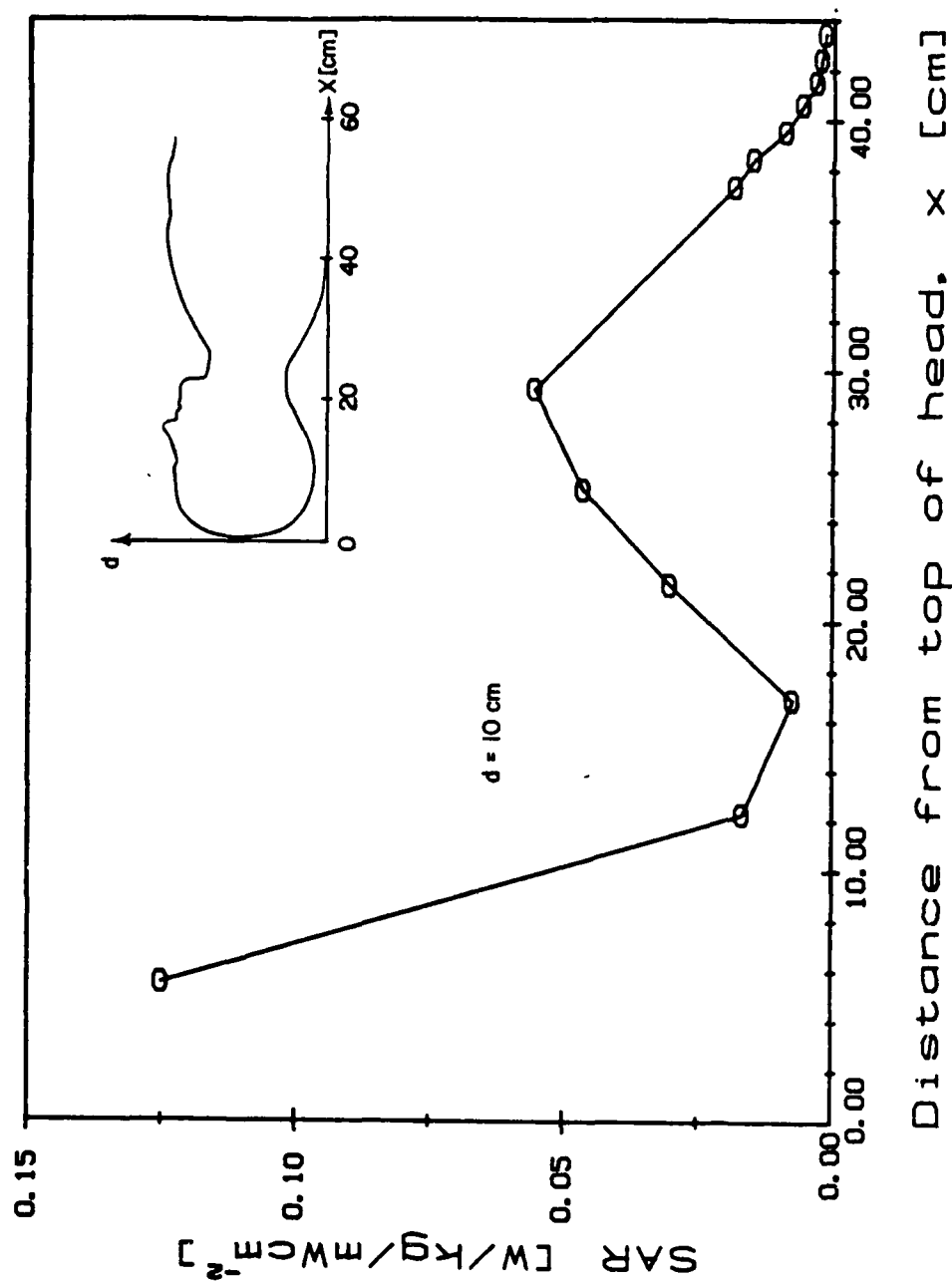


Figure 7 - Far-field experiments. The distribution of the specific absorption rate (SAR) (normalized to 1 mW/cm<sup>2</sup>) along the main axis of the body; frequency 350 MHz, polarization  $k \parallel L$ .

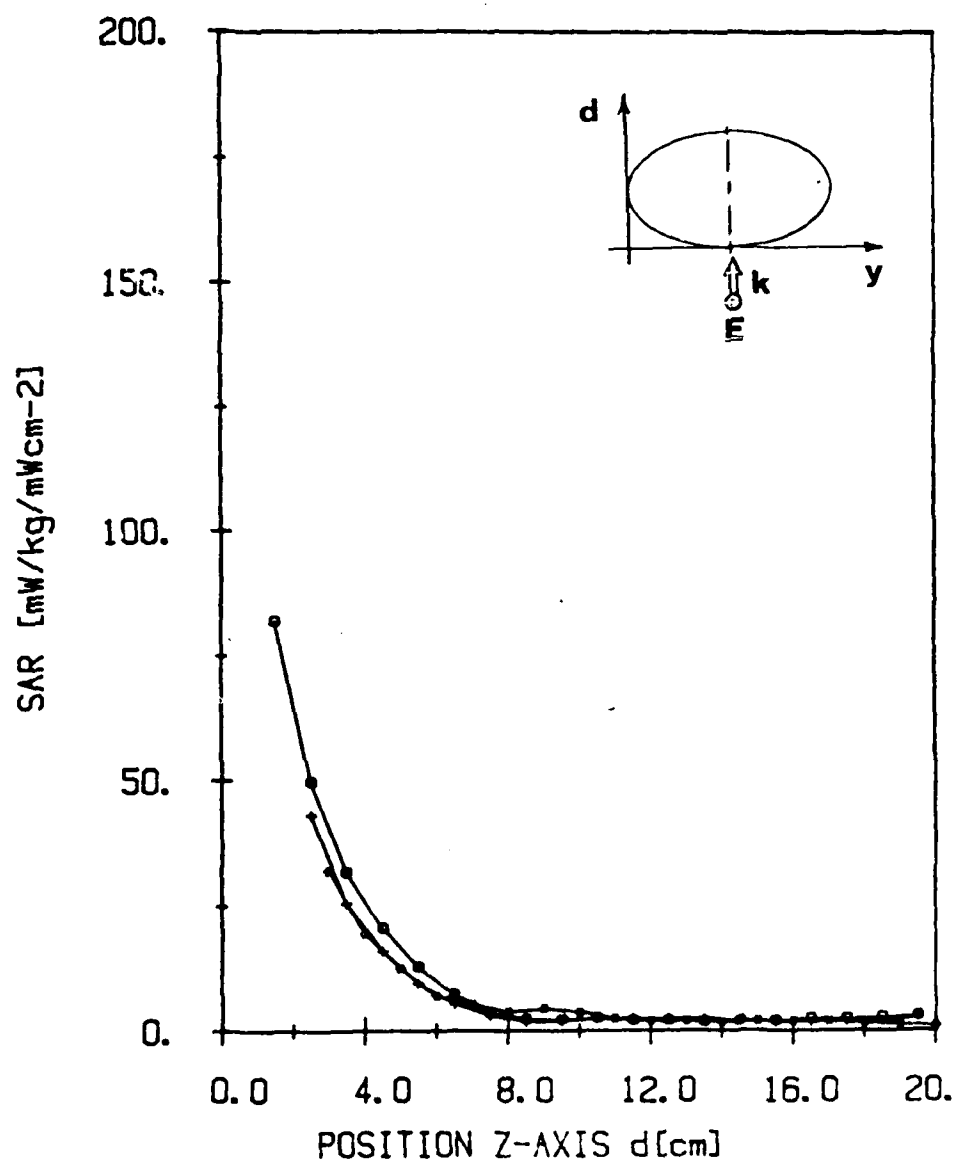


Figure 8 - Far-field experiments. The specific absorption rate (SAR) (normalized to  $1 \text{ mW/cm}^2$ ) in the torso vs. the distance from the body surface at which the wave is incident for three position:  $x = 96 \text{ cm}$ ,  $+ x = 117 \text{ cm}$  and  $* x = 137 \text{ cm}$  from the base (feet). Frequency: 50 MHz, polarization  $\mathbf{E} \parallel \mathbf{L}$ .

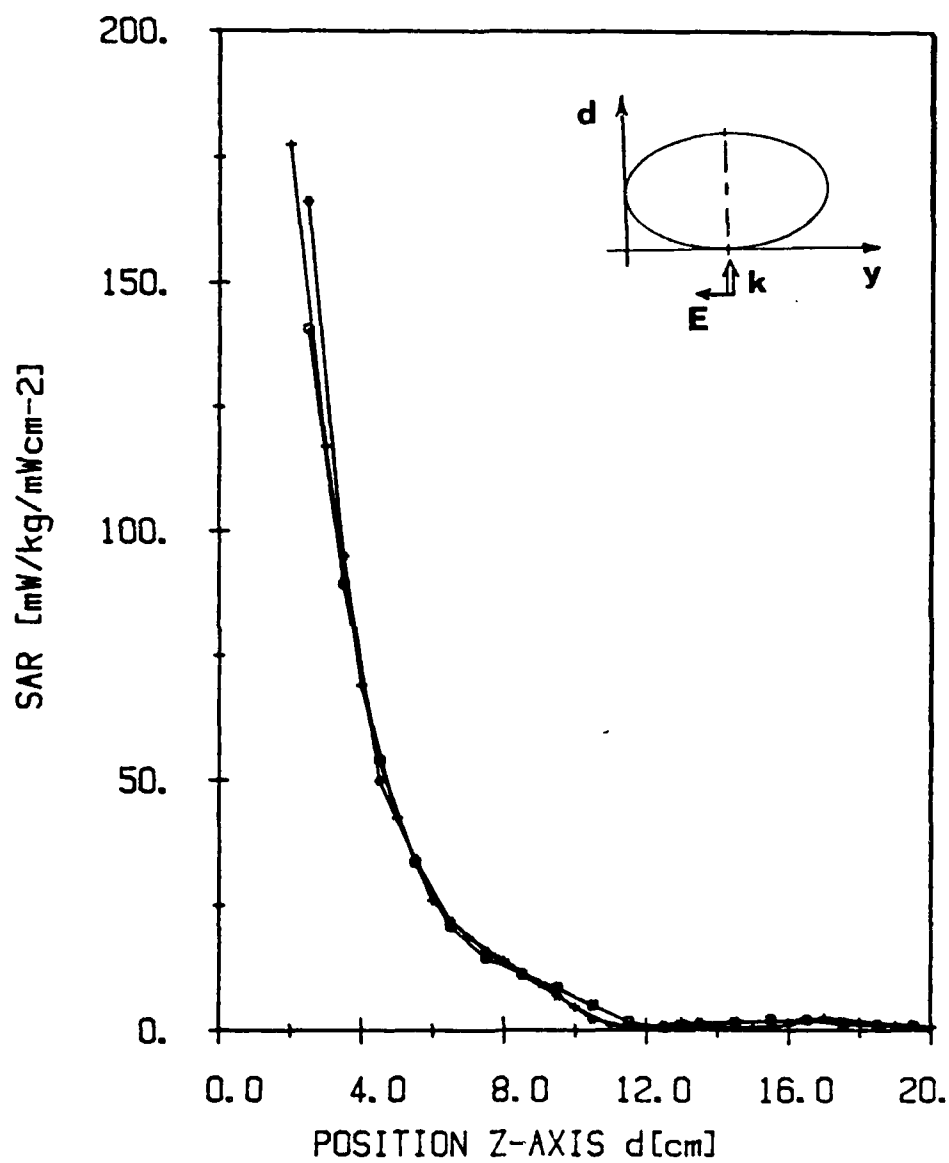


Figure 9 - Far-field experiments. The specific absorption rate (SAR) (normalized to  $1 \text{ mW/cm}^2$ ) in the torso vs. the distance from the body surface at which the wave is incident for three position:  $x = 96$  cm,  $+ x = 117$  cm and  $* x = 137$  cm from the base (feet). Frequency 350 MHz, polarization  $\mathbf{H} \parallel \mathbf{L}$ .

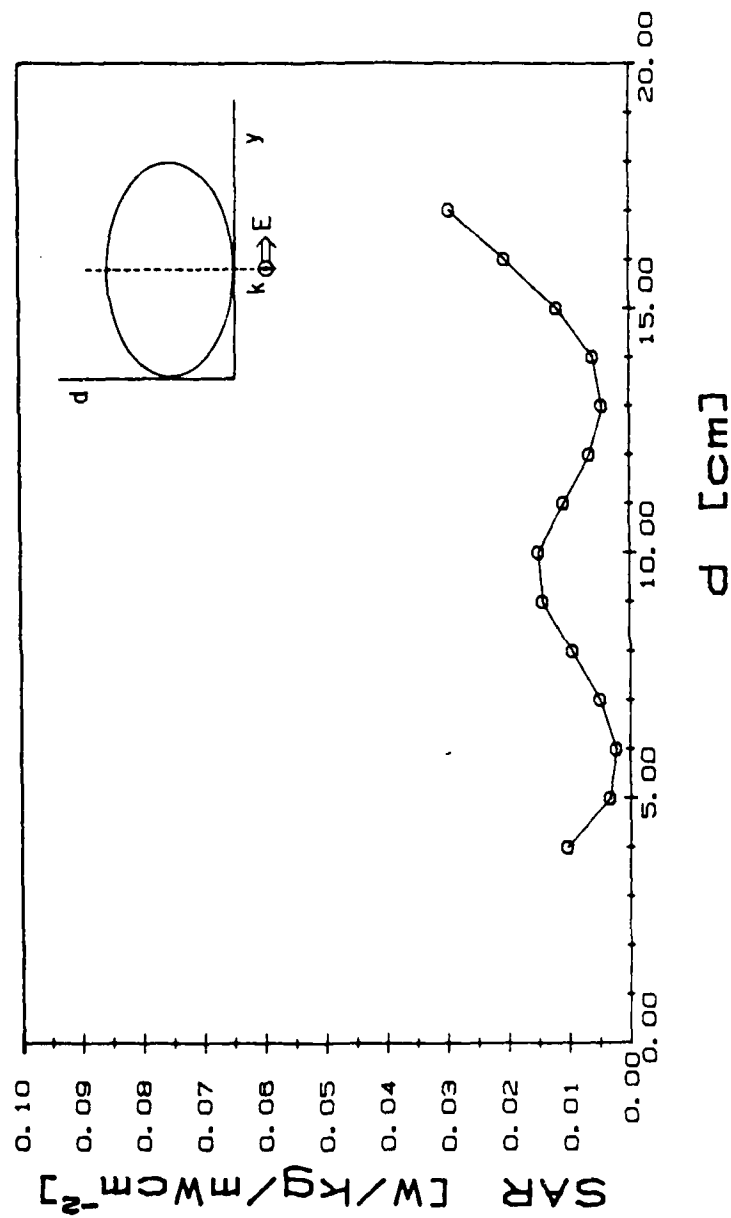


Figure 10 - Far-field experiments. The specific absorption rate (SAR) (normalized to  $1 \text{ mW/cm}^2$ ) in the torso vs. the distance across the torso at  $x = 137 \text{ cm}$  from the base (feet), frequency  $350 \text{ MHz}$ , polarization  $k \parallel L$ .



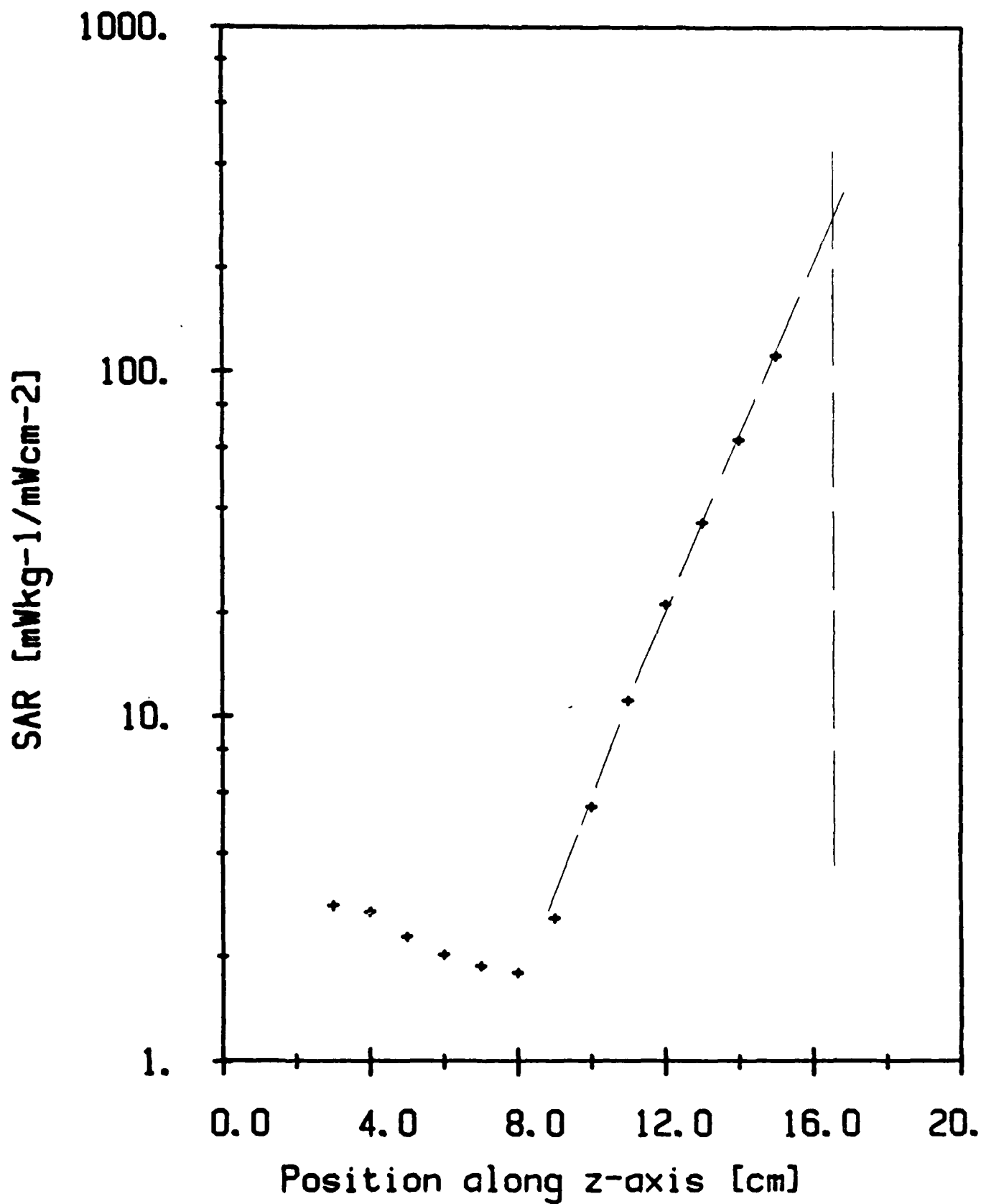


Figure 11 - Far-field experiments. The specific absorption rate (SAR) (normalized to 1 mW/cm<sup>2</sup>) - logarithmic scale) in the torso vs. the distance from the body surface at which the wave is incident. Position x = 127 cm from the base (feet), frequency 350 MHz, E || L.

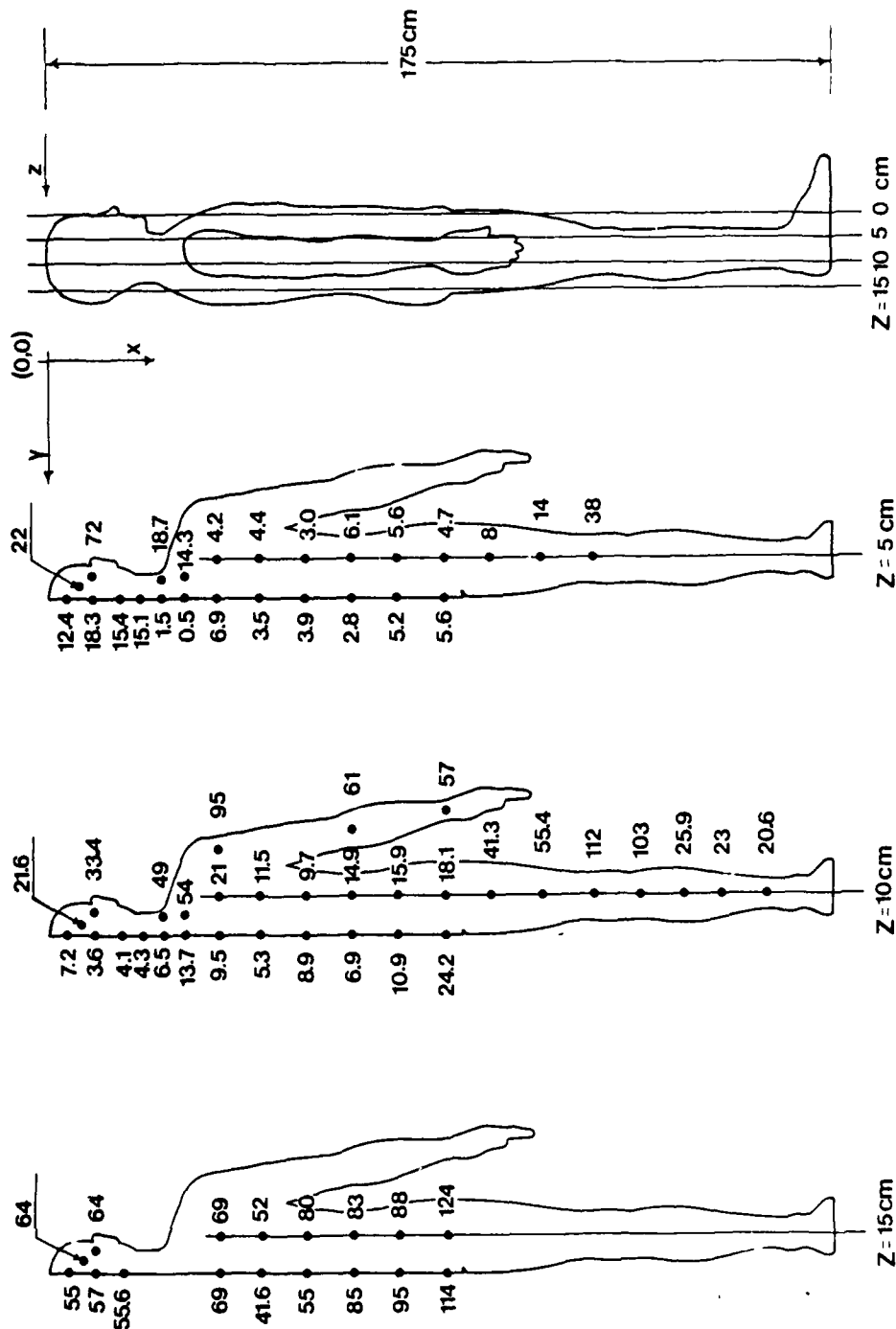


Figure 12 - Far-field experiments. The specific absorption rate (SAR) (normalized to  $1\text{ mW/cm}^2$ ) in three body cross sections, frequency 350 MHz, polarization H || L, propagation back to front.

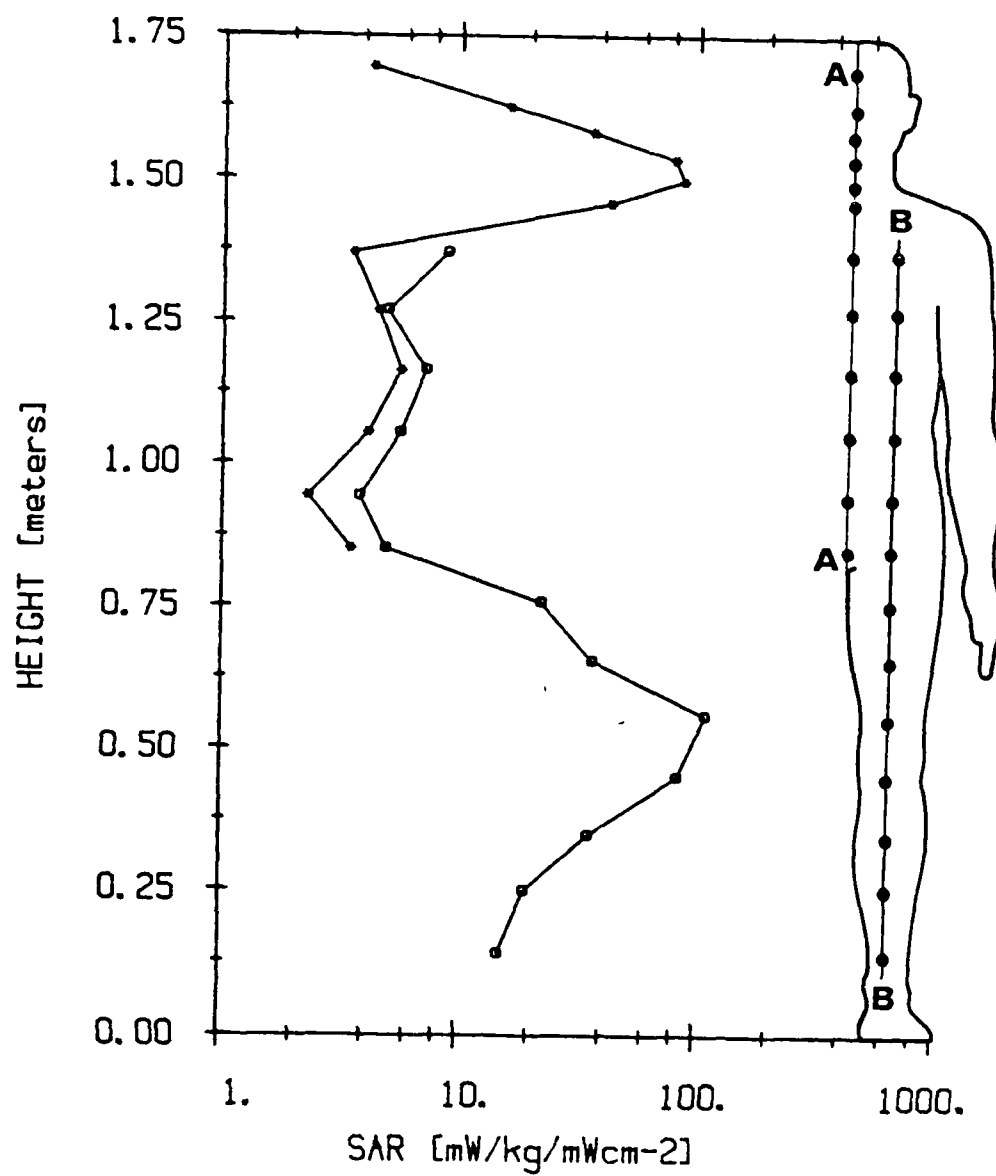


Figure 13 - Far-field experiments. The distribution of the specific absorption rate (SAR) (normalized to  $1 \text{ mW/cm}^2$ ) along the body axis, frequency 350 MHz,  
a) polarization  $E \parallel L$

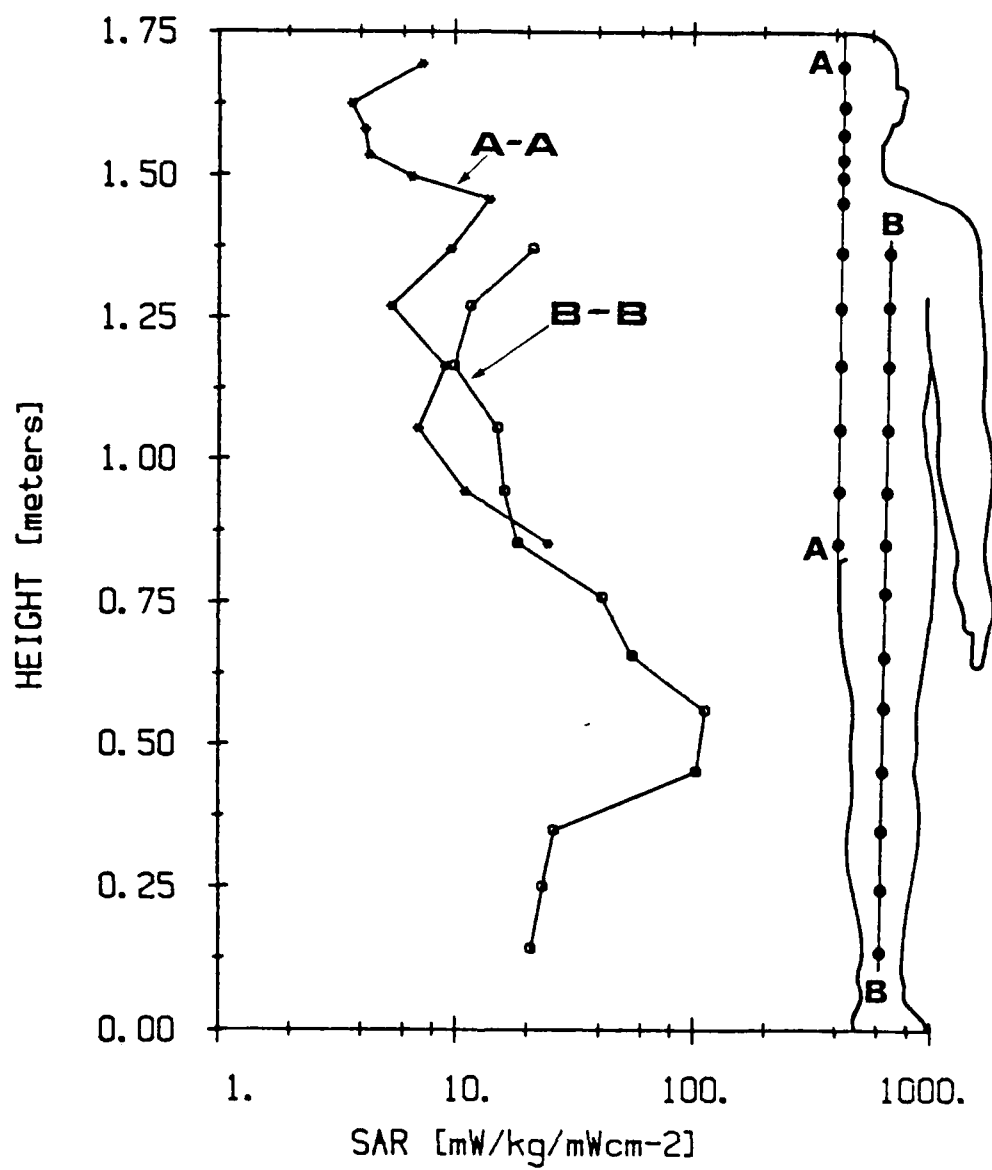


Figure 13 - Far-field experiments. The distribution of the specific absorption rate (SAR) (normalized to  $1 \text{ mW/cm}^2$ ) along the body axis, frequency 350 MHz,

b) polarization H || L.

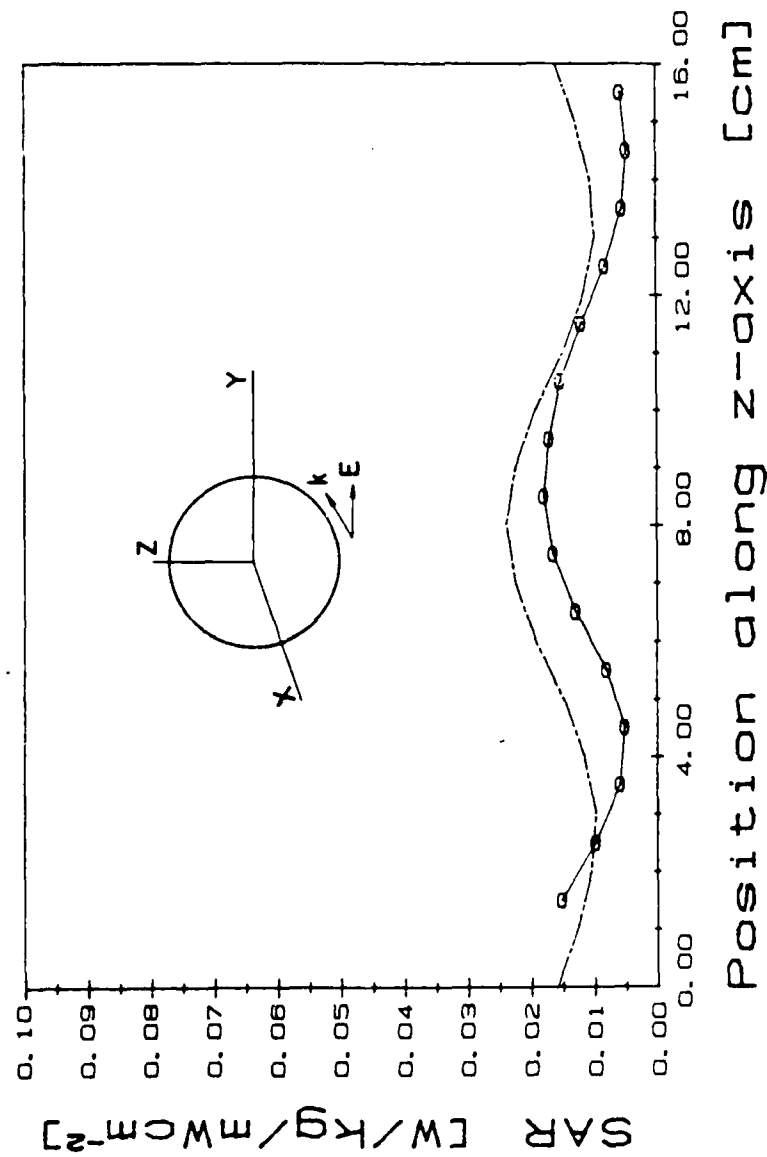


Figure 14 - Far-field experiments. The distribution of the specific absorption rate (SAR) (normalized to 1 mW/cm<sup>2</sup>) in the head-solid line with experimental points, frequency 350 MHz, polarization k || L. Dashed line represents the SAR distribution in a 16-cm dia. lossy sphere calculated numerically and presented here for comparison.

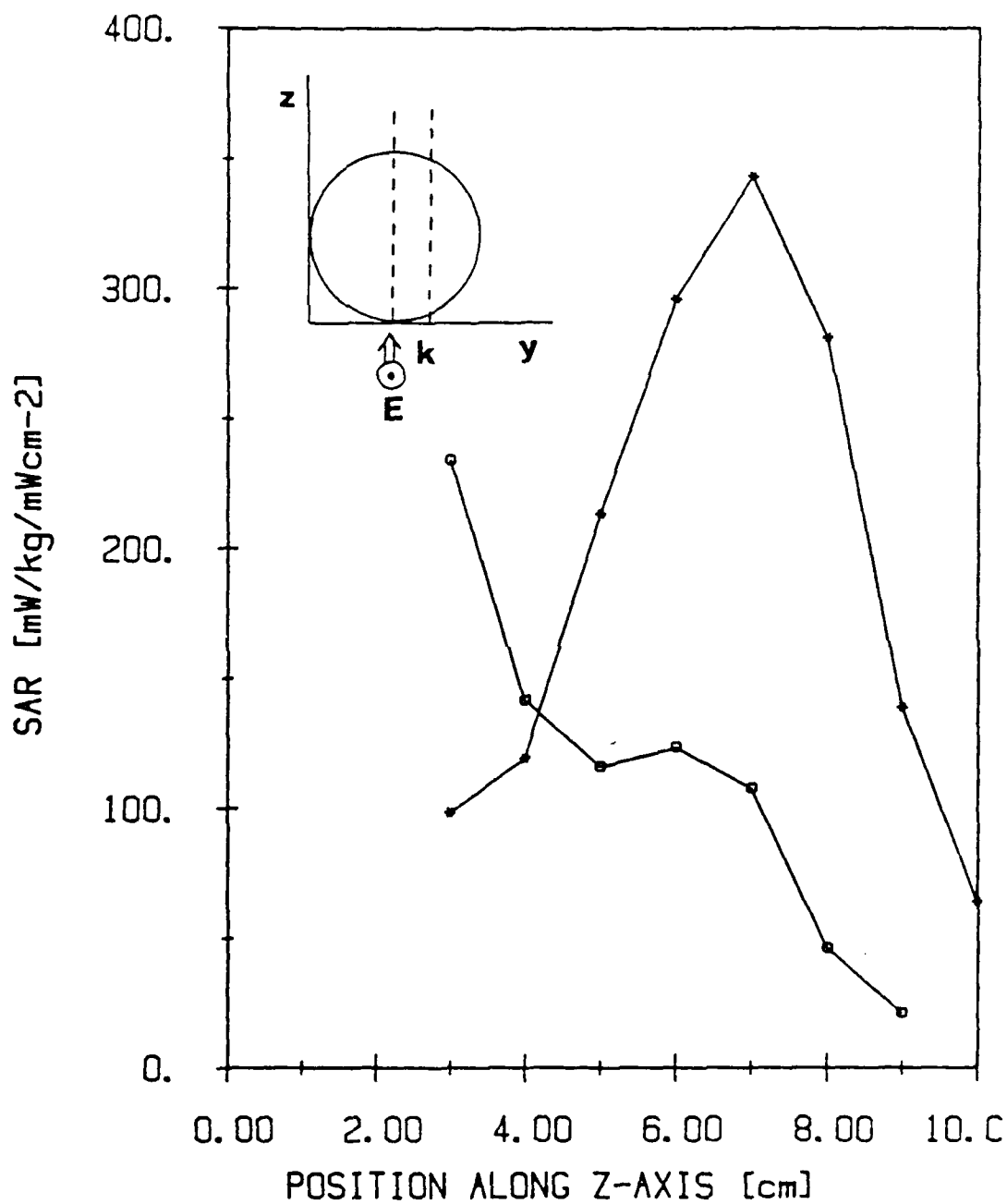


Figure 15 - Far-field experiments. The distribution of the specific absorption rate (SAR) (normalized to  $1 \text{ mW/cm}^2$ ) in the neck - at  $x = 150 \text{ cm}$  from the base (feet), \* on the main axis, □ 5 cm of the main axis, frequency 350 MHz, polarization E || L.

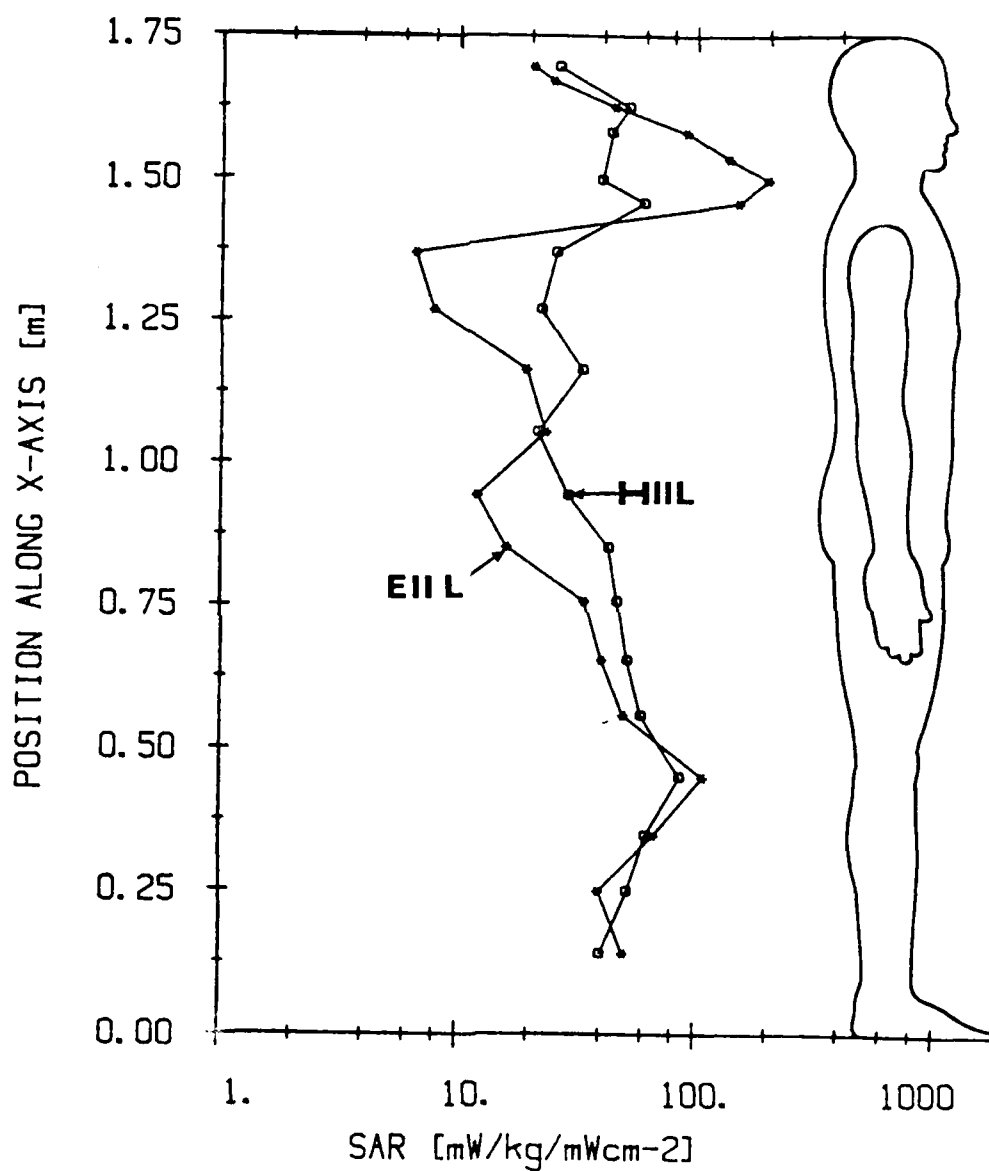


Figure 16 - Far-field experiments. The distribution of the specific absorption rate (SAR) (normalized to 1 mW/cm<sup>2</sup>) averaged over the body horizontal cross-sections (slices) for E || L and H || L, frequency 350 MHz.

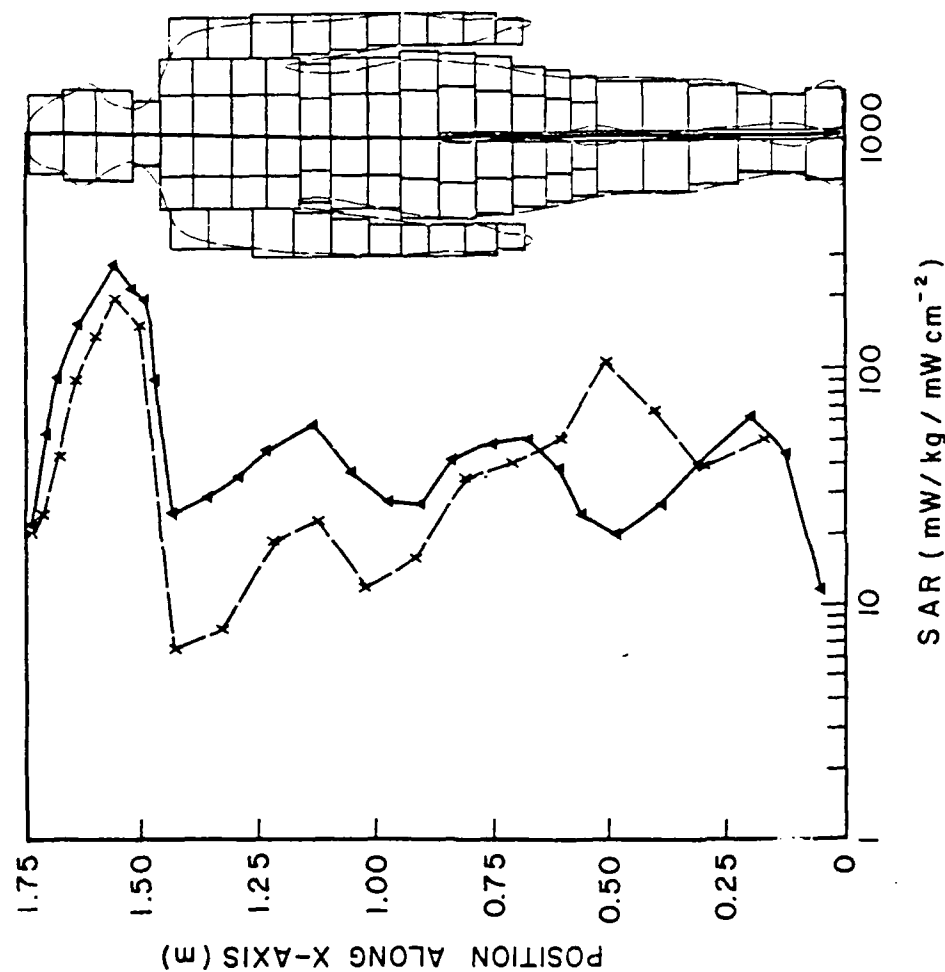


Figure 17 - Far-field experiments. Comparison of the specific absorption rate (SAR) (normalized to 1 mW/cm<sup>2</sup>) distribution averaged over the body horizontal cross-sections (slices): the data calculated for the block model (solid line) and the experimental data (this work) (dashed line), frequency 350 MHz, polarization E || L.



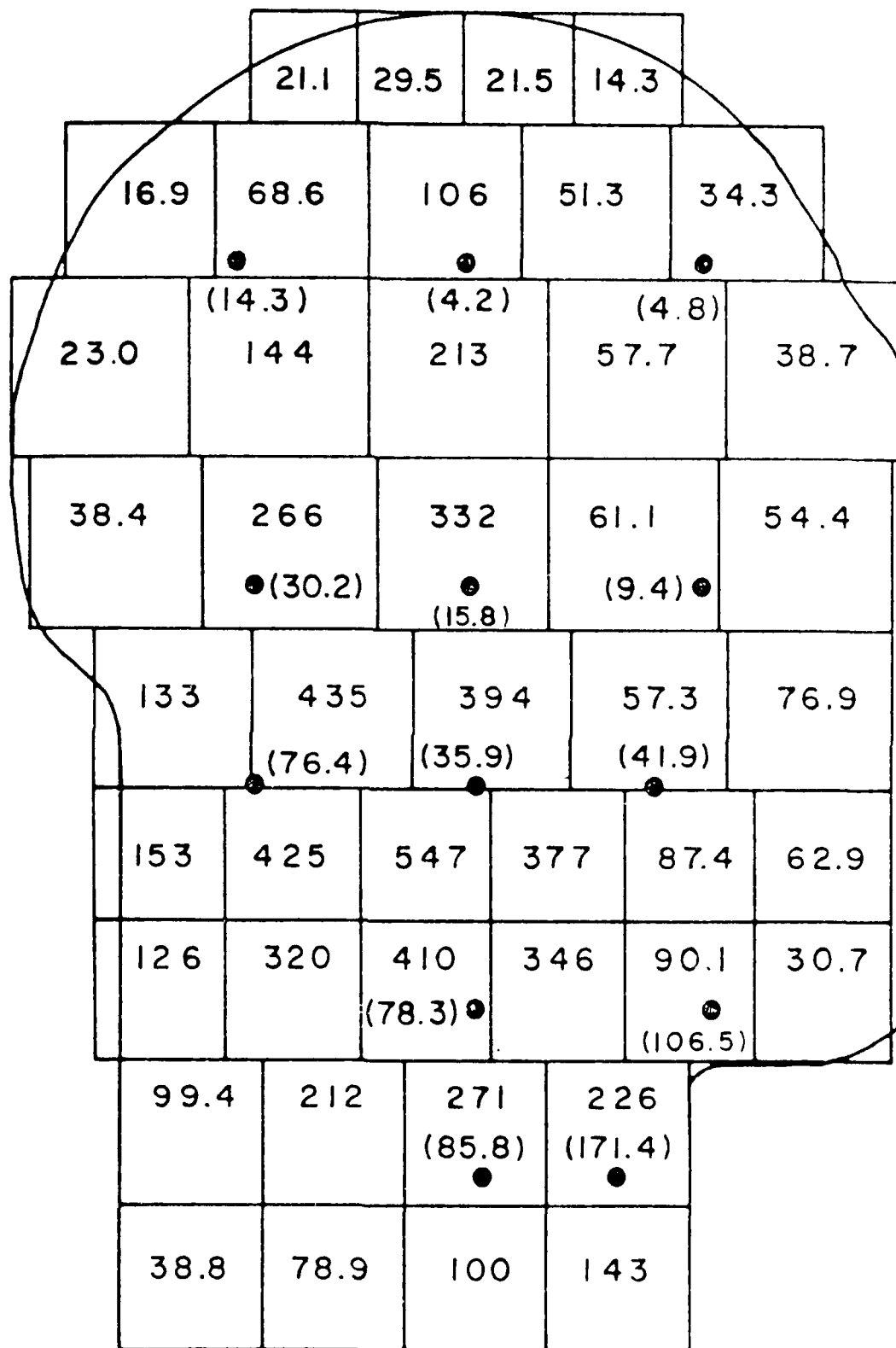


Figure 18 - Far-field experiments. Comparison of the specific absorption rate (SAR) (normalized to  $1 \text{ mW/cm}^2$ ) distribution in the head: the data calculated for the block model (number in blocks) and the experimental data (this work) (numbers in brackets), frequency 350 MHz, polarization E || L  
a) inner layer; polarization E || L

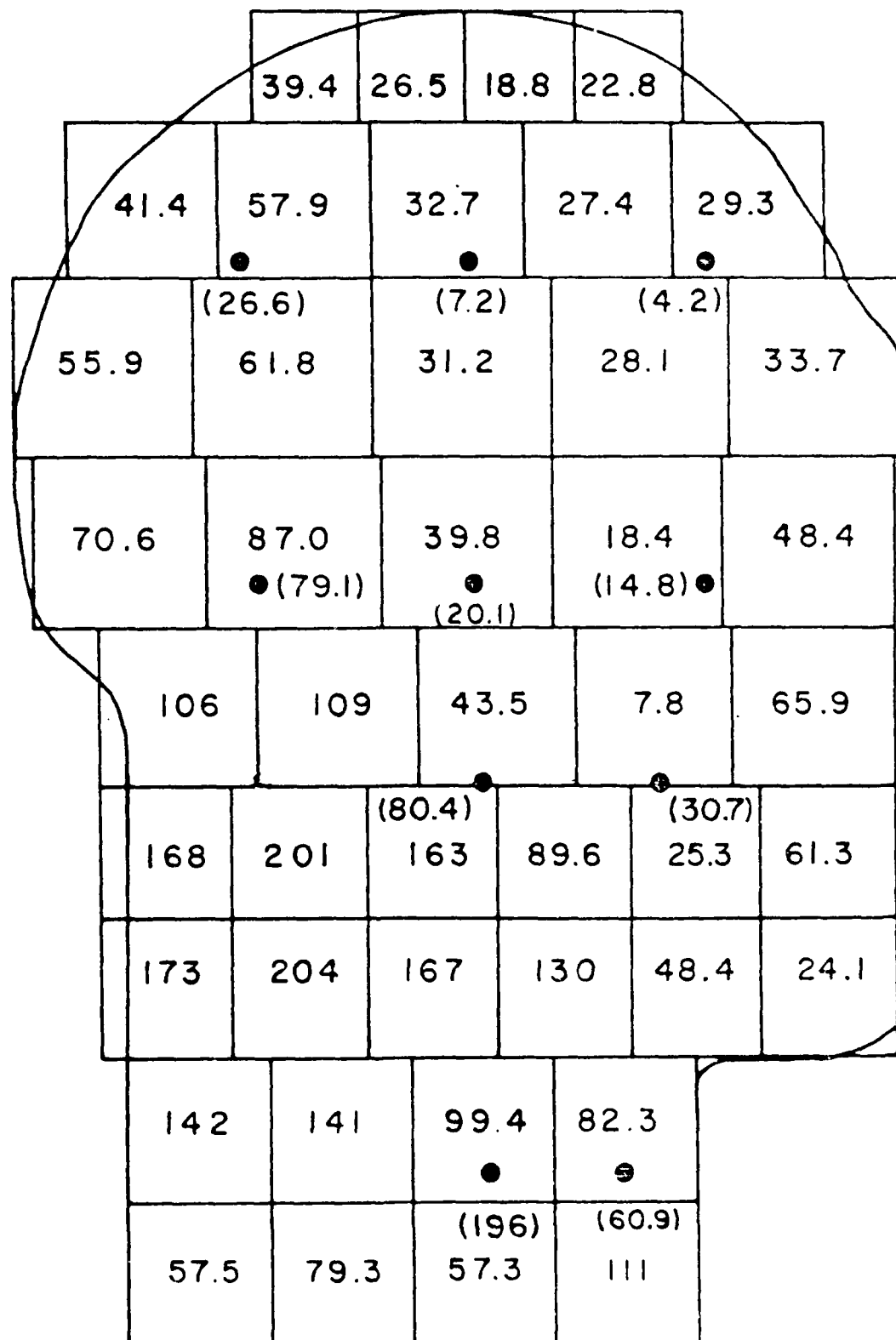
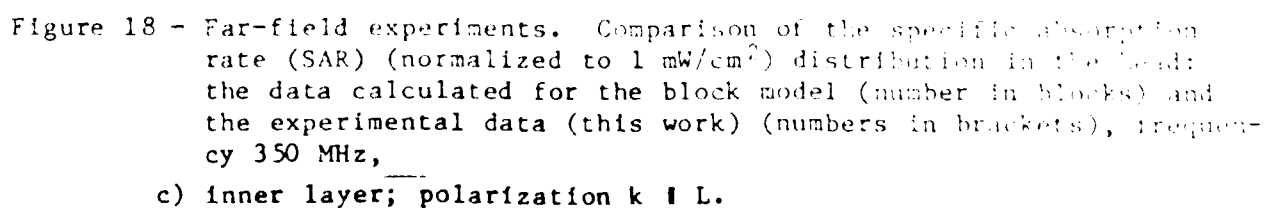


Figure 8 - Far-field experiments. Comparison of the specific absorption rate (SAR) (normalized to 1 mW/cm<sup>2</sup>) distribution in the head: the data calculated for the block model (number in blocks) and the experimental data (this work) (numbers in brackets), frequency 350 MHz, polarization E || L

b) outer layer; polarization E ⊥ L



c) inner layer; polarization  $k \parallel L$ .

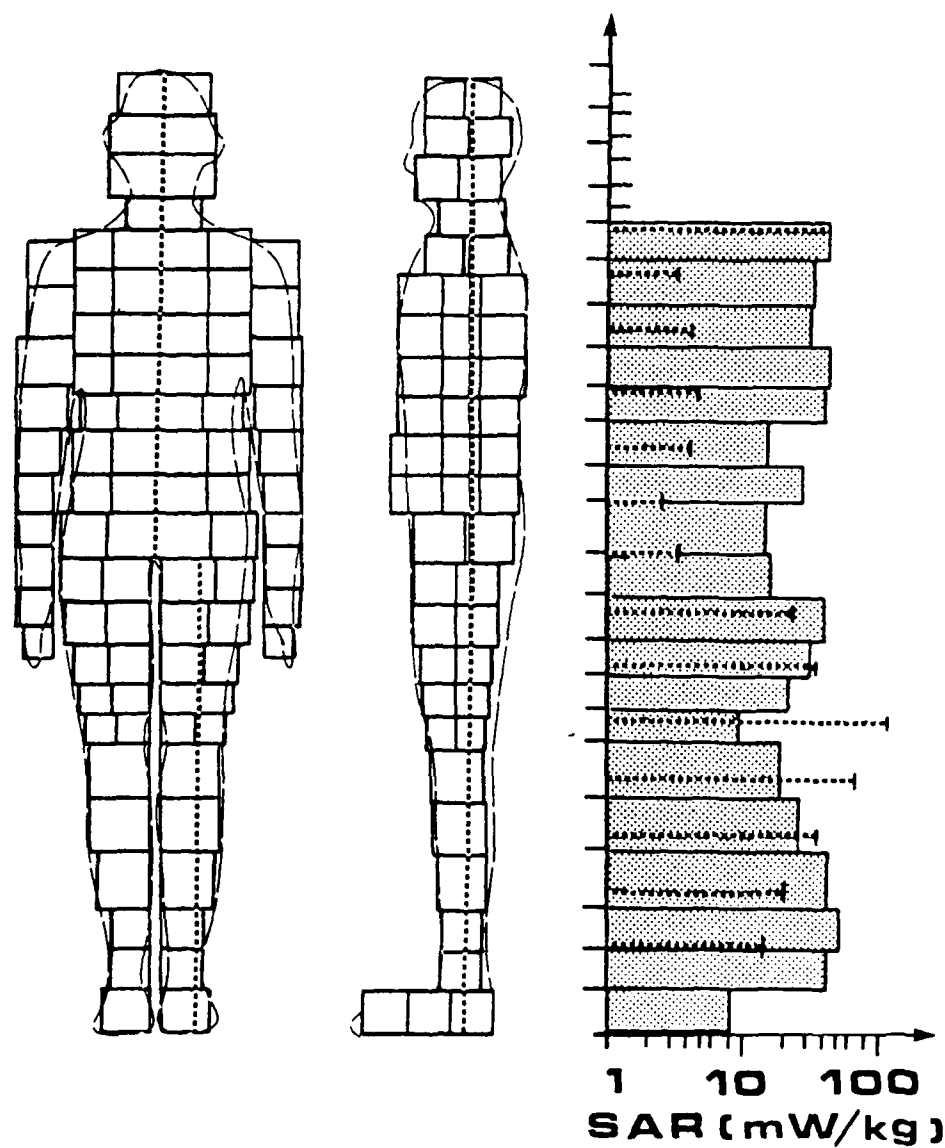


Figure 19 - Far field experiments. Comparison of the specific absorption rate (SAR) (normalized to  $1 \text{ mW/cm}^2$ ) distribution in the body: the data calculated for the block model (shaded bars) and the experimental data (this work) (dashed lines), frequency 350 MHz  
a) E || L middle layer

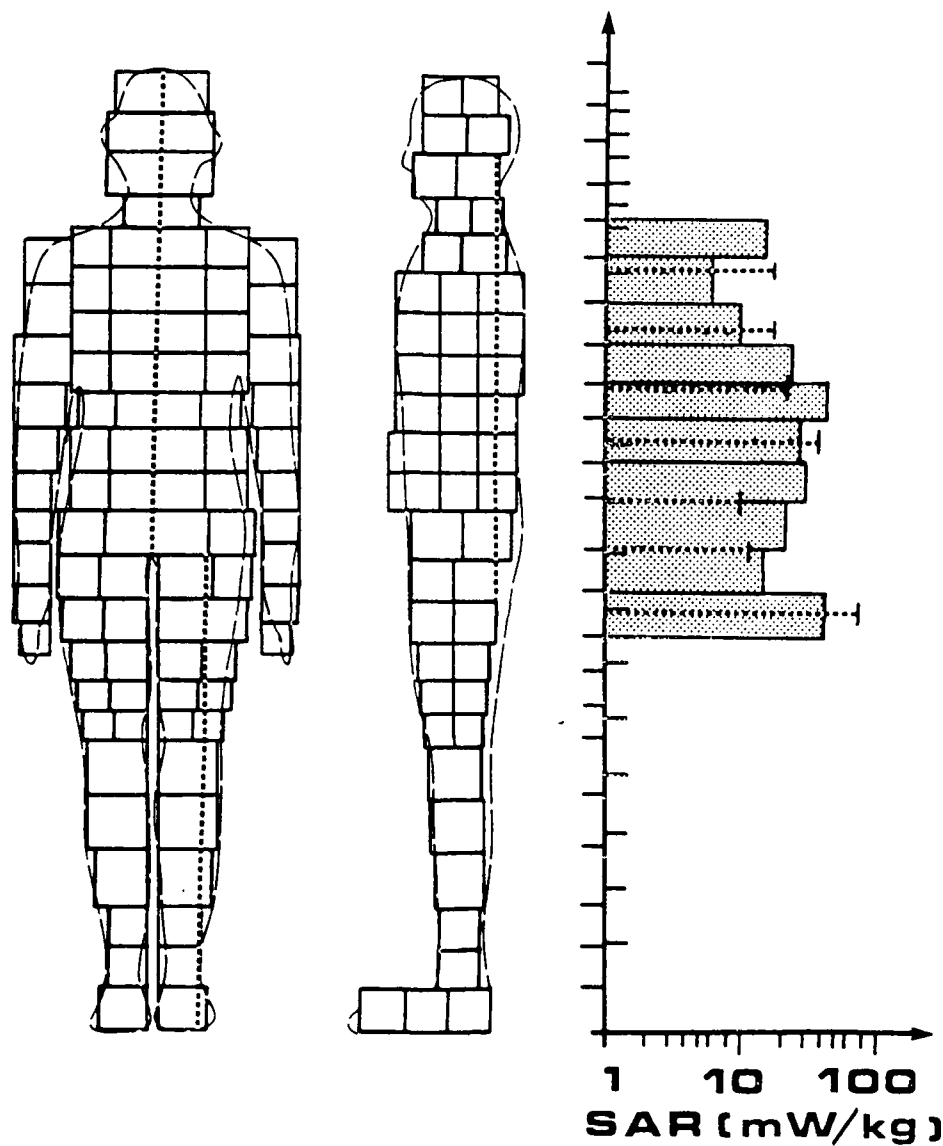


Figure 19 - Far field experiments. Comparison of the specific absorption rate (SAR) (normalized to  $1 \text{ mW/cm}^2$ ) distribution in the body: the data calculated for the block model (shaded bars) and the experimental data (this work) (dashed lines), frequency 350 MHz

b) E || L back layer

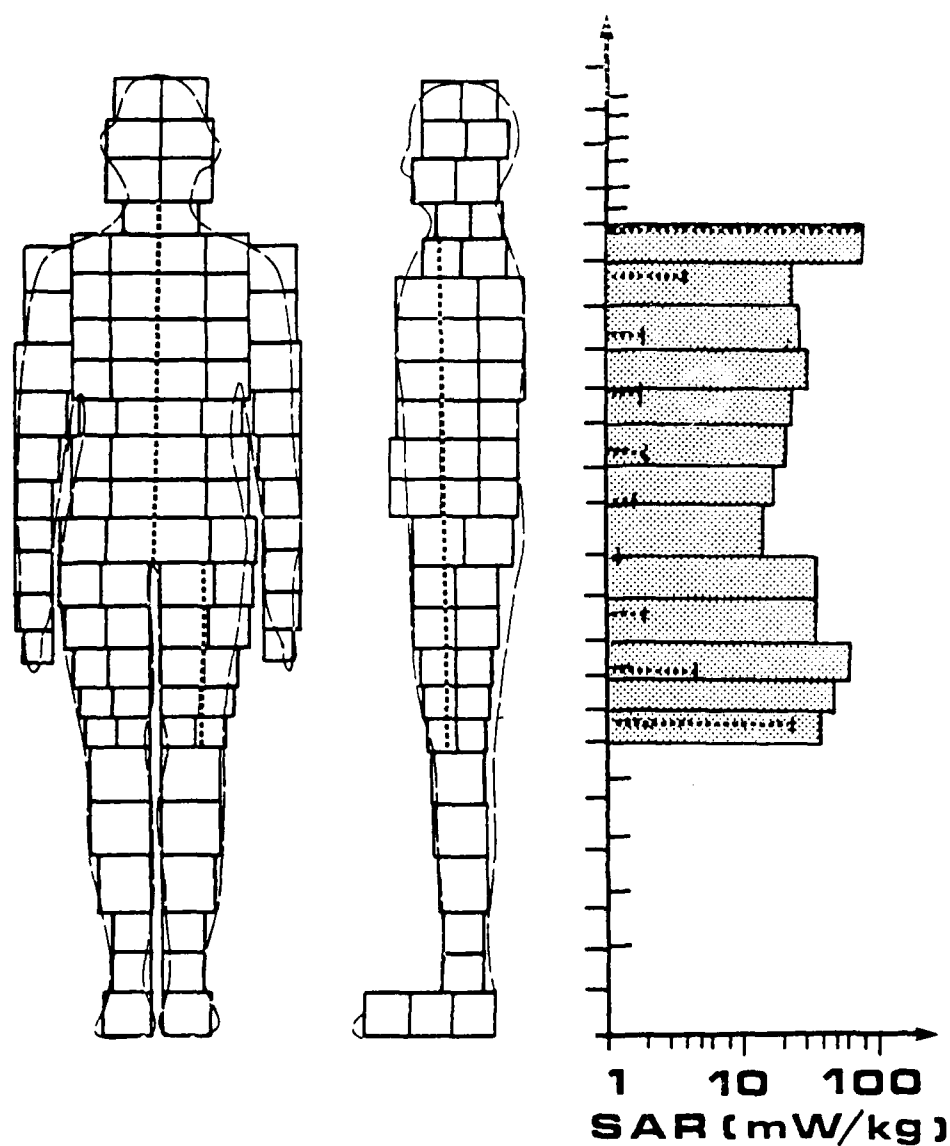


Figure 19 - Far field experiments. Comparison of the specific absorption rate (SAR) (normalized to  $1 \text{ mW/cm}^2$ ) distribution in the body: the data calculated for the block model (shaded bars) and the experimental data (this work) (dashed lines), frequency 350 MHz

c) E || L front layer

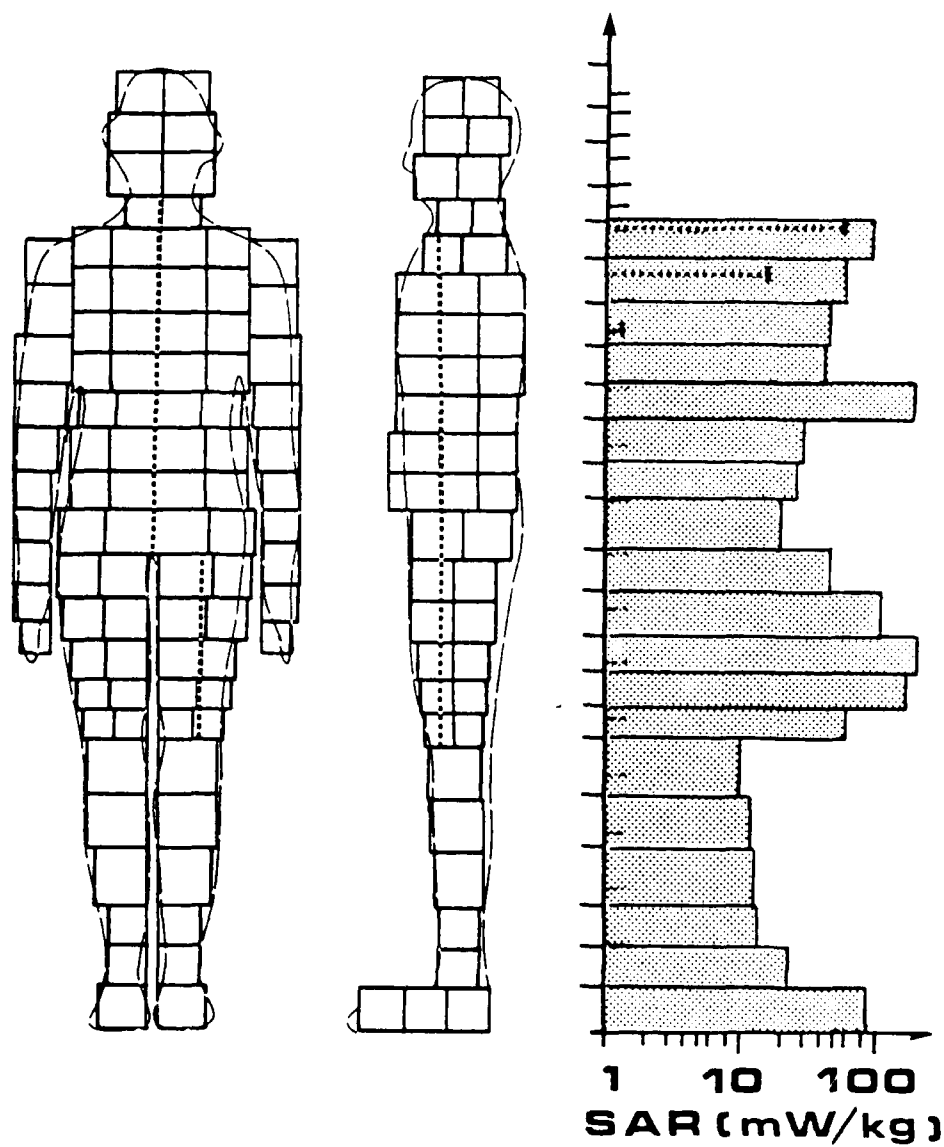


Figure 19 - Far field experiments. Comparison of the specific absorption rate (SAR) (normalized to  $1 \text{ mW/cm}^2$ ) distribution in the body: the data calculated for the block model (shaded bars) and the experimental data (this work) (dashed lines), frequency 350 MHz

d) k || L middle layer.

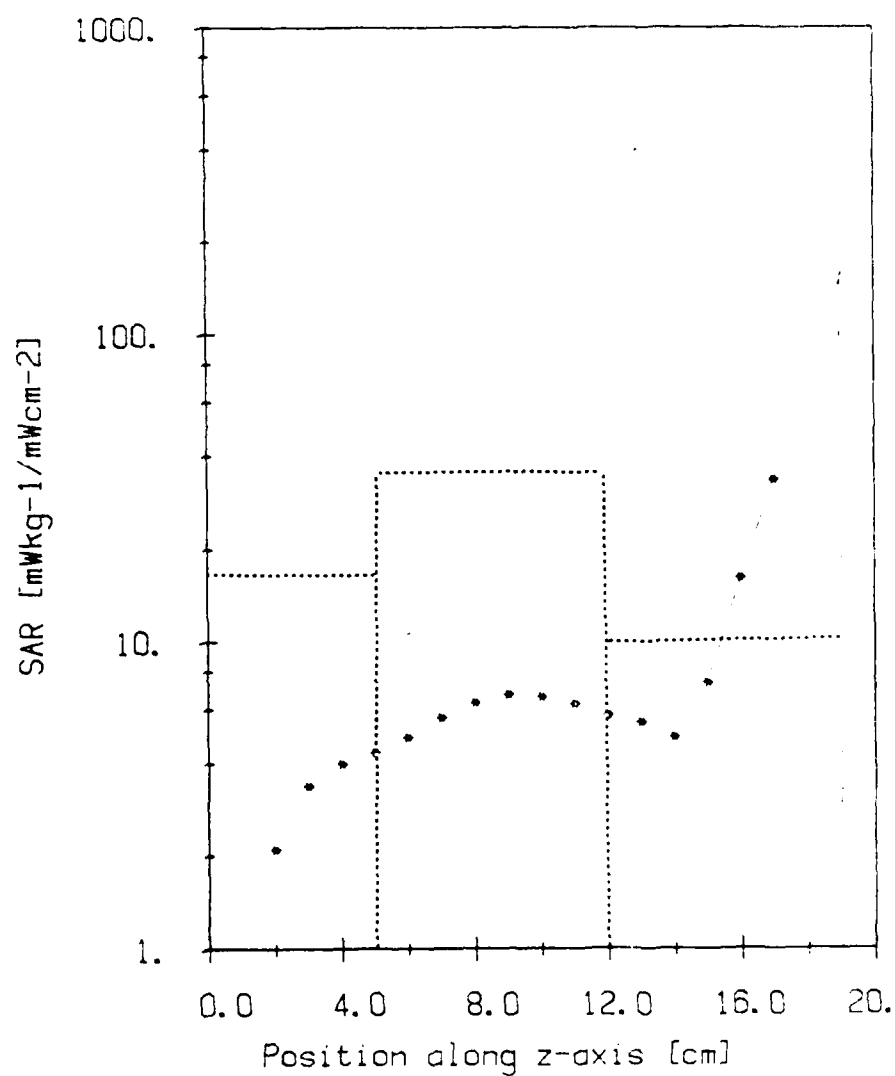


Figure 20 - Far-field experiments. Comparison of the specific absorption rate (SAR) (normalized to 1 mW/cm<sup>2</sup>) distribution in the torso along the direction of propagation: the data calculated for the block model (dashed-line blocks) and the experimental data (this work) (stars), frequency 350 MHz, polarization E<sub>z</sub>, L, a) at x = 127 cm from the base level (foot).



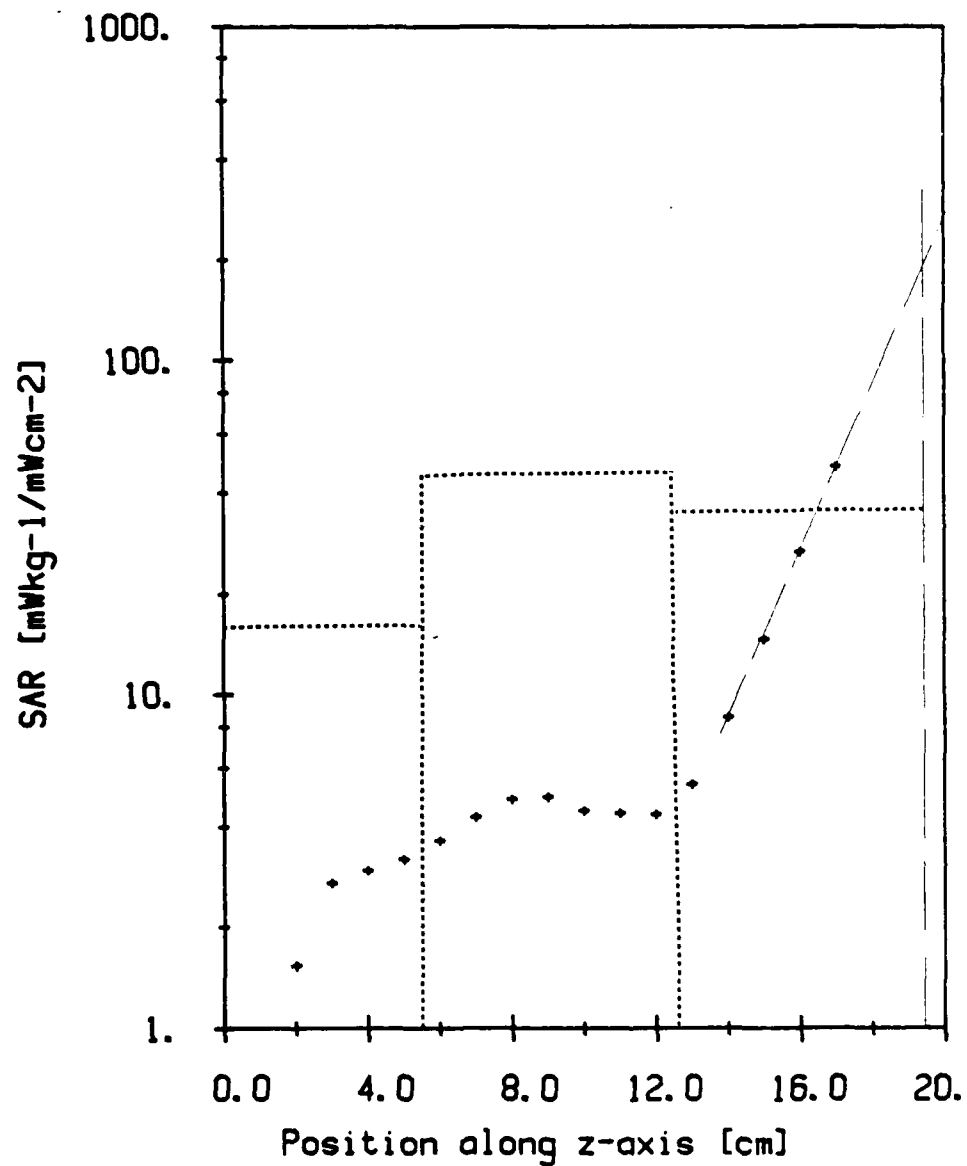


Figure 20 - Far-field experiments. Comparison of the specific absorption rate (SAR) (normalized to  $1 \text{ mW/cm}^2$ ) distribution in the torso along the direction of propagation: the data calculated for the block model (dashed-line blocks) and the experimental data (this work) (stars), frequency 350 MHz, polarization E || L,

b) at  $x = 117 \text{ cm}$   
from the base level (feet)

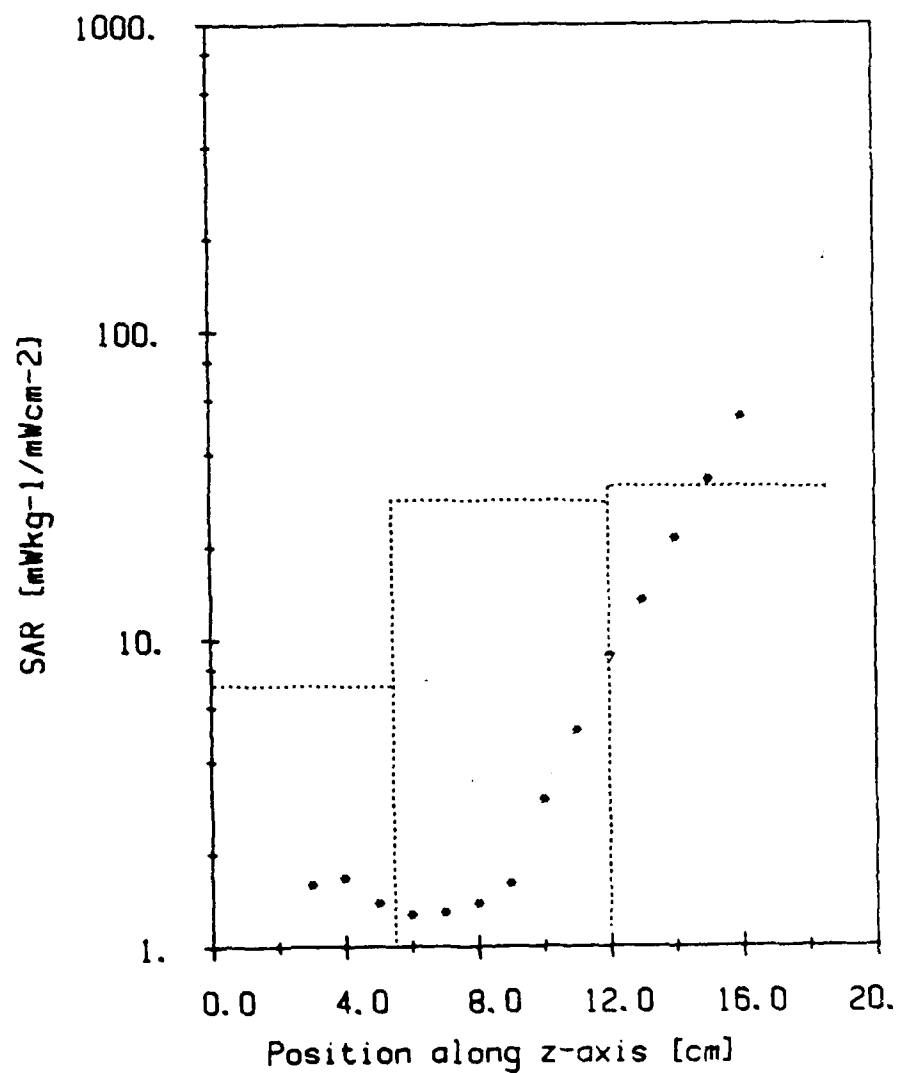


Figure 20 - Far-field experiments. Comparison of the specific absorption rate (SAR) (normalized to 1 mW/cm<sup>2</sup>) distribution in the torso along the direction of propagation: the data calculated for the block model (dashed-line blocks) and the experimental data (this work) (stars), frequency 350 MHz, polarization E // L,

c) at x = 96 cm  
from the base level (feet).

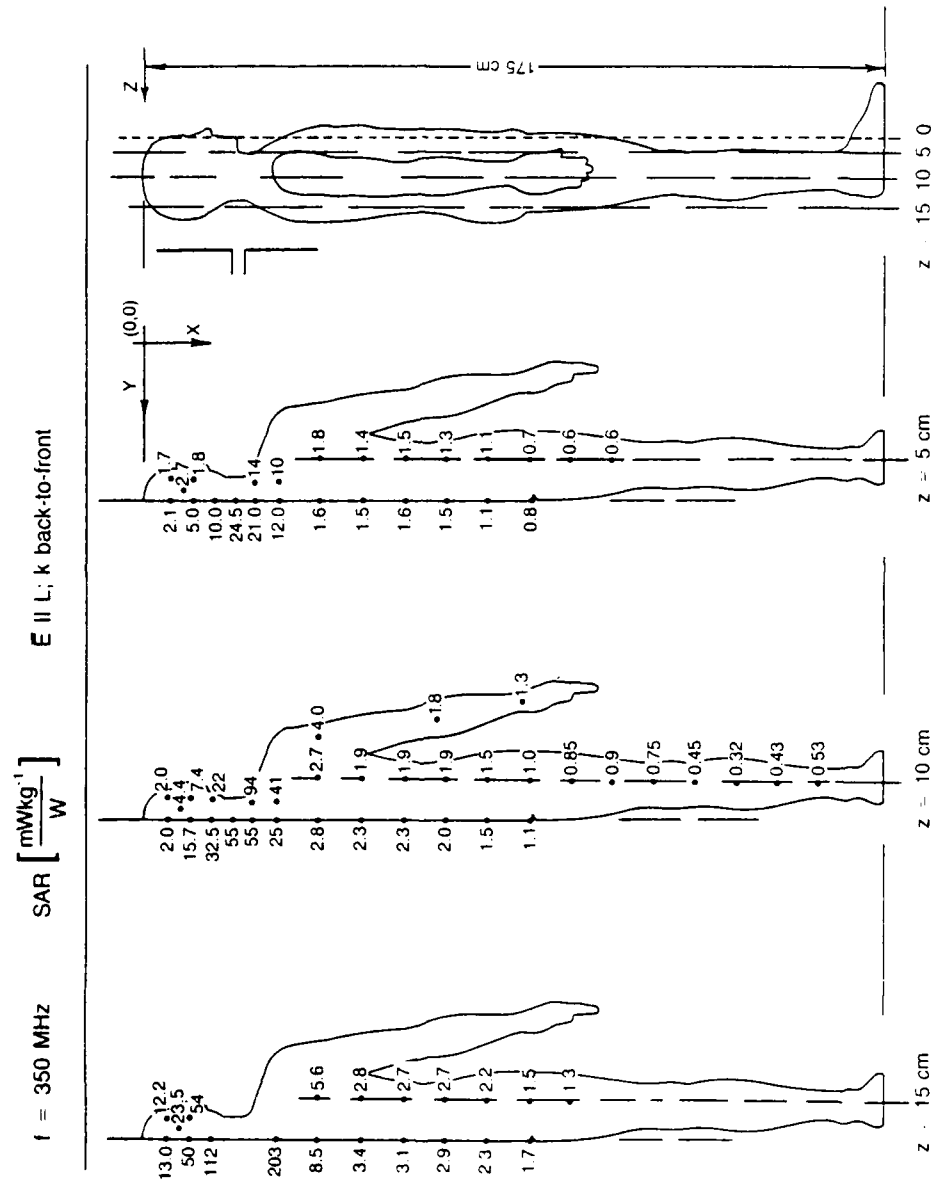


Figure 21 - Near-field experiments, resonant dipole. The distribution of the specific absorption rate (SAR) in three cross-sections of the body, frequency 350 MHz, polarization  $E \parallel L$ , power to the antenna 1W.

a) dipole at  $x = 156.5 \text{ cm}$

from the base (feet)

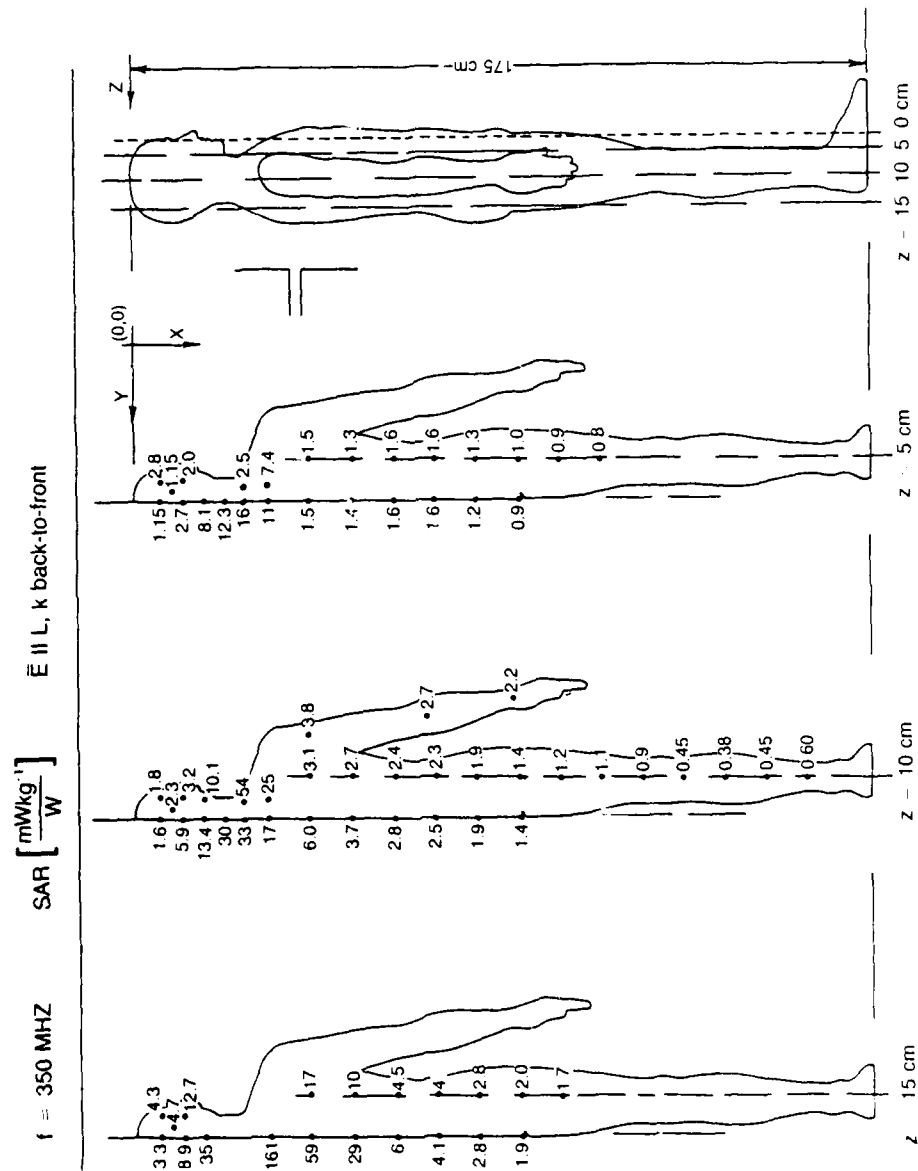


Figure 21 - Near-field experiments, resonant dipole. The distribution of the specific absorption rate (SAR) in three cross-sections of the body, frequency 350 MHz, polarization  $E \parallel L$ , power to the antenna 1W.

b) dipole at  $x = 137 \text{ cm}$

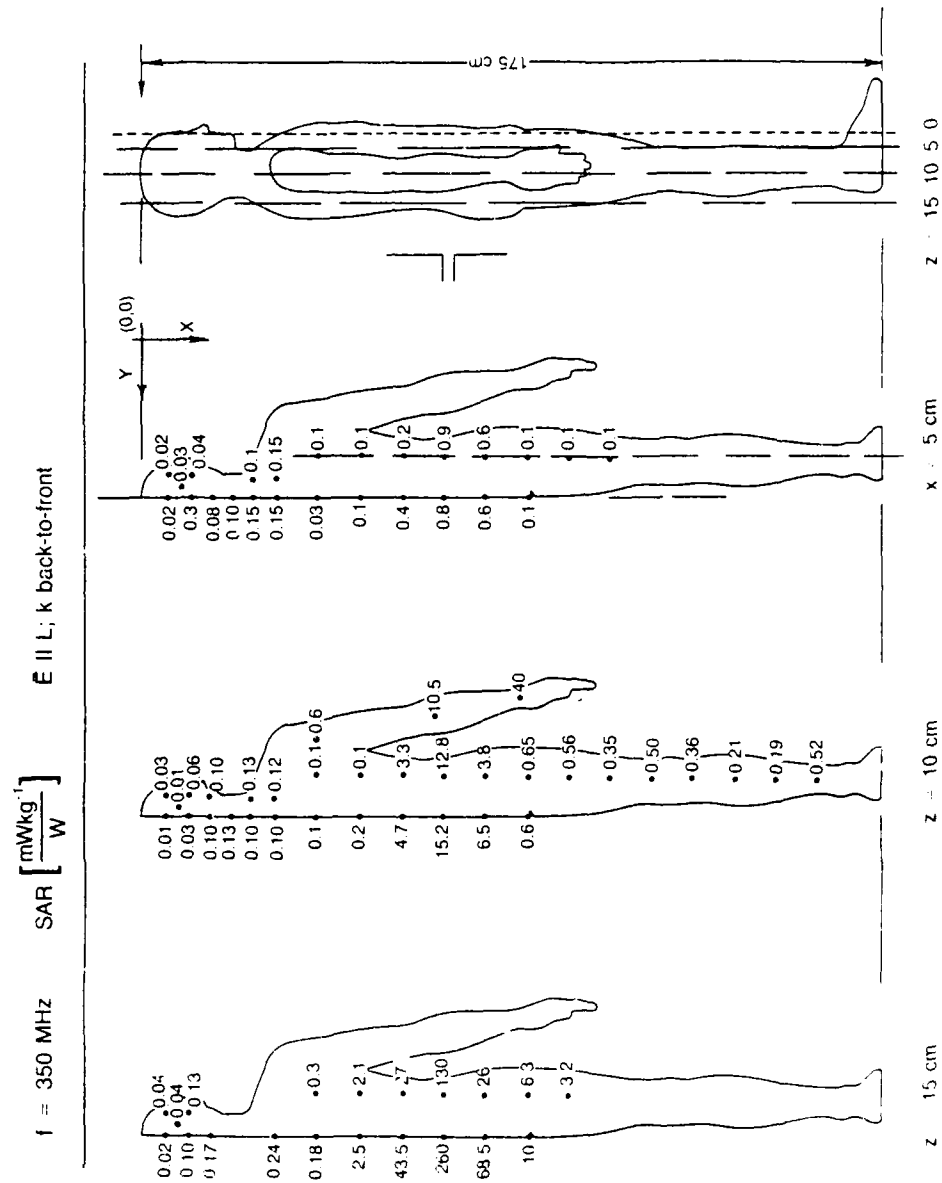


Figure 21 - Near-field experiments, resonant dipole. The distribution of the specific absorption rate (SAR) in three cross-sections of the body, frequency 350 MHz, polarization  $E \parallel L$ , power to the antenna 1W.

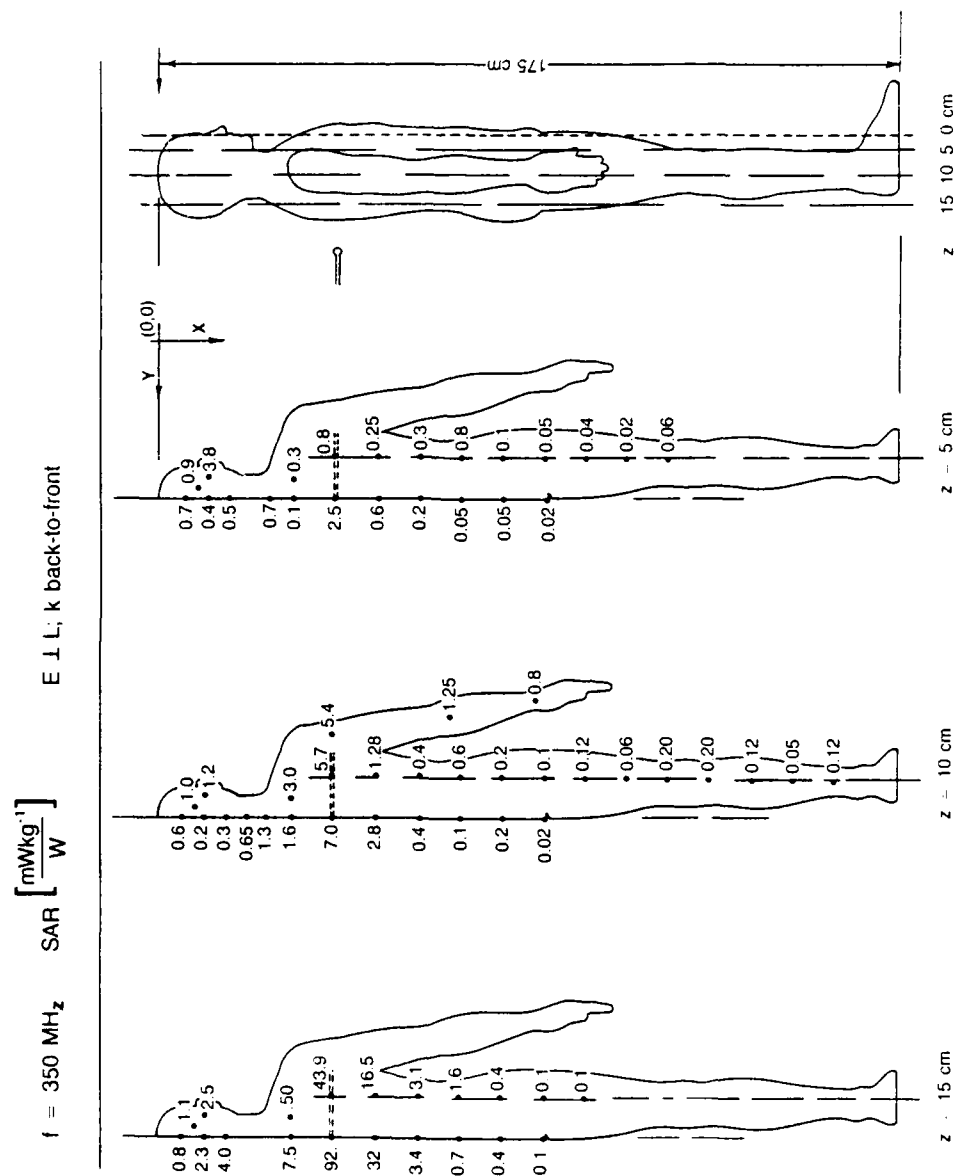


Figure 22 - Near-field experiments, resonant dipole. The distribution of the specific absorption rate (SAR) in three cross-sections of the body, frequency 350 MHz, polarization H  $\parallel$  L, power to the antenna 1 W, dipole at  $x = 137 \text{ cm}$  from the base (feet).

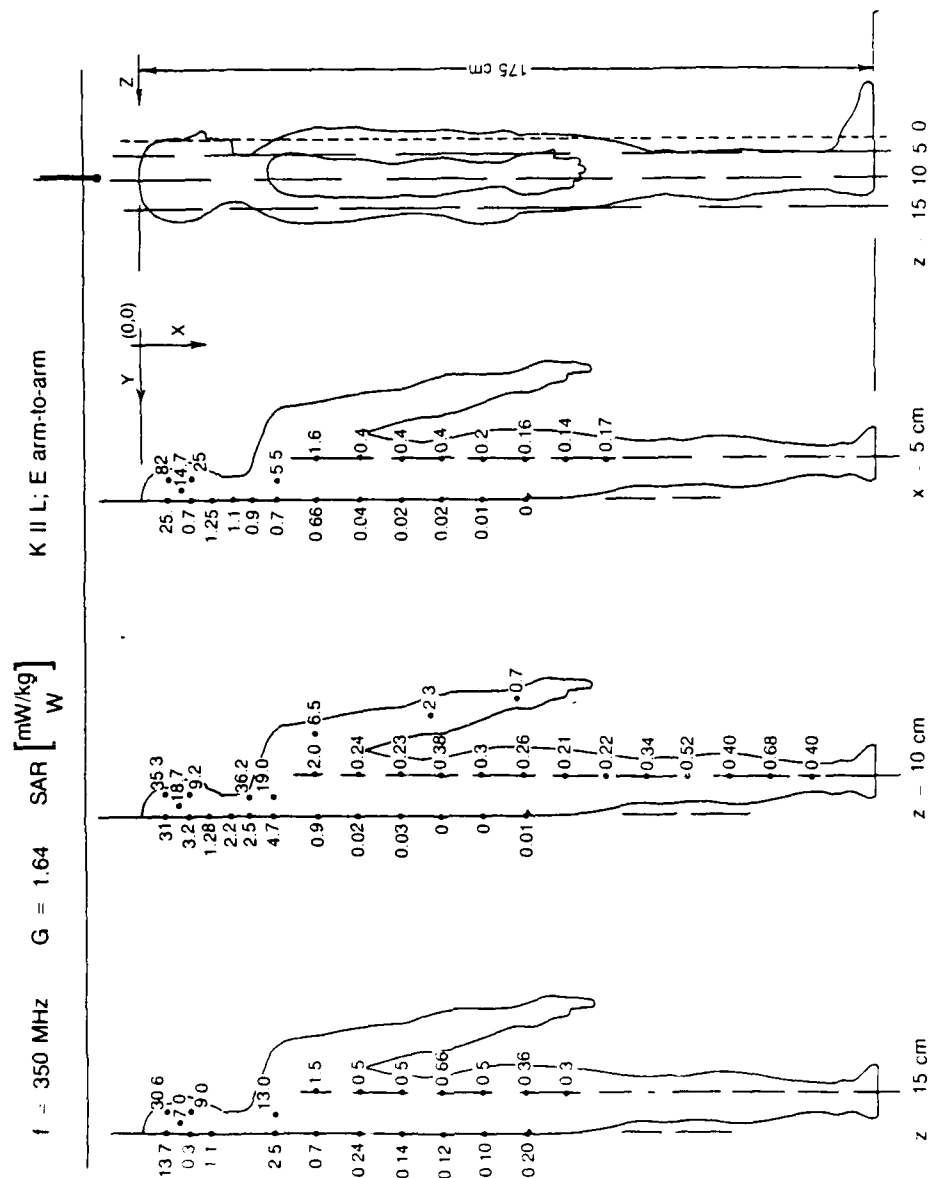


Figure 23 - Near-field experiments, resonant dipole. The distribution of the specific absorption rate (SAR) in three cross-sections of the body, frequency 350 MHz, polarization  $k \parallel L$ , dipole 14 cm above the head.

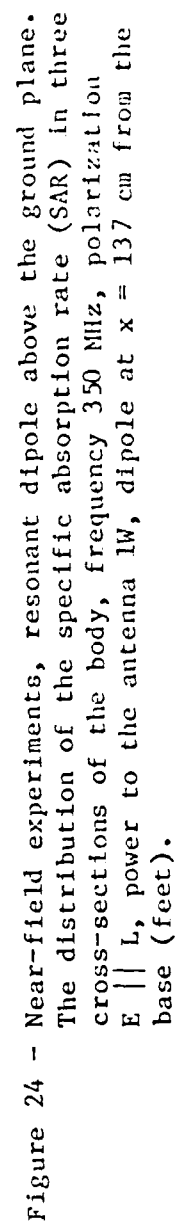


Figure 24 - Near-field experiments, resonant dipole above the ground plane. The distribution of the specific absorption rate (SAR) in three cross-sections of the body, frequency 350 MHz, polarization E || L, power to the antenna 1W, dipole at x = 137 cm from the base (feet).



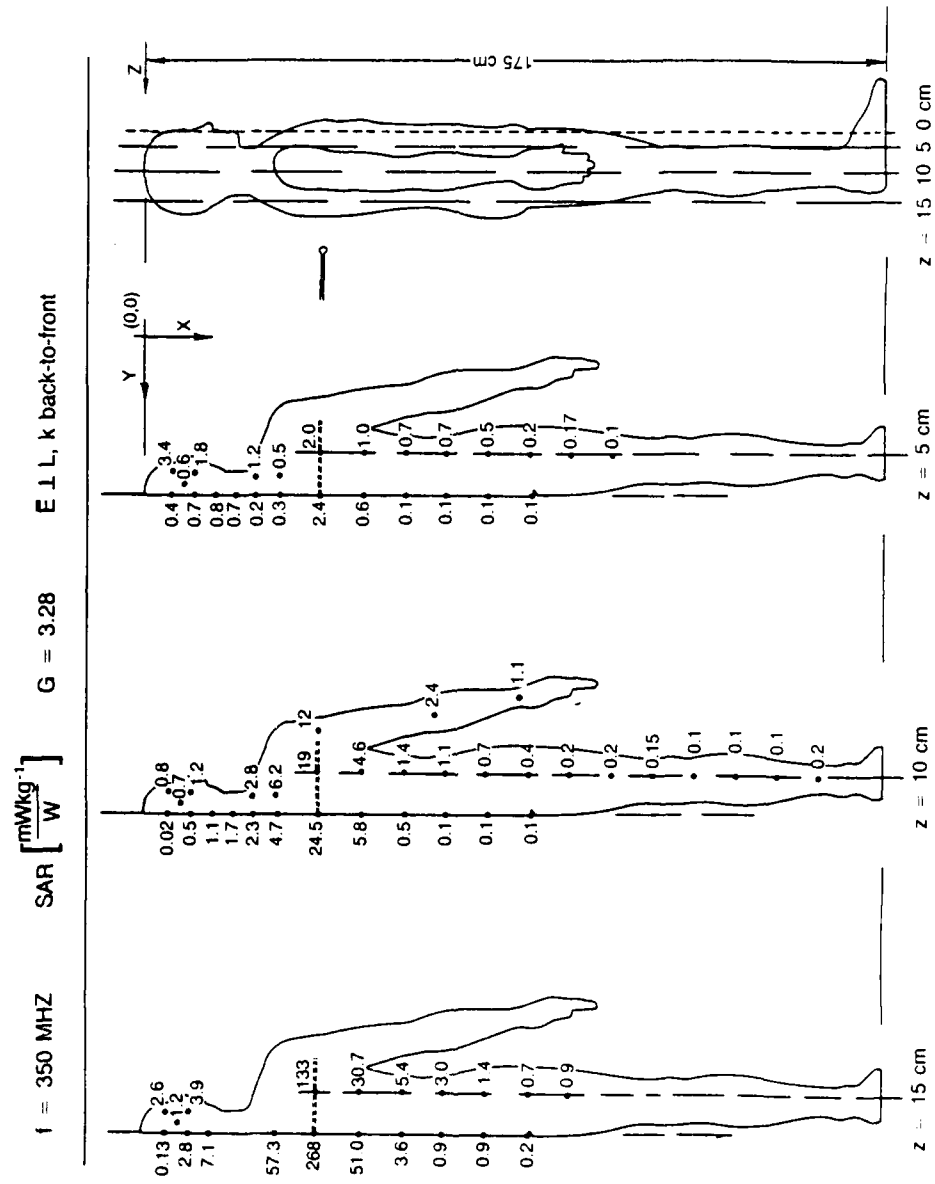


Figure 25 - Near-field experiments, resonant dipole above the ground plane.  
 The distribution of the specific absorption rate (SAR) in three cross-sections of the body, frequency 350 MHz, polarization  $H \parallel L$ , power to the antenna 1 W, dipole at  $x = 137 \text{ cm}$  from the base (feet).

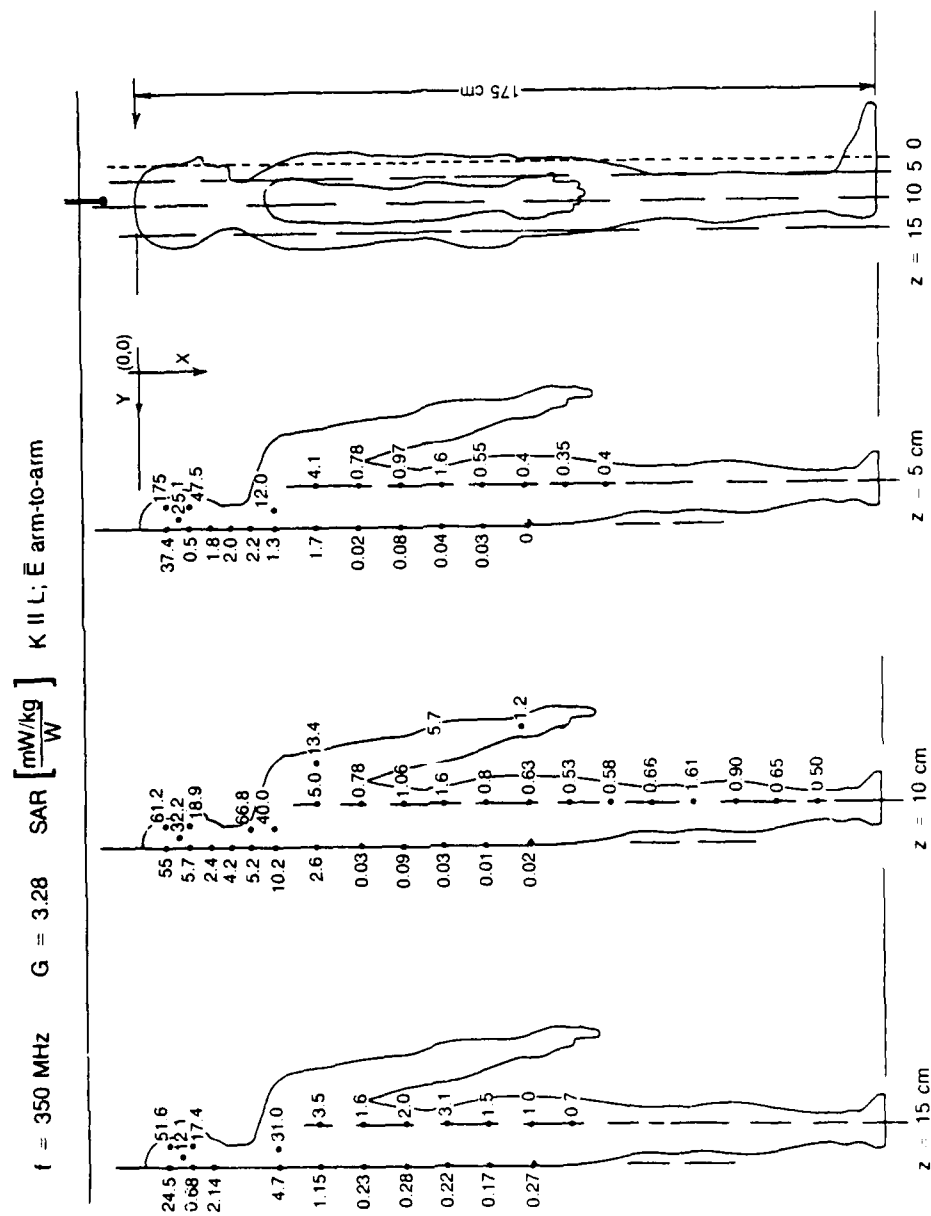


Figure 26 - Near-field experiments, resonant dipole above the ground plane.  
 The distribution of the specific absorption rate (SAR) in three  
 cross-sections of the body, frequency 350 MHz, polarization  
 $k \parallel L$ , power to the antenna 1W, dipole at  $x = 14 \text{ cm}$  above the  
 head.

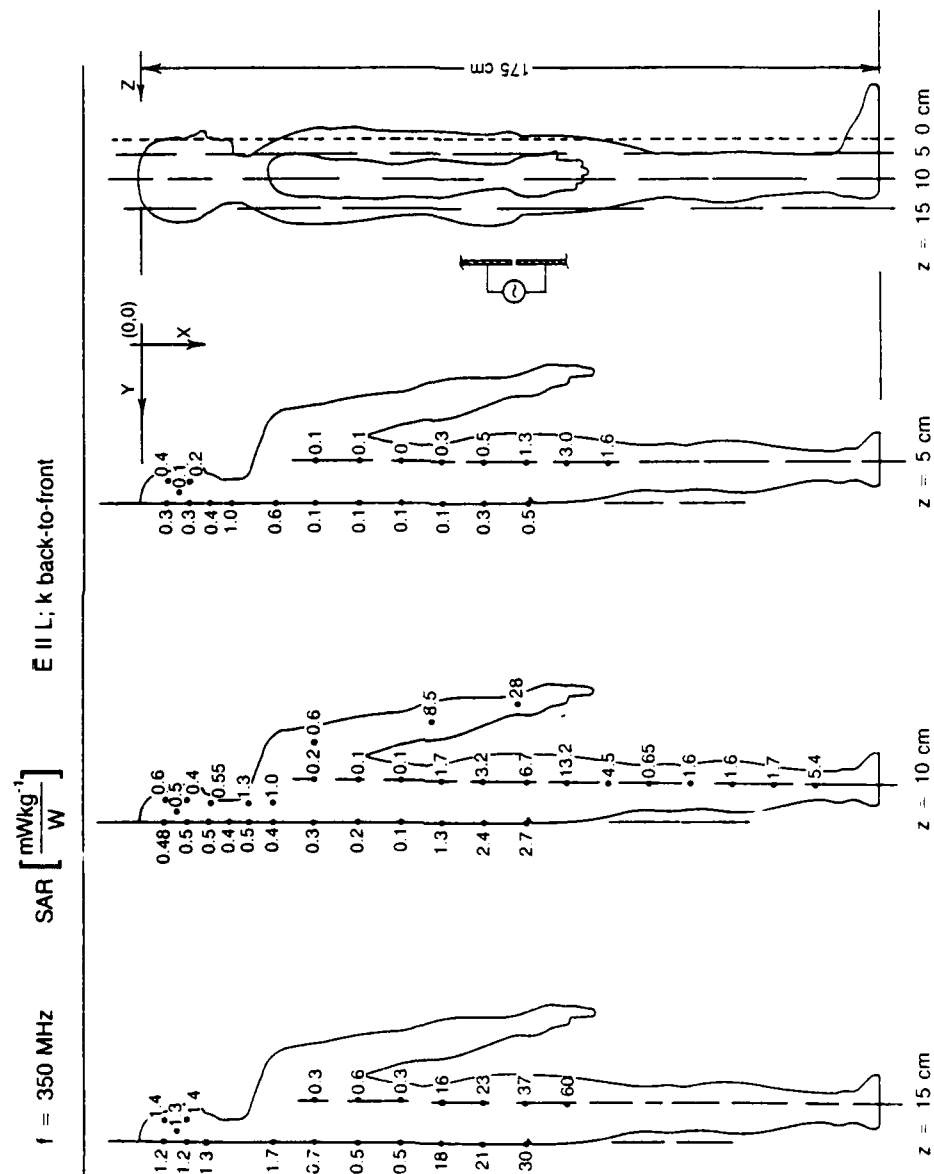


Figure 27 - Near-field experiments, resonant slot. The distribution of the specific absorption rate (SAR) in three cross-sections of the body, frequency 350 MHz, polarization  $E \parallel L$ , power to the antenna 1W, slot at  $x = 85 \text{ cm}$  from the base (feet).

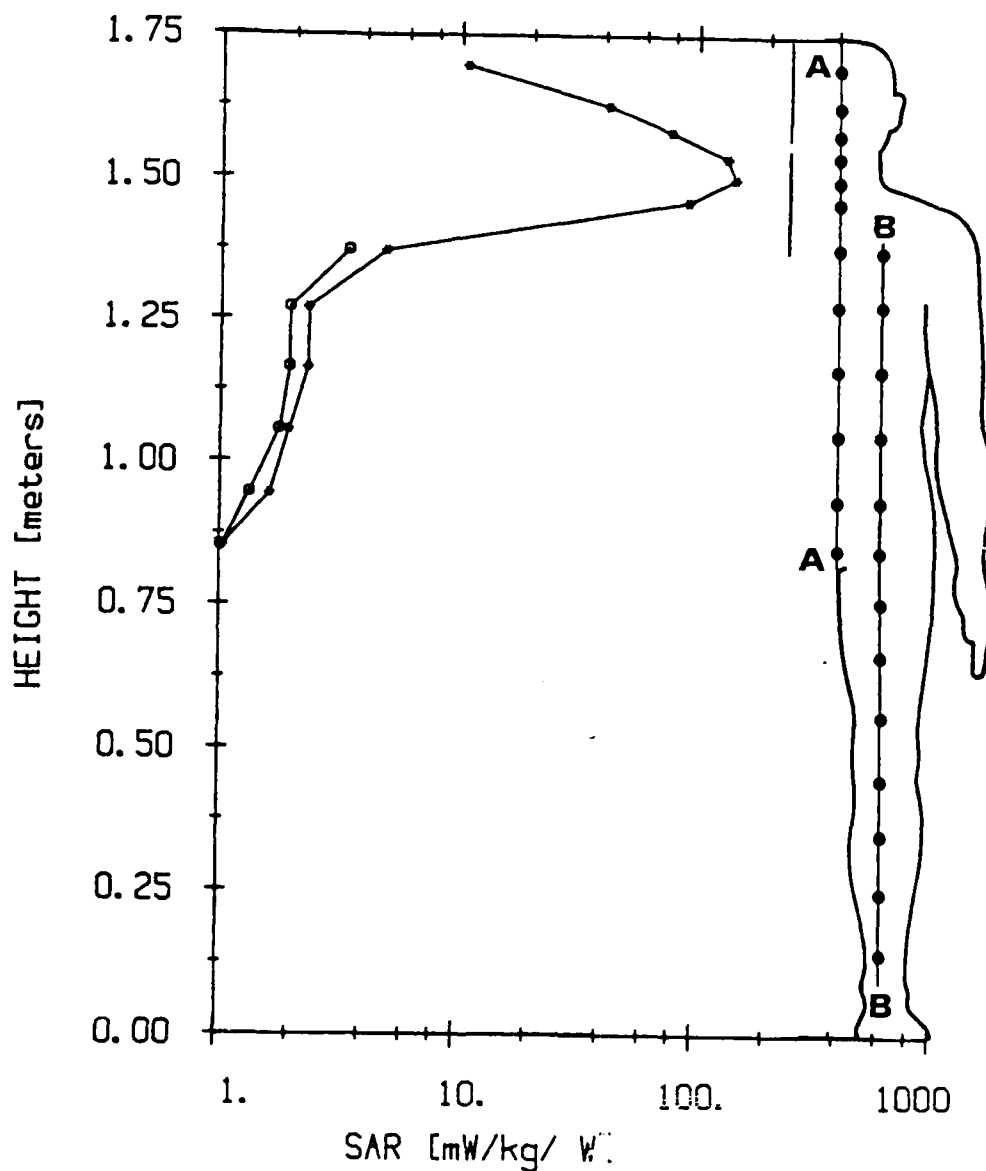


Figure 28 - Near-field experiments, resonant dipole. The mean values of the specific absorption rate (SAR) in a number of locations along the selected axis, frequency 350 MHz, polarization E || L, power to the antenna 1W,  
a) dipole at x = 156.5 cm

from the base (feet).

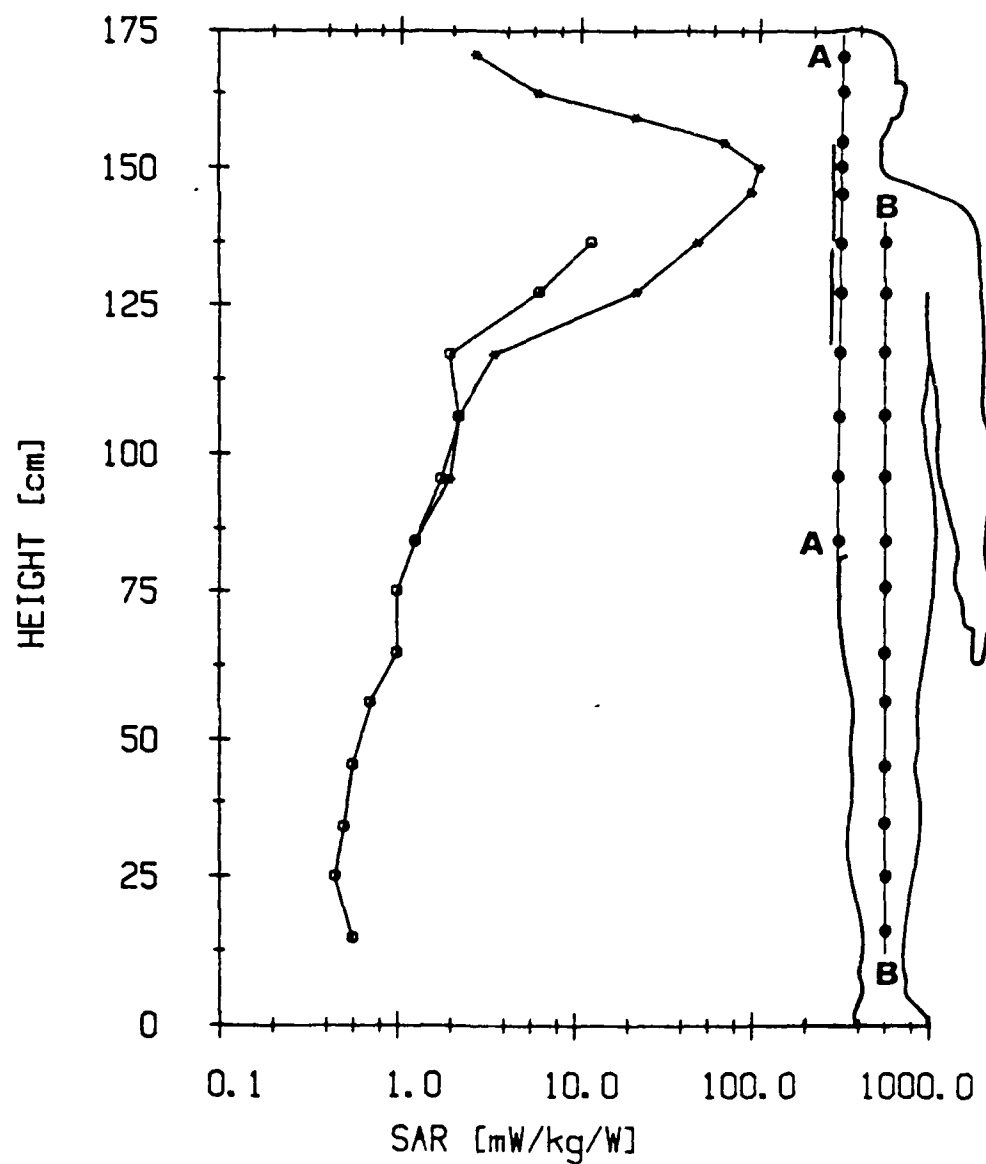


Figure 28 - Near-field experiments, resonant dipole. The mean values of the specific absorption rate (SAR) in a number of locations along the selected axis, frequency 350 MHz, polarization  $E \parallel L$ , power to the antenna 1W,

b) dipole at  $x \approx 137$  cm

from the base (feet).

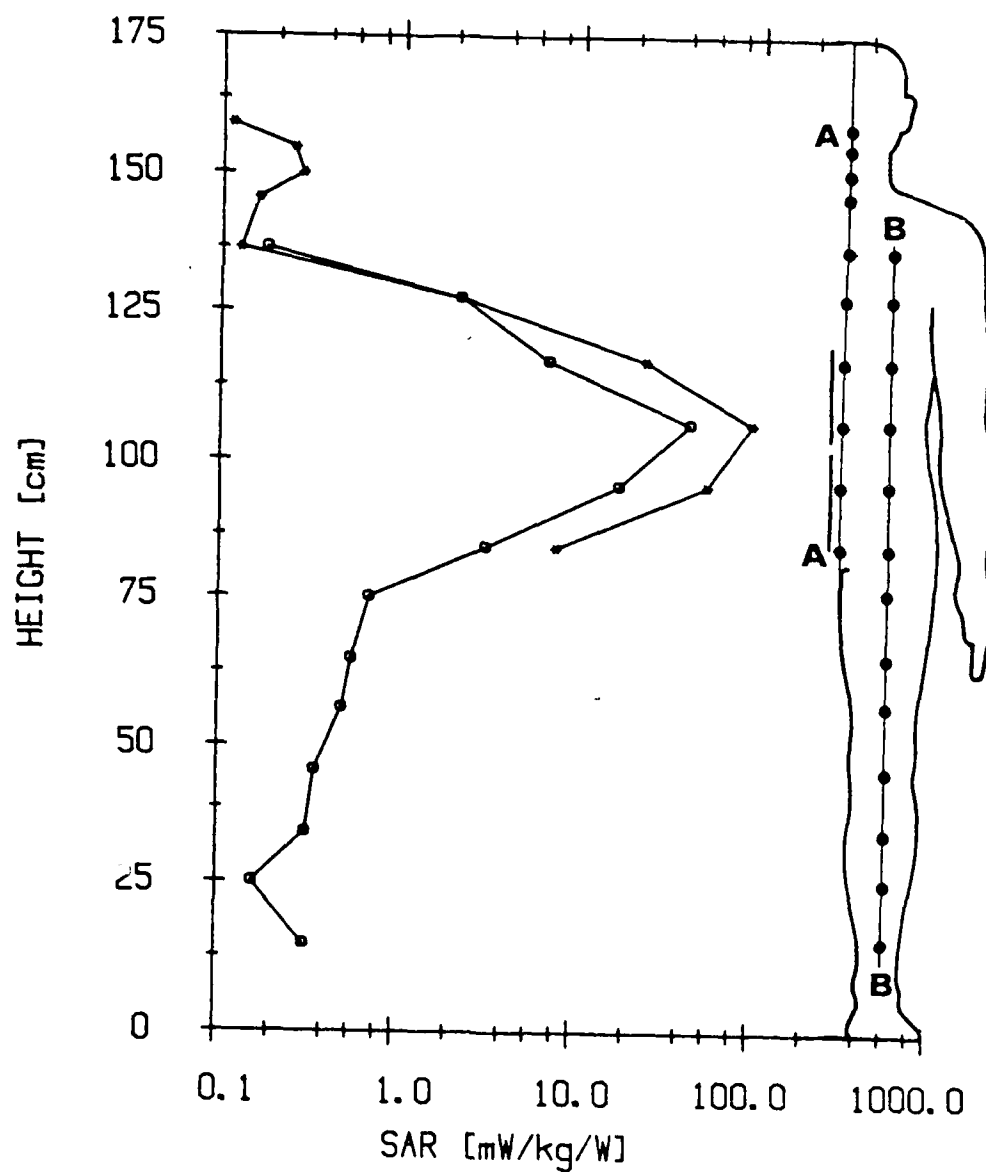


Figure 28 - Near-field experiments, resonant dipole. The mean values of the specific absorption rate (SAR) in a number of locations along the selected axis, frequency 350 MHz, polarization E || L, power to the antenna 1W,

c) dipole at  $x = 103$  cm from the base (feet).

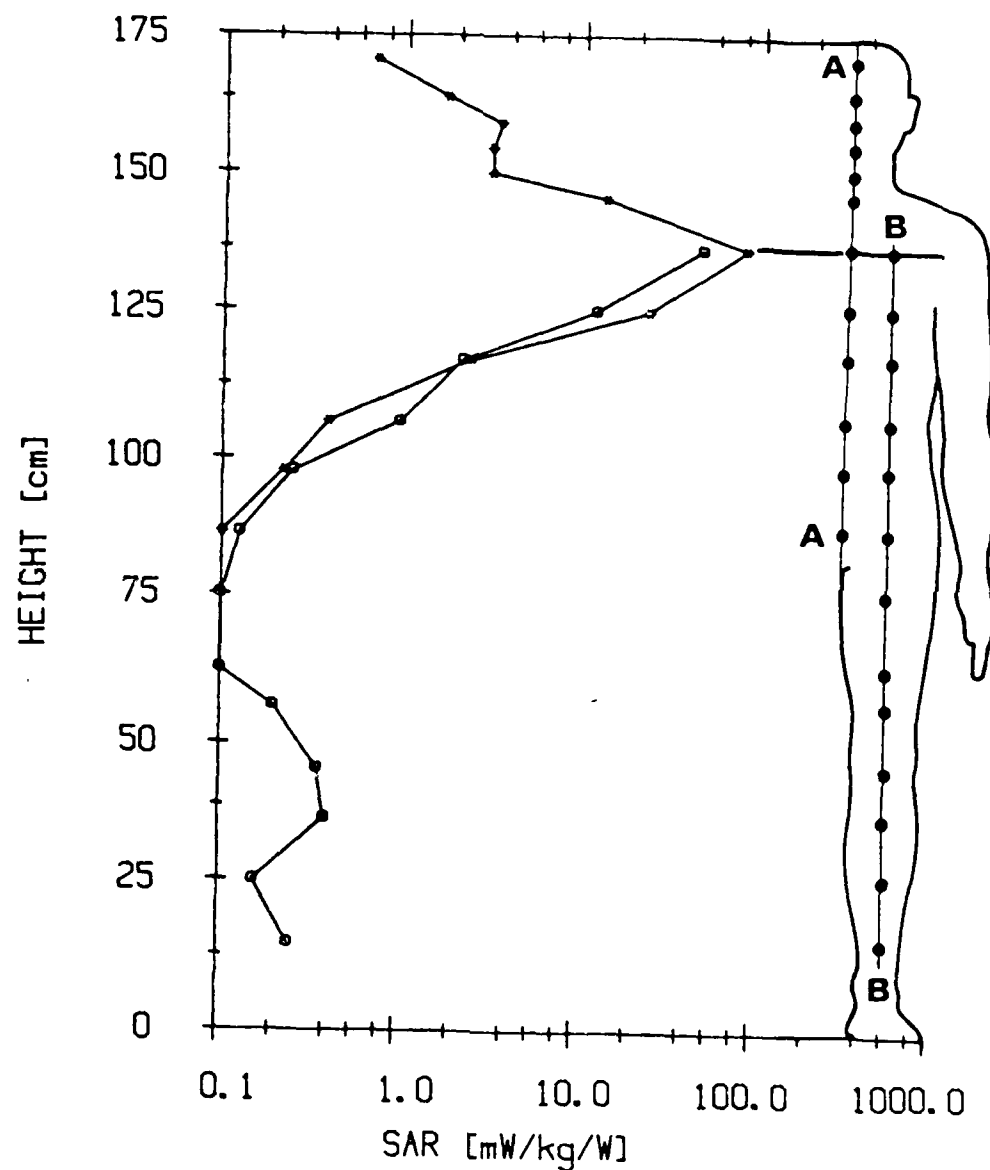


Figure 29 - Near-field experiments, resonant dipole. The mean values of the specific absorption rate (SAR) in a number of locations along the selected axis, frequency 350 MHz, polarization H || L, power to the antenna 1W, dipole at  $x = 137$  cm from the base (feet).

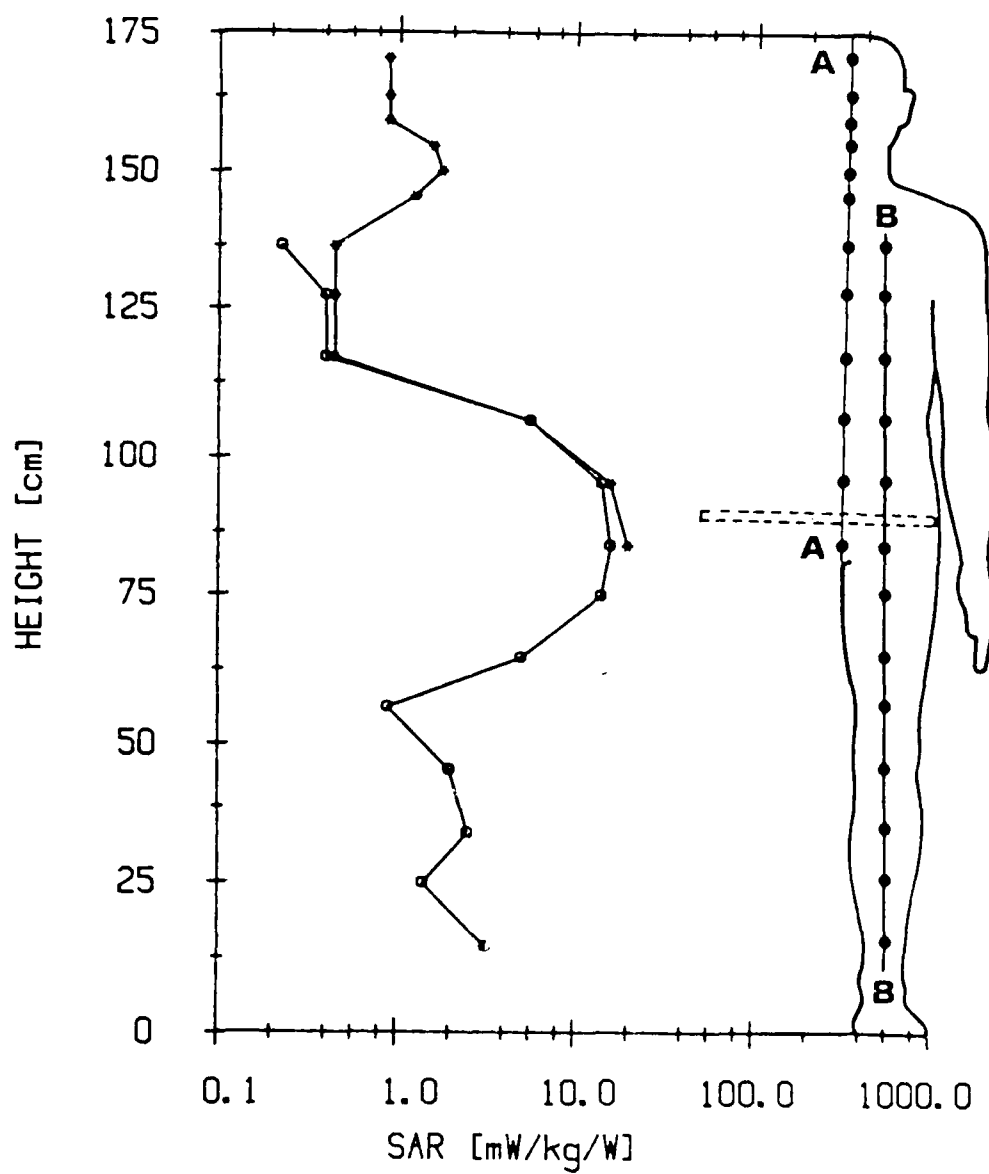


Figure 30 -- Near-field experiments, resonant dipole. The mean values of the specific absorption rate (SAR) in a number of locations along the selected axis, frequency 350 MHz, polarization H || L, power to the antenna 1W, slot at x = 85 cm from the base (feet).



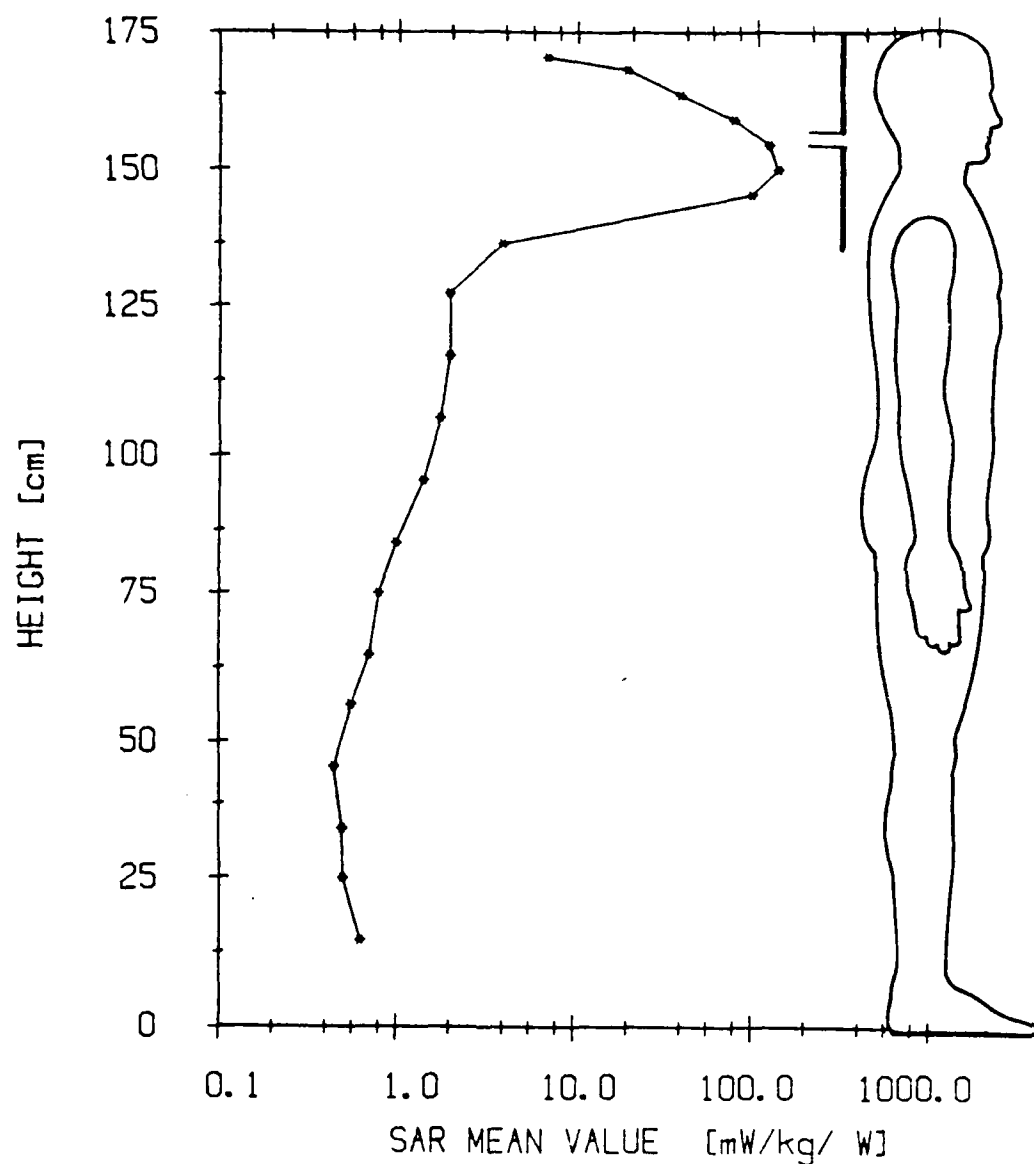


Figure 31 - Near-field experiments, resonant dipole. The mean values of the specific absorption rate (SAR) for horizontal tissue layers along the vertical body axis, frequency 350 MHz, polarization E || L, power to the antenna 1W  
a) dipole at x = 156.5 cm

from the base (feet).

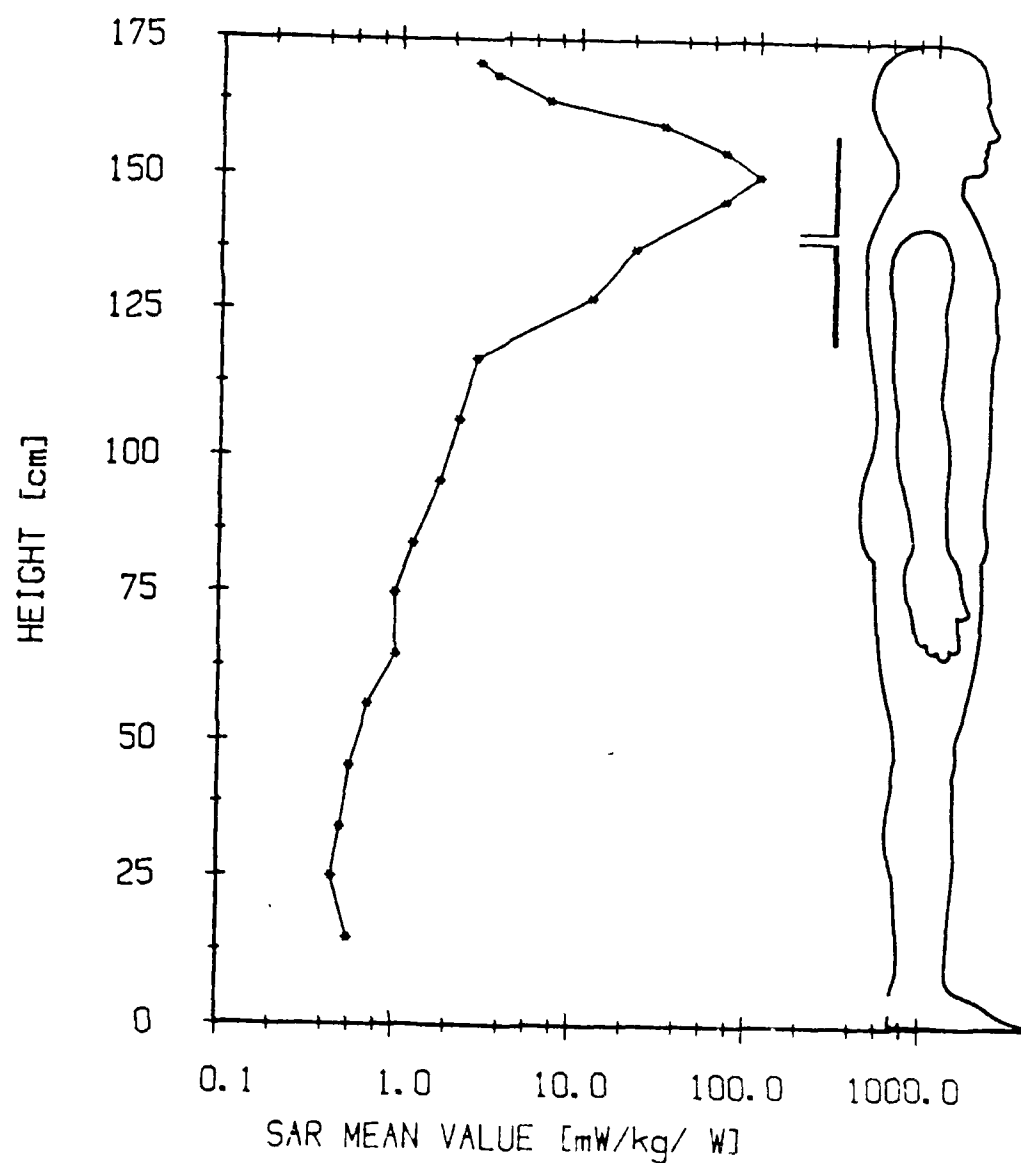


Figure 31 - Near-field experiments, resonant dipole. The mean values of the specific absorption rate (SAR) for horizontal tissue layers along the vertical body axis, frequency 350 MHz, polarization E // L, power to the antenna 1W

b) dipole at  $x = 137$  cm

from the base (feet).

AD-A143 507

STUDIES OF THE ELECTRIC FIELD DISTRIBUTION IN BIOLOGICAL  
BODIES - EXPERIMENTAL (U) OTTAWA UNIV (ONTARIO) DEPT OF  
ELECTRICAL ENGINEERING S S STUCHLY ET AL. MAY 84  
N00044-82-G-0011

2/2

UNCLASSIFIED

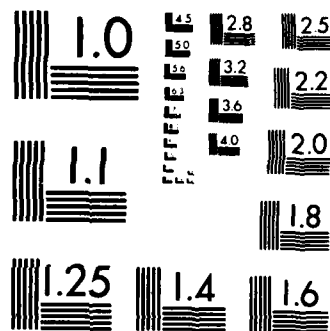
F/G 6/18

NL

END

FILED

DATE



MICROCOPY RESOLUTION TEST CHART  
NATIONAL BUREAU OF STANDARDS-1963-A

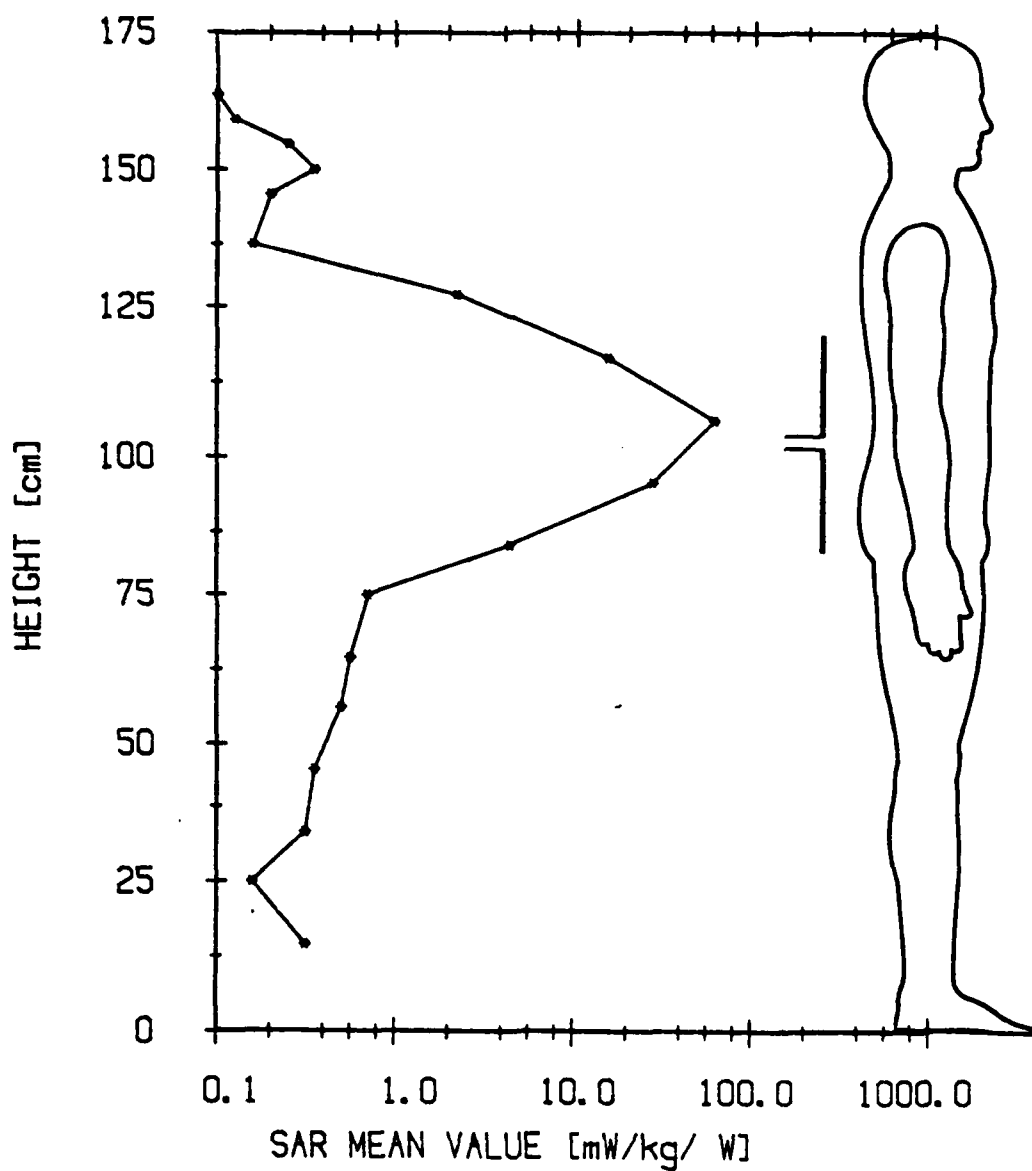


Figure 31 - Near-field experiments, resonant dipole. The mean values of the specific absorption rate (SAR) for horizontal tissue layers along the vertical body axis, frequency 350 MHz, polarization E || L, power to the antenna 1W

c) dipole at x = 103 cm  
from the base (feet).

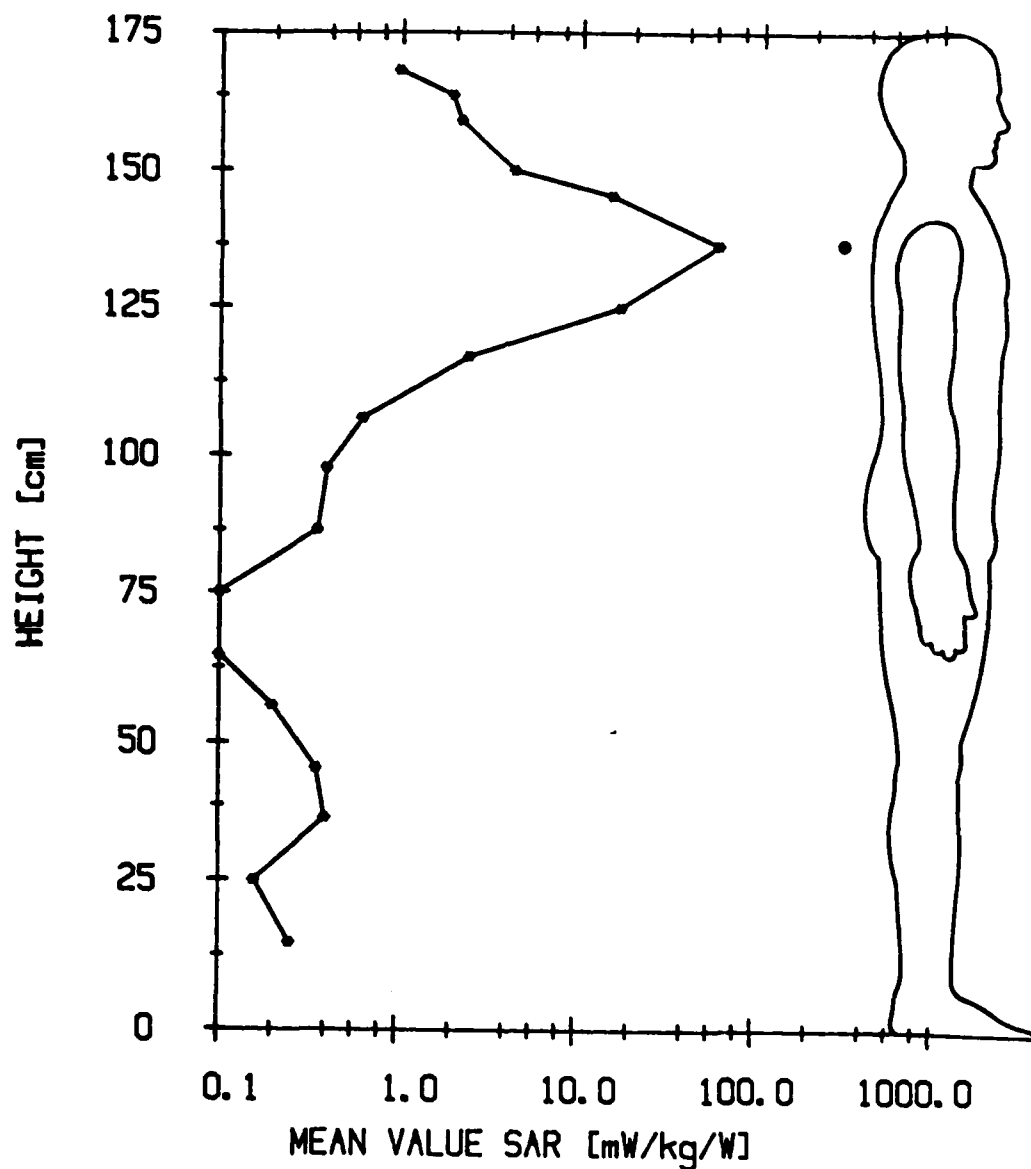
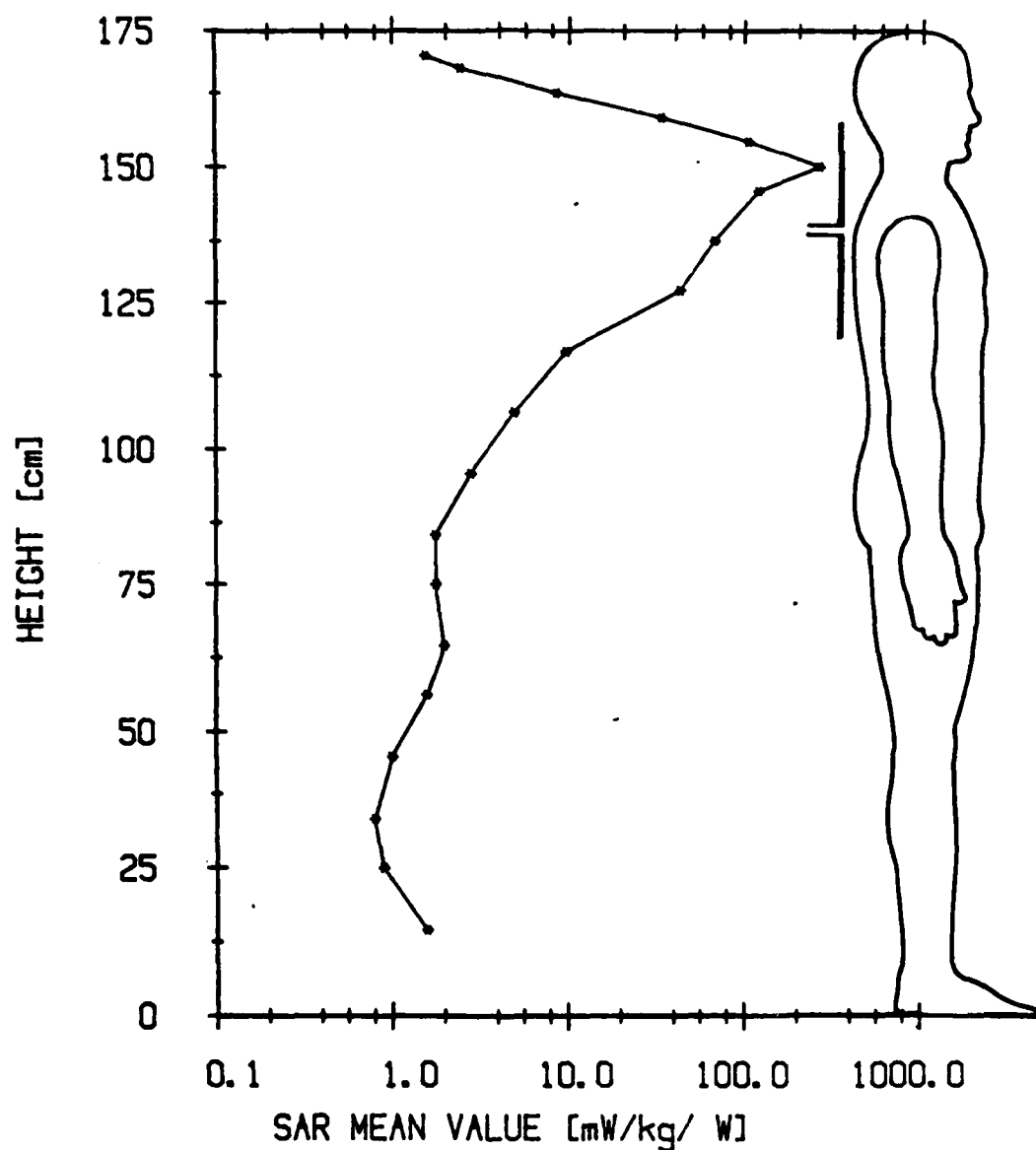


Figure 32 - Near-field experiments, resonant dipole. The mean values of the specific absorption rate (SAR) for horizontal tissue layers along the vertical body axis, frequency 350 MHz, polarization H || L, power to the antenna 1W, dipole at x = 137 cm from the base (feet).



**Figure 33** - Near-field experiments, resonant dipole above the ground plane. The mean values of the specific absorption rate (SAR) for horizontal tissue layers along the vertical body axis, frequency 350 MHz, polarization  $E \parallel L$ , power to the antenna 1W, dipole at  $x = 137$  cm from the base (feet).

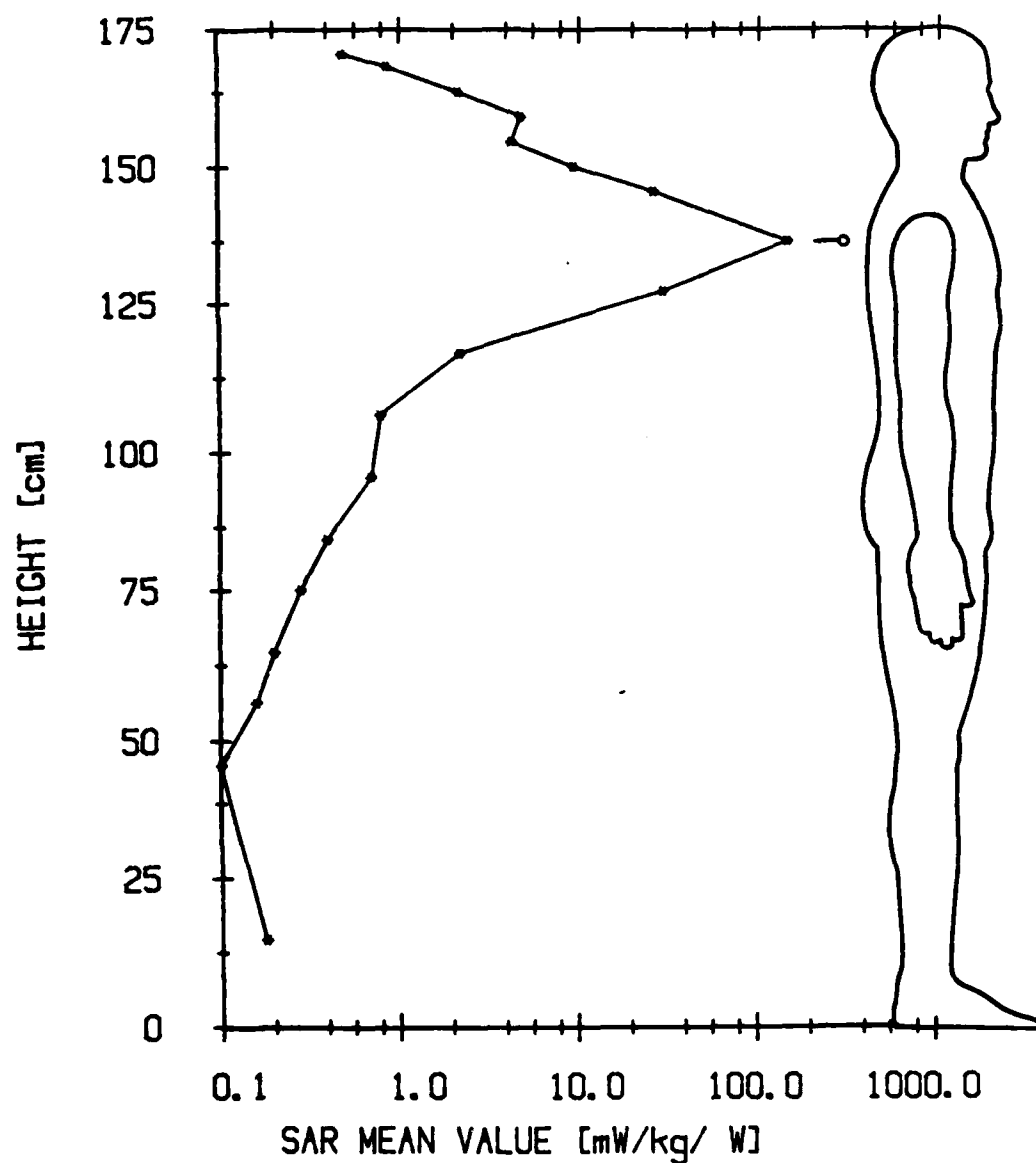


Figure 34 - Near-field experiments, resonant dipole above the ground plane. The mean values of the specific absorption rate (SAR) for horizontal tissue layers along the vertical body axis, frequency 350 MHz, polarization H || L, power to the antenna 1W, dipole at x = 137 cm from the base (feet).



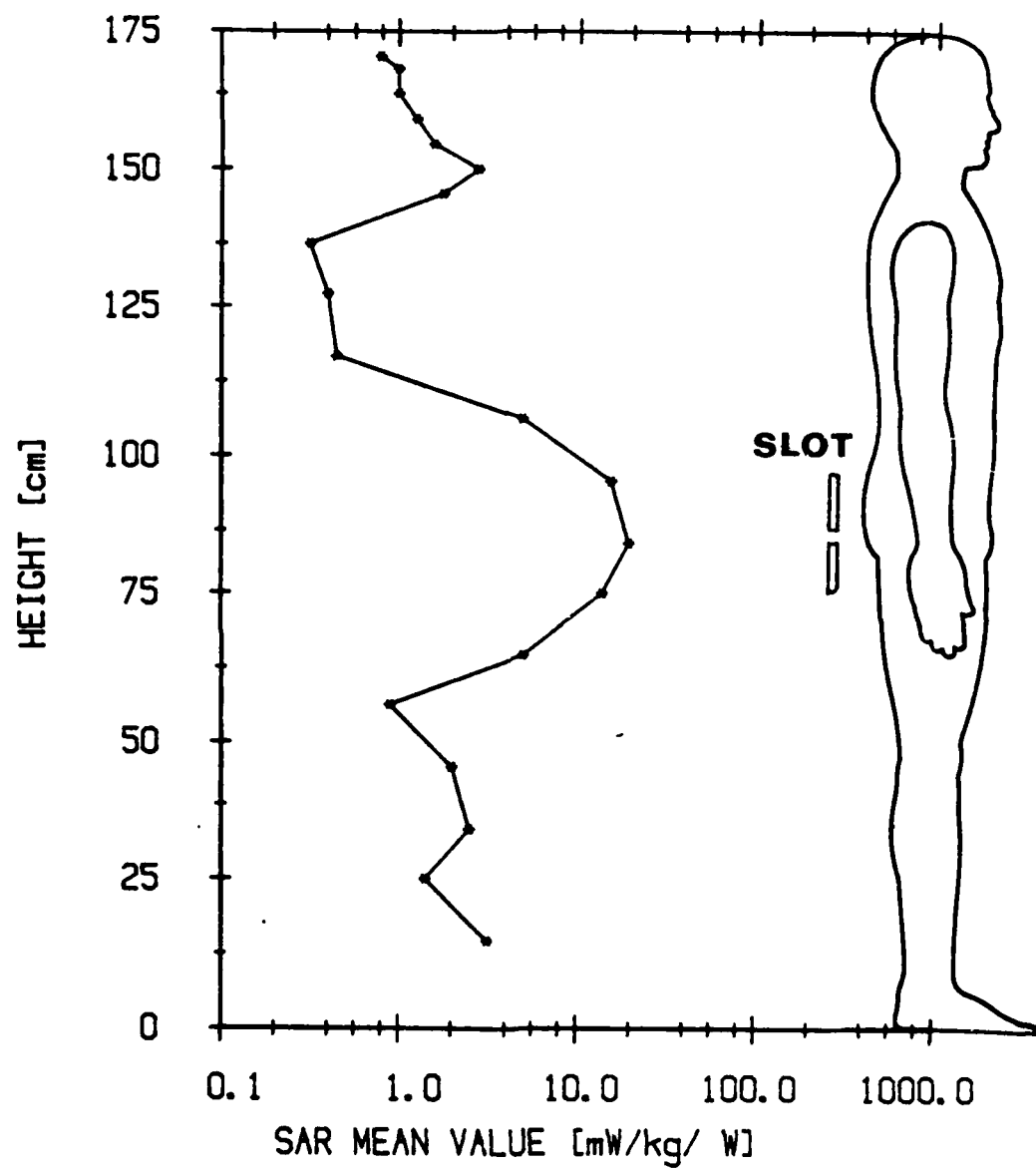


Figure 35 - Near-field experiments, resonant slot. The mean value of the specific absorption rate (SAR) for horizontal tissue layers along the vertical body axis, frequency 350 MHz, polarization E || L power to the antenna 1W, slot at x = 85 cm from the base (feet).

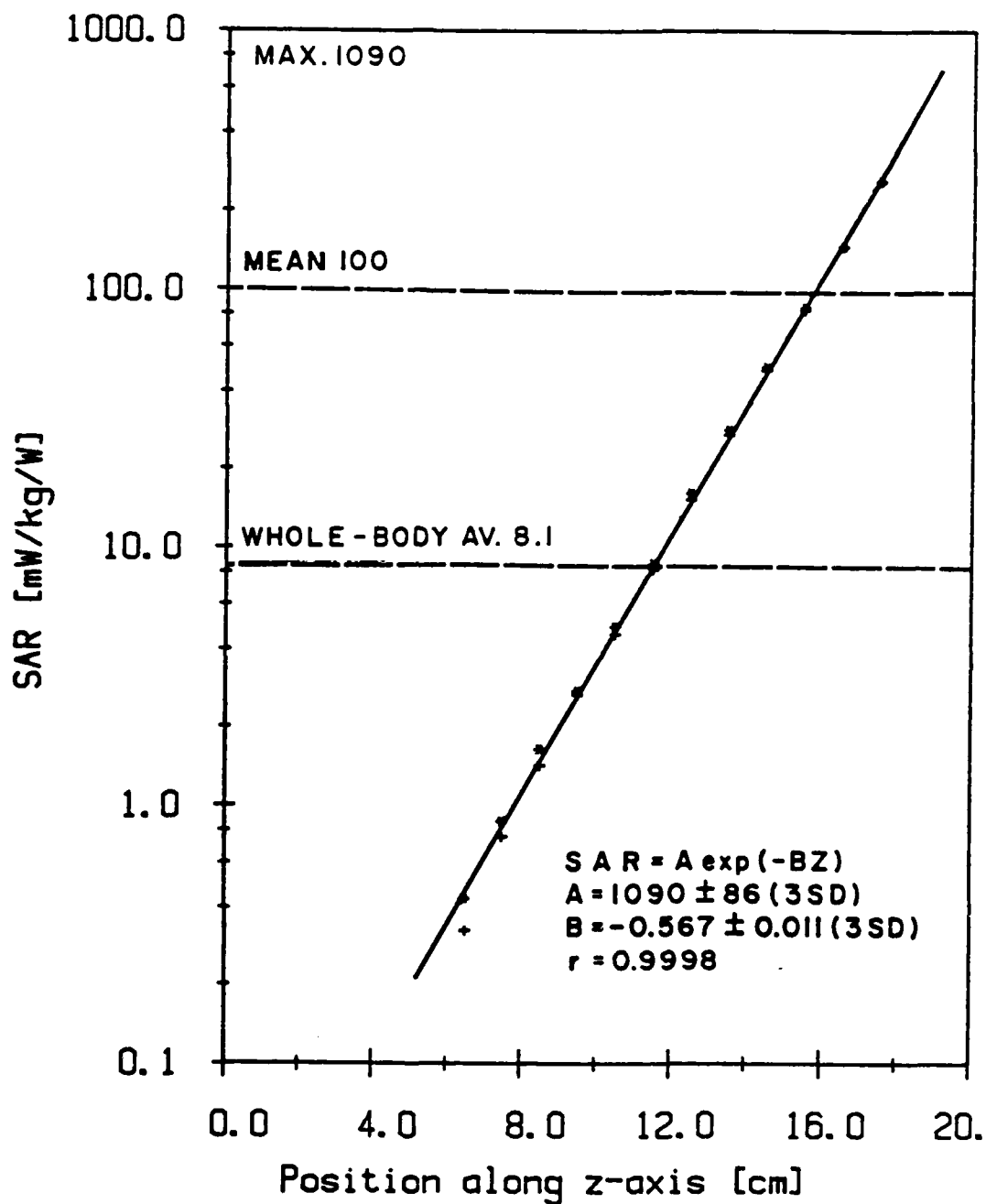


Figure 36 - Near-field experiment, resonant dipole. The specific absorption rate (SAR) in the torso at the dipole axis vs. distance from the body surface at which the wave is incident frequency 350 MHz, polarization E || L, power to the antenna

a) dipole at x = 103 cm  
from the base (feet).

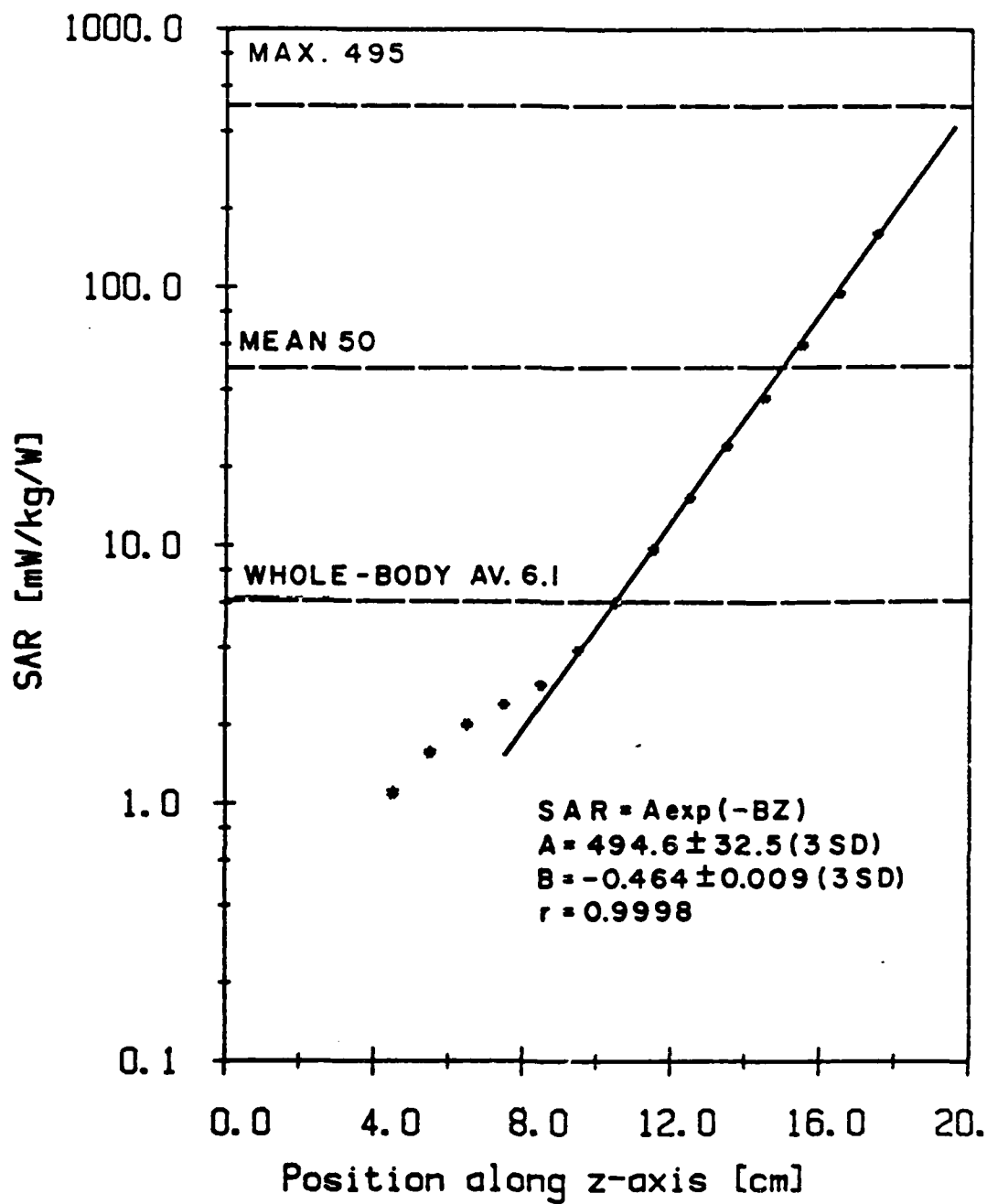


Figure 36 - Near-field experiment, resonant dipole. The specific absorption rate (SAR) in the torso at the dipole axis vs. distance from the body surface at which the wave is incident frequency 350 MHz, polarization E || L, power to the antenna

b) dipole at x = 137 cm  
from the base (feet).

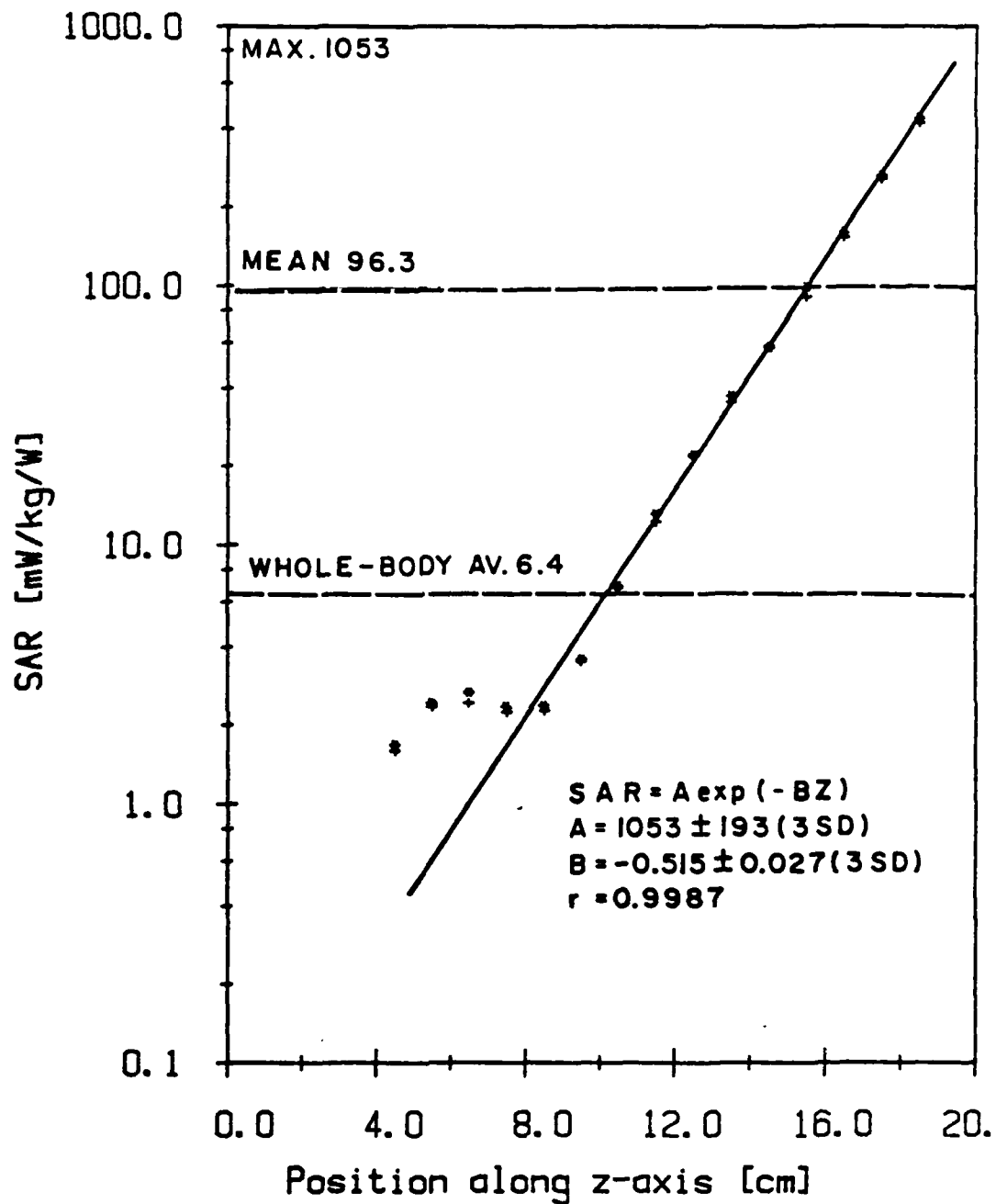


Figure 37 - Near-field experiment, resonant dipole. The specific absorption rate (SAR) in the torso at the dipole axis vs. distance from the body surface at which the wave is incident, frequency 350 MHz, polarization H || L, power to the antenna 1W, dipole at x = 137 cm from the base (feet).

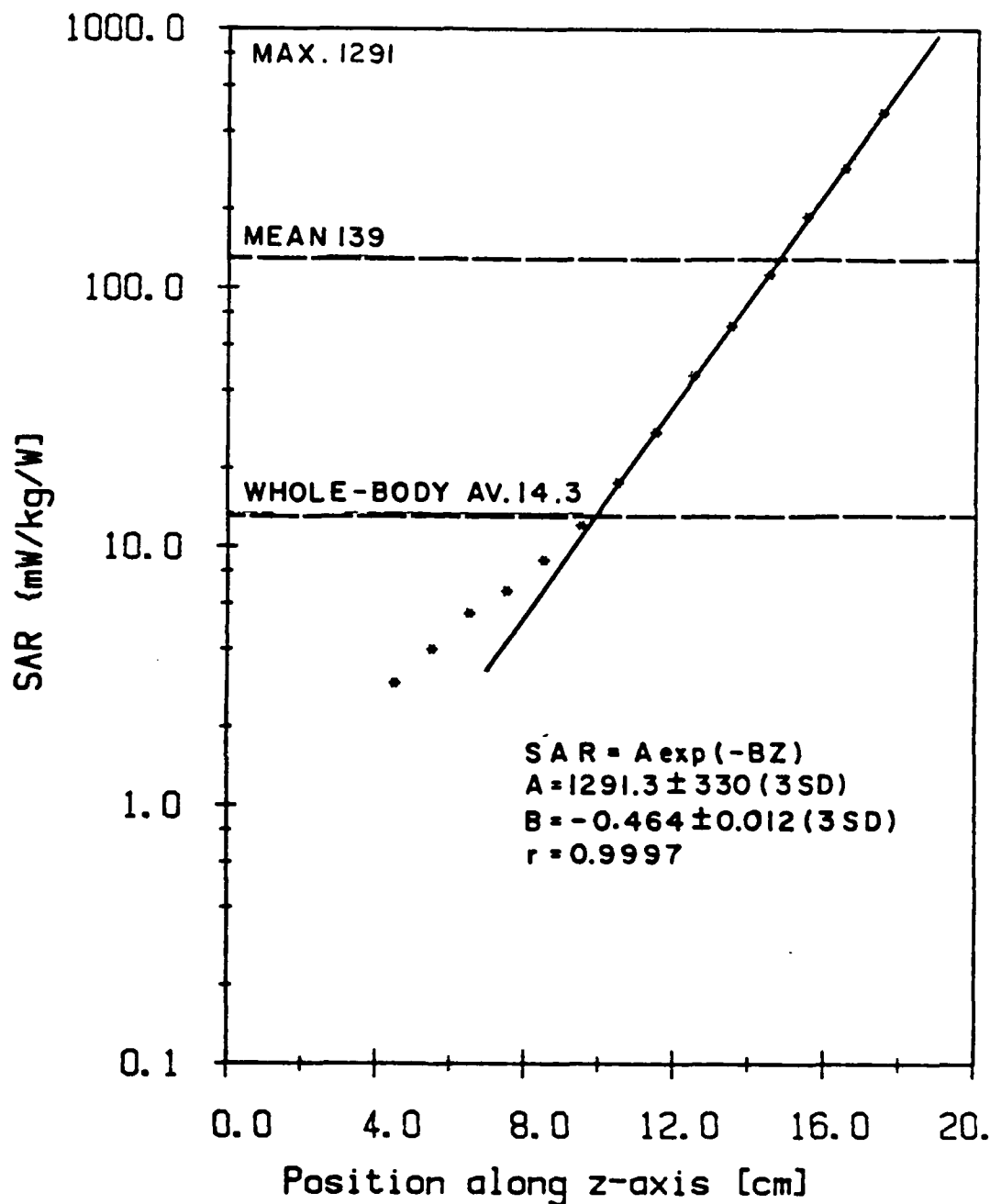


Figure 38 - Near-field experiment, resonant dipole above the ground plane. The specific absorption rate (SAR) in the torso at the dipole axis vs. distance from the body surface at which the wave is incident, frequency 350 MHz, polarization  $E \parallel L$ , power to the antenna 1W, dipole at  $x = 137$  cm from the base (feet).

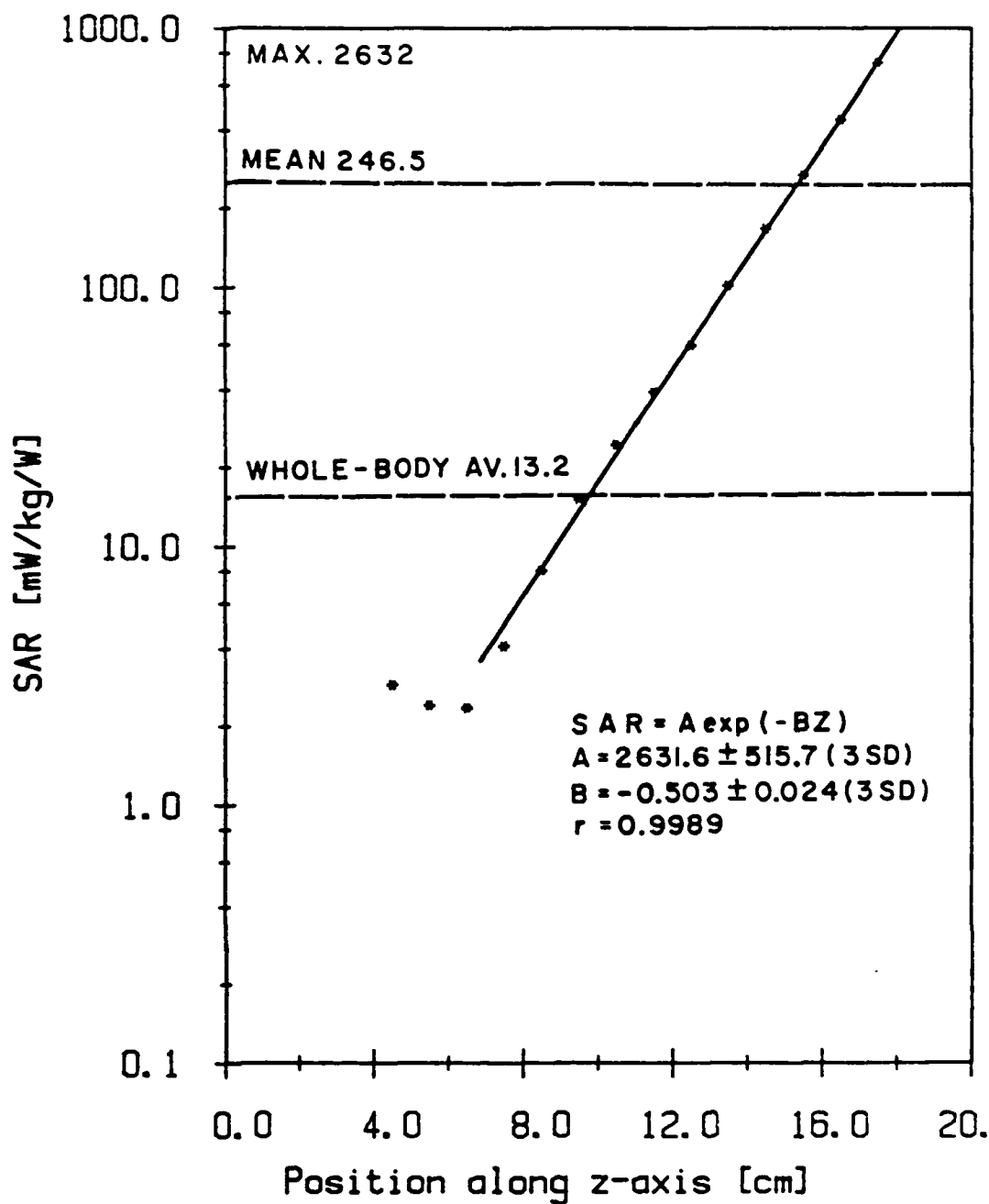


Figure 39 - Near-field experiment, resonant dipole above the ground plane. The specific absorption rate (SAR) in the torso at the dipole axis vs. distance from the body surface at which the wave is incident, frequency 350 MHz, polarization H || L, power to the antenna 1W, dipole at x = 137 cm from the base (feet).

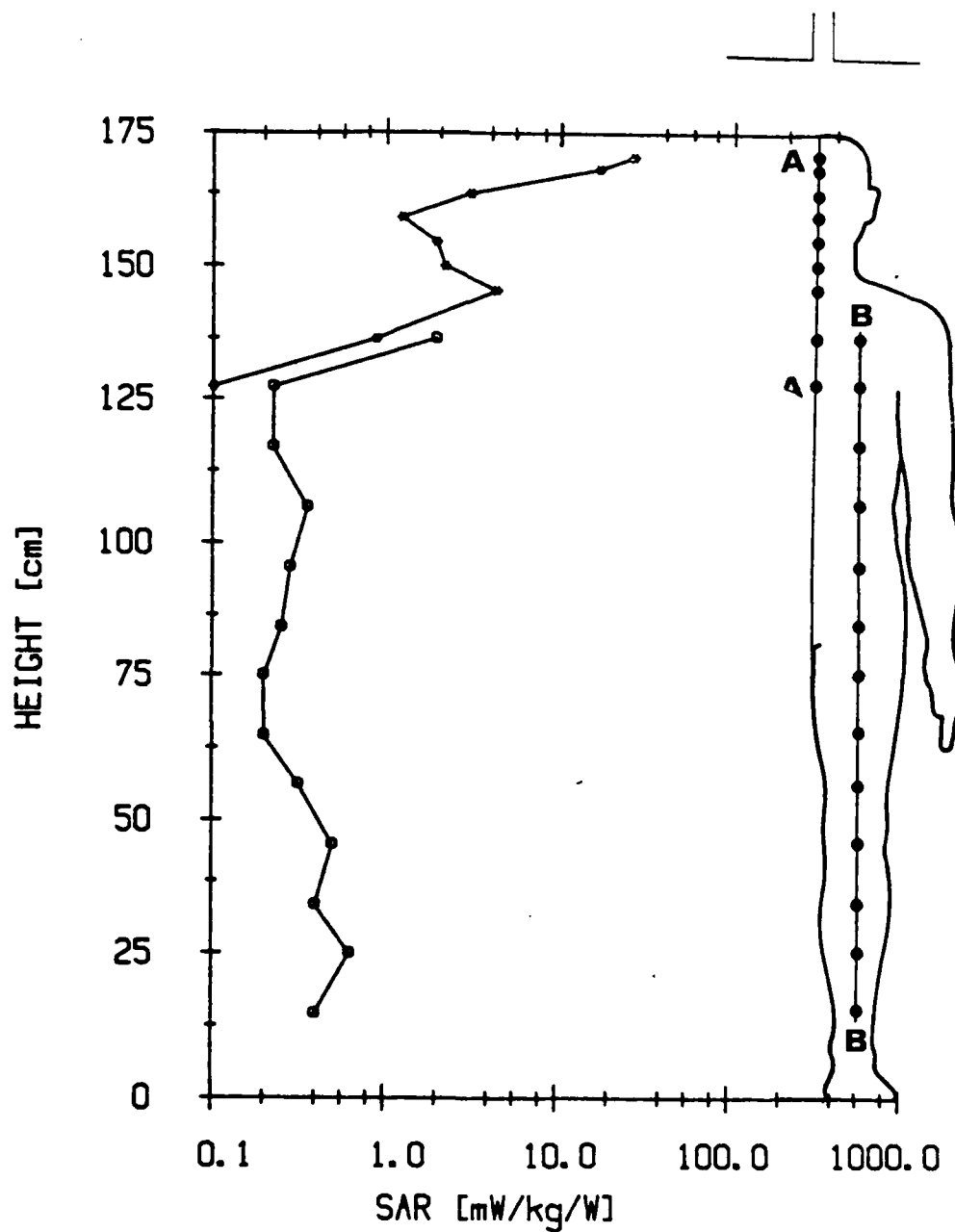


Figure 40 - Near-field experiments, resonant dipole. The local values of the specific absorption rate (SAR) along the selected body axis, frequency 350 MHz, polarization  $k \parallel L$ , power to the antenna 1W, the dipole 14 cm above the head.

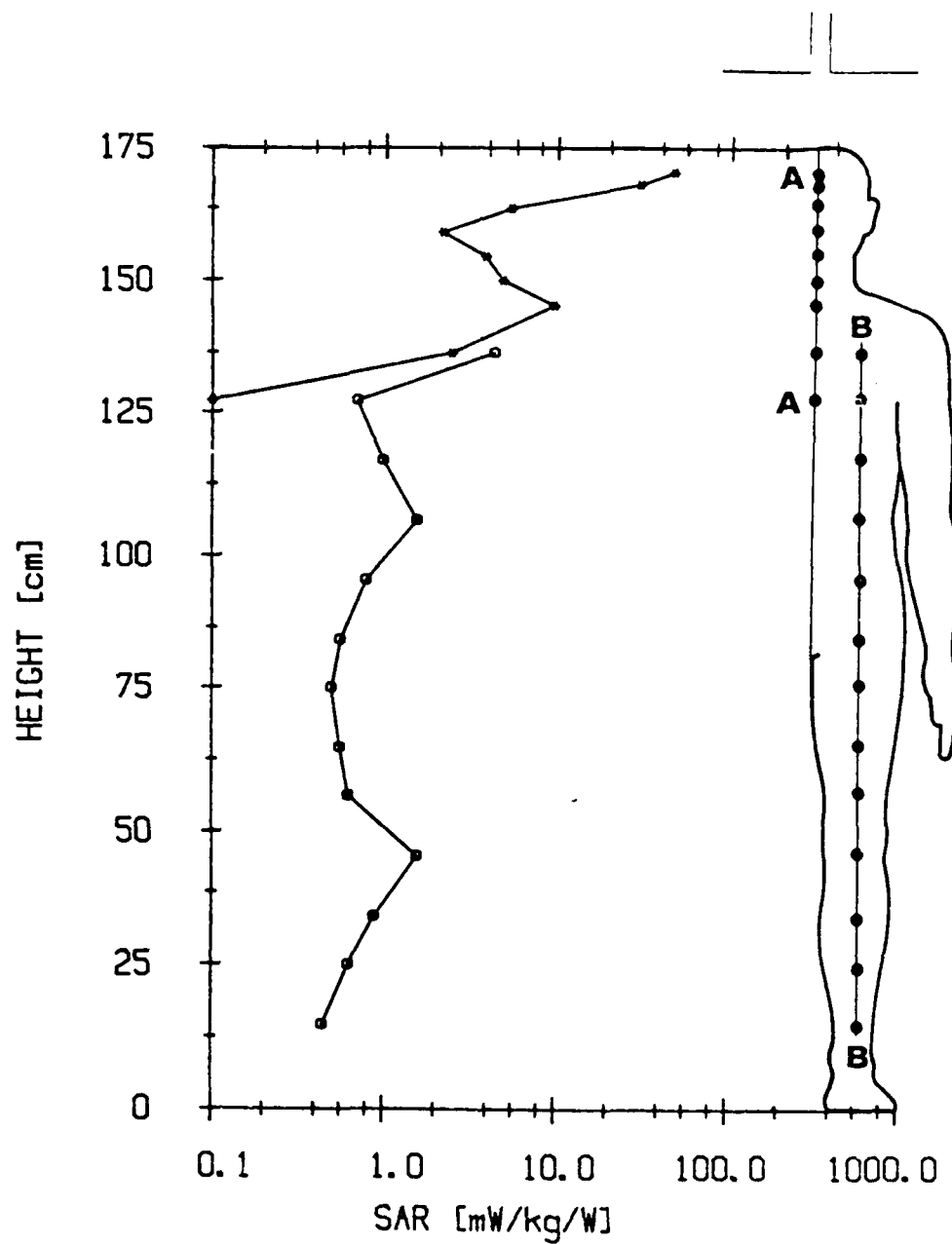


Figure 41 - Near-field experiments, resonant dipole above the ground plane. The local values of the specific absorption rate (SAR) along the selected body axis, frequency 350 MHz, polarization  $k \parallel L$ , power to the antenna 1W, the dipole 14 cm above the head.



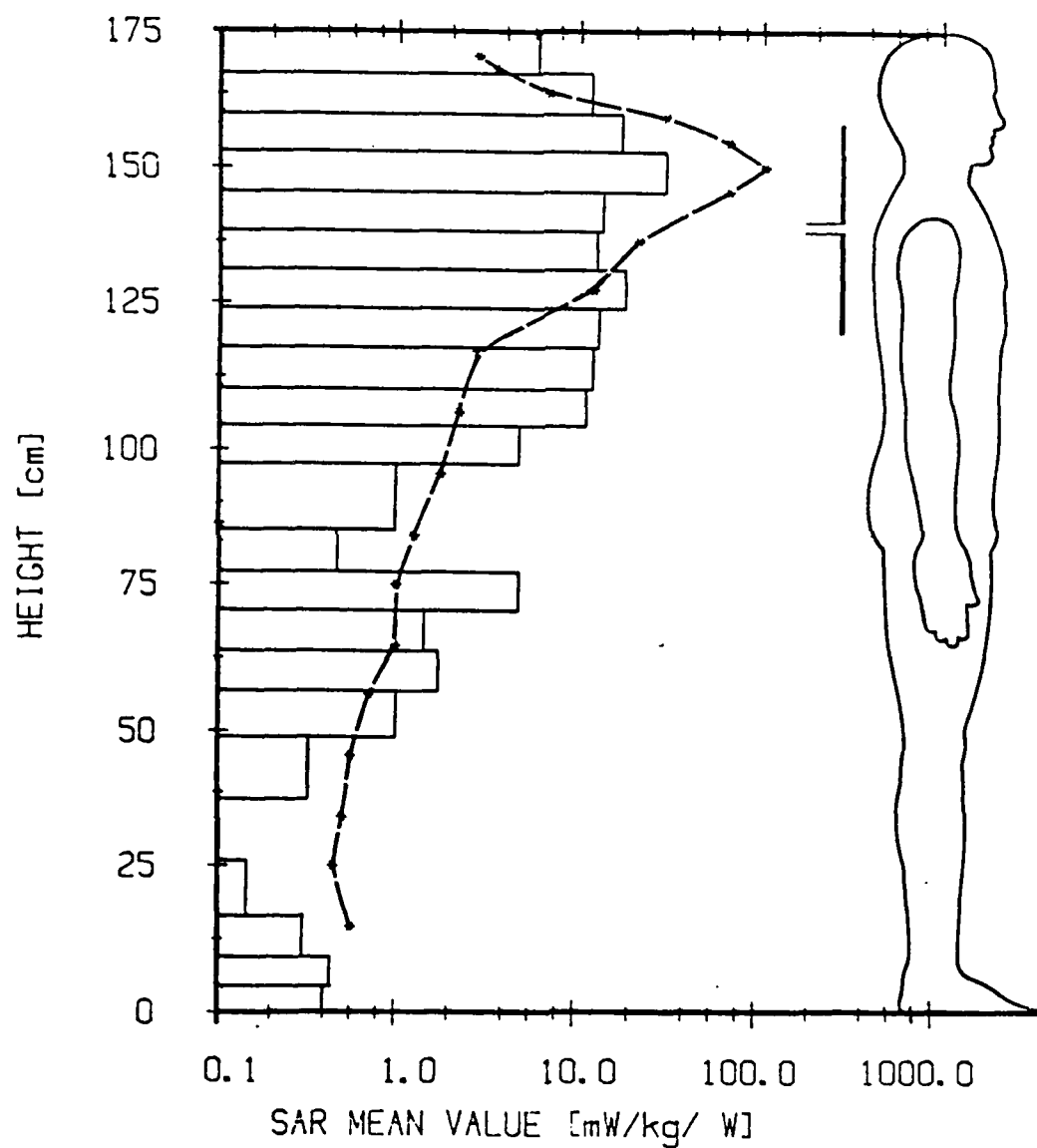


Figure 42 - Near-field experiment. Comparison of the specific absorption rate (SAR) averaged over the body horizontal cross-sections: the experimental data vs. the data calculated for the block model, resonant dipole, frequency 350 MHz, polarization  $E \parallel L$ , power to the antenna 1W, dipole at  $x = 137$  cm from the base (feet).

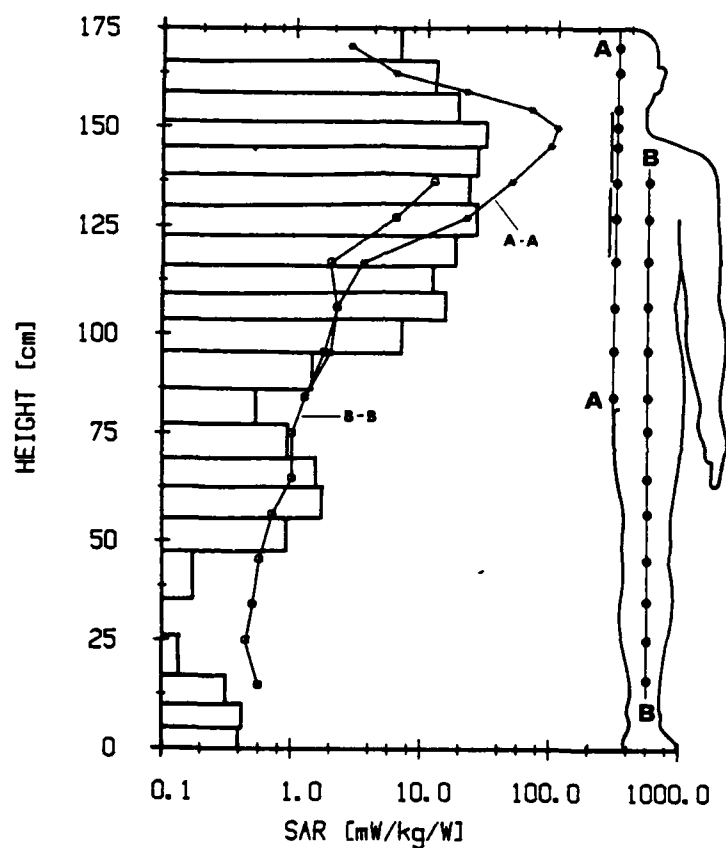


Figure 43 - Near-field experiment. Comparison of the specific absorption (SAR) averaged in the direction of the wave propagation for various positions along two vertical body axis. Experimental data (this work) vs. the data calculated for the block-model of man, frequency 350 MHz, polarization E || L, power to the antenna 1W, dipole at x = 137 cm from the base (feet).

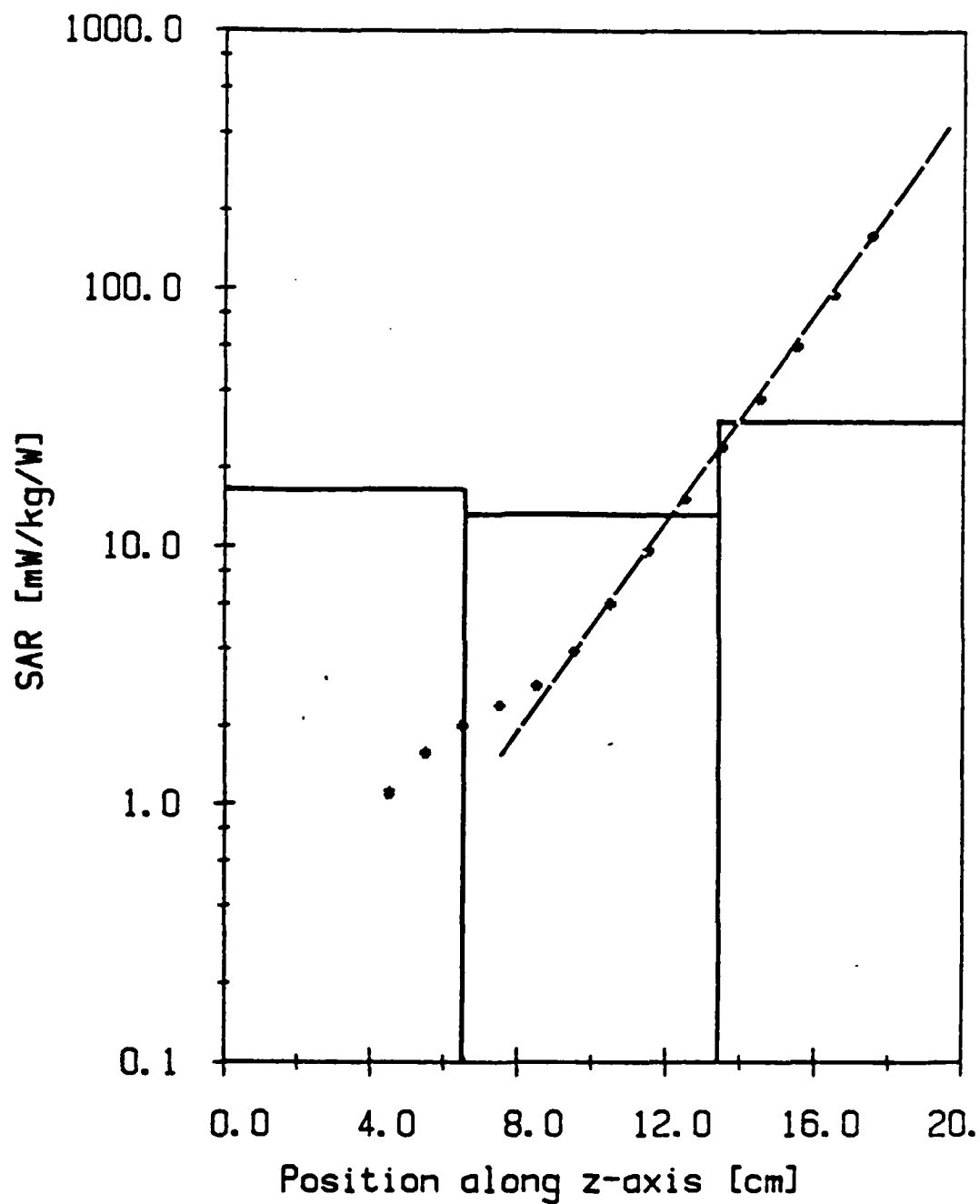


Figure 44 - Near-field experiment. Comparison of the local specific absorption rate (SAR) along the direction of the wave propagation in the torso, experimental data (this work) (stars) and values calculated for the block model (blocks), frequency 350 MHz, polarization  $E \parallel L$ , power to the antenna 1W.